H^- ION SOURCE FOR CERN'S LINAC4 ACCELERATOR: SIMULATION, EXPERIMENTAL VALIDATION AND OPTIMIZATION OF THE HYDROGEN PLASMA

THÈSE N^O 7907 (2017)

PRÉSENTÉE LE 24 JUILLET 2017
À LA FACULTÉ DES SCIENCES DE BASE
CRPP - INSTALLATIONS INTERNATIONALES
PROGRAMME DOCTORAL EN PHYSIQUE

ÉCOLE POLYTECHNIQUE FÉDÉRALE DE LAUSANNE

POUR L'OBTENTION DU GRADE DE DOCTEUR ÈS SCIENCES

PAR

Stefano MATTEI

acceptée sur proposition du jury:

Prof. O. Schneider, président du jury
Prof. M. Q. Tran, Dr J. Lettry, directeurs de thèse
Prof. U. Fantz, rapporteuse
Prof. A. Hatayama, rapporteur
Prof. P. Ricci, rapporteur

ÉCOLE POLYTECHNIQUE
FÉDÉRALE DE LAUSANNE
Suisse
2017

Acknowledgements

My time spent as PhD student has been a wonderful journey, and I am grateful to many people who have supported and motivated me throughout. My deepest gratitude goes to my supervisors, Dr. Jacques Lettry, who has provided all the means to accomplish this result and created a friendly and international collaboration that has truly been an inspiration for my future career. Prof. Minh Quang Tran for his guidance and kindness, always found the time to support me and answer my questions. No matter how busy his schedule was I always knew that I could count on him. I had the honor to work in close collaboration with Prof. Akiyoshi Hatayama, who offered me the warmest hospitality in his lab and with his enthusiasm showed me the wonders of plasma simulations, どうもありがとうございました。Many thanks to Prof. Ursel Fantz, the appreciation she showed for my work has given me the motivation to improve and to go a step forward. Prof. Paolo Ricci for his help in the details of the model and for the fruitful discussions on the implicit algorithm. I would also like to thank Prof. Olivier Schneider for accepting to chair my exam committee.

Working in such a large and international organization, truly has made the world seem smaller, removing all frontiers. Over these years I had the opportunity to collaborate with wonderful people and make friends all over the world. This not only made me a better scientist, but more importantly a better person. A special thanks goes to all the students at KEIO University, in particular K. Nishida, S. Nishioka, M. Ohta, S. Mochizuki and M. Onai. Your hard work has been key to the success of this project. And you made me love your country so much that you motivated me to learn Japanese! I want to express my gratitude to the team at the University of Augsburg, especially S. Briefi and D. Rauner who have greatly contributed to the experimental campaign and the benchmarking of the code.

Many people at CERN contributed to the realization of this thesis. A big thanks to E. Macintosh who helped me setup the code at CERN and T. Pieloni for her assistance with the clusters. Many thanks also to the IT department, particularly N. Høimyr, C. Lindqvist, P. Ganz and M. Husejko. My daily work at CERN would not have been the same without the support and kindness of many colleagues: P. Andersson, S. Bertolo, D. Fink, F. di Lorenzo, E. Mahner, H. Martinet, C. Mastrostefano, O. Midttun, M. O'Neil, H. Pereira, D. Rivoiron, R. Scrivens, G. Voulgarakis, A. Lombardi and the HSL team. Many thanks to D. Steyaert, E. Chaudet and Y. Coutron who provided the drawings of the Linac4 ion source.

From young age I had the support of the best family and friends one can hope for. Thank you for always believing in me, I owe you my deepest gratitude. Un grazie speciale ai miei più cari amici Fede, Giulio, Tita. Grazie ragazzi, siete i migliori e so che sempre posso contare su di voi.

Acknowledgements

Grazie al mio caro amico Enrico che è stato il miglior professore che uno possa immaginare di avere. Grazie a Silvano che è sempre stato come un fratello; zio Guido, Tarcisio e Gina per avermi sempre sostenuto. Grazie nonna Mariuccia e nonno Riccardo per il vostro affetto, siete sempre nel mio cuore. Gracias a Manuel que me apoyó en este camino. Mis años de doctorado no hubiesen sido igual de especial sin el apoyo y el amor de mi querida Reina, gracias por todo. Devo ai miei genitori la mia più profonda gratitudine, papà Aldo e mamma Iris, per aver sempre creduto in me e aver fatto tutto il possibile per il mio bene.

Lausanne, 20 May 2017 Stefano Mattei

Abstract

Linac4 is the new negative hydrogen ion (H^-) linear accelerator of the European Organization for Nuclear Research (CERN). Its ion source operates on the principle of Radio-Frequency Inductively Coupled Plasma (RF-ICP) and it is required to provide 50 mA of H^- beam in pulses of 600 μs with a repetition rate up to 2 Hz and within an RMS emittance of 0.25 π mm mrad in order to fullfil the requirements of the accelerator.

This thesis is dedicated to the characterization of the hydrogen plasma in the Linac4 H^- ion source. We have developed a Particle-In-Cell Monte Carlo Collision (PIC-MCC) code to simulate the RF-ICP heating mechanism and performed measurements to benchmark the fraction of the simulation outputs that can be experimentally accessed. The code solves self-consistently the interaction between the electromagnetic field generated by the RF coil and the resulting plasma response, including a kinetic description of charged and neutral species. A fully-implicit implementation allowed to simulate the high density regime of the Linac4 H^- ion source, ensuring the energy conservation while maintaining the computational resources tractable.

We studied the capacitive to inductive transition characteristic of the initial phase of the pulsed discharge. The simulation results were confirmed by time-resolved photometry measurements and allowed quantifying the effect of the hydrogen pressure and of the external magnetic cusp field on the transition dynamics. This provided insights into possible modifications to the magnetic cusp field configuration to maximize the power deposited to the plasma.

The optimal ion source configuration maximizes the density of volume produced H^-, the flux of H^0 atoms onto the cesiated molybdenum plasma electrode surface at the origin of H^- emission, and minimizes the electron density and energy in the beam formation region. We simulated the high-density regime (10^{19} m^{-3}) representative of the nominal operation of the Linac4 ion source during beam extraction. We performed a parametric study of the RF current, hydrogen pressure and magnetic configuration (cusp and filter) to assess their impact on the plasma parameters. The simulation results allowed assessment of these parameters and provided guidelines for the optimization of the ion source operational and design parameters.

The simulation results of electron density, electron energy and hydrogen dissociation degree showed excellent agreement with optical emission spectroscopy measurements both as a function of RF coil current and magnetic configuration. The outputs of these simulations provide crucial inputs to beam formation and extraction physics models. Dedicated PIC software packages are being developed that will eventually shed insight into essential beam parameters such as the intensity and emittance of the H^- beam and the intensity of the

co-extracted electrons.

Key words: Ion source, particle accelerator, Particle-In-Cell, Monte Carlo Collision, RF-ICP

Riassunto

Linac4 è il nuovo acceleratore lineare di ioni negativi di idrogeno (H^-) dell'organizzazione europea per la ricerca nucleare (CERN). La sua sorgente di ioni opera secondo il principio dei plasmi accoppiati induttivamente alle radio frequenze e deve fornire un fascio di 50 mA di H^- in impulsi di 600 μs con una ripetizione fino a 2 Hz ed un'emittanza RMS inferiore a 0.25 π mm mrad.

Questa tesi ha come obiettivo la caratterizzazione del plasma di idrogeno della sorgente di ioni del Linac4. Abbiamo sviluppato un codice Particle-In-Cell Monte Carlo Collision (PIC-MCC) con lo scopo di simulare il meccanismo di sostentamento del plasma ad accoppiamento induttivo. Allo stesso tempo una campagna sperimentale è stata organizzata per permettere un confronto diretto tra simulazioni e misure. Il codice simula l'interazione tra il campo elettromagnetico generato dall'antenna e la conseguente dinamica del plasma. Quest'ultima include una descrizione cinetica sia delle specie elettricamente cariche che di quelle neutre. Grazie ad un algoritmo d'integrazione implicito, il modello permette di simulare alte densità preservando la conservazione dell'energia e mantenendo un costo computazionale limitato.

In primo luogo abbiamo studiato la transizione dall'accoppiamento capacitivo ad induttivo caratteristico della fase iniziale dell'impulso. I risultati delle simulazioni, confermati da misure fotometriche in funzione del tempo, hanno permesso di quantificare l'effetto della pressione d'idrogeno e del campo magnetico esterno sulla dinamica della transizione. Questo ha permesso di identificare possibili miglioramenti da apportare alla configurazione magnetica per migliorare l'efficienza di trasmissione di potenza dall'antenna al plasma.

Successivamente, abbiamo simulato il regime di alta densità (10^{19} m^{-3}) caratteristico dell'operazione nominale della sorgente di ioni durante l'estrazione del fascio. Uno studio parametrico della corrente dell'antenna, della pressione d'idrogeno e della configurazione magnetica ha permesso di determinare l'effetto di tali variazioni sulla dinamica del plasma. L'ottimizzazione della sorgente di ioni consiste nel massimizzare la densità di ioni di idrogeno prodotti nel volume del plasma, il flusso d'atomi H^0 incidenti sull'elettrodo a basso lavoro d'estrazione all'origine dell'emissione di H^-, e allo stesso tempo minimizzare la densità di elettroni e la loro energia nella zona di formazione del fascio. I risultati delle simulazioni hanno permesso di determinare l'influenza di parametri operazionali e di disegno su tali densità ed energie, permettendo di identificare possibili miglioramenti alla configurazione attuale per ottimizzarne l'efficienza.

La densità elettronica, l'energia elettronica ed il grado di dissociazione d'idrogeno sono in ottimo accordo con risultati di misure spettroscopiche sia in funzione della corrente dell'antenna

che in base alla configurazione magnetica esterna. I risultati di queste simulazioni forniscono per la prima volta le caratteristiche del plasma nella zona d'estrazione, che sono critiche per la simulazione della formazione e l'estrazione del fascio. Codici specifici per tale scopo sono in corso di sviluppo e permetteranno in futuro di caratterizzare i parametri del fascio all'uscita della sorgente, come l'intensità e l'emittanza del fascio di H^- e degli elettroni co-estratti.

Parole chiave: sorgente di ioni, acceleratore di particelle, Particle-In-Cell, Monte Carlo, plasmi ad accoppiamento induttivo

Contents

List of Figures

List of Tables

List of acronyms

AD . . . . . Antiproton Decelerator

ADet . . . . . Associative Detachment

ALICE . . . . . A Large Ion Collider Experiment

ATLAS . . . . . A Toroidal LHC ApparatuS

AWAKE . . . . . Advanced WAKefield Experiment

CCDTL . . . . . Cell Coupled Drift Tube Linac

CERN . . . . . Conseil Européen pour la Recherche Nucléaire

Chop. . . . . . Chopper and buncher

CID . . . . . Collision Induced Dissociation

CMS . . . . . Compact Muon Solenoid

CNGS . . . . . Cern Neutrinos to Gran Sasso

CPU . . . . . Central Processing Unit

CR . . . . . Collisional Radiative

CTF3 . . . . . Clic Test Facility

DEL . . . . . Delivered (RF power)

Det . . . . . non-associative Detachment

DTL . . . . . Drift Tube Linac

ED . . . . . Electron Detachment

EEDF . . . . . Electron Energy Distribution Function

EL . . . . . Einzel Lens

EM . . . . . Electro Magnetic

EM-PIC-MCC . . Electro Magnetic Particle-In-Cell Monte Carlo Collision

E-H . . . . . Electrostatic-Inductive

FC . . . . . Faraday Cup

FDTD . . . . . Finite Difference Time Domain

FWD . . . . . Forward (RF power)

GMRES . . . . . Generalized Minimal RESidual

HiRadMat . . . . High-Radiation to Materials

HL-LHC . . . . . High Luminosity Large Hadron Collider

HV . . . . . High Voltage

ICCD . . . . . Intensified Charge Coupled Device

ICP . . . . . Inductively Coupled Plasma

ISOLDE . . . . . Isotope mass Separator On-Line DEvice

JFNK . . . . . Jacobian Free Newton Krylov

LEBT . . . . . Low Energy Beam Transport

LEIR . . . . . Low Energy Ion Ring

LHC . . . . . Large Hadron Collider

LHCb . . . . . Large Hadron Collider beauty

Linac . . . . . Linear Accelerator

LIU . . . . . LHC Injector Upgrade

LU . . . . . Lower Upper

n-ToF . . . . . Neutron Time of Flight

MCC . . . . . Monte Carlo Collision

MN . . . . . Mutual Neutralization

MPI . . . . . Message Passing Interface

NIBS . . . . . Negative Ion Beams Sources

OES . . . . . Optical Emission Spectroscopy

PD . . . . . Puller-Dump

PIC . . . . . Particle-In-Cell

PIC-MCC . . . . . Particle-In-Cell Monte Carlo Collision

PIMS . . . . . PI-Mode Structure

PMT . . . . . Photomultiplier

PS . . . . . Proton Synchrotron

PSB . . . . . Proton Synchrotron Booster

RAM . . . . . Random Access Memory

RF . . . . . Radio Frequency

RFL . . . . . Reflected (RF power)

RFQ . . . . . Radio Frequency Quadrupole

RF-ICP . . . . . Radio Frequency Inductively Coupled Plasma

RMS . . . . . Root Mean Square

SEJ . . . . . Start EJection

SL . . . . . Super-conducting Linac

SPS . . . . . Super Proton Synchrotron

SRC . . . . . Source

ToF . . . . . Time of Flight

1 Introduction

Over the last decades we have witnessed tremendous advances in the understanding of matter at its fundamental level. Many discoveries in the field have been possible thanks to the construction of large and complex scientific instruments where physicists and engineers measured with great precision the properties of the basic constituents of matter, the elementary particles and their interactions. One of the largest scientific facilities ever built is located at the European Organization for Nuclear Research (CERN, from the French acronym Conseil Européen pour la Recherche Nucléaire). Here, proton or ion beams accelerated to nearly the speed of light are collided against each other or onto a target, and sophisticated particle detectors measure the debris left by these collisions. Analysis of these processes give physicists clues about how the particles interact, and provide insights into the fundamental laws of nature.

The particle beams required by the experiments are formed in ion sources and accelerated in so-called "particle accelerators". By using electromagnetic fields, bunches of charged particles (e.g. protons, ions) are boosted to increasing energies while being maintained in well-defined trajectories. The first stage of any particle accelerator is the ion source, responsible for producing the charged particles and impart the first acceleration by an electric field. Over the years many types of ion sources have been developed, targeted at specific particle types, currents and beam characteristics [1]. In the majority of cases, the charged particles are produced within a low-temperature plasma where intra-particle collisions and surface interactions generate the desired charged species.

Current applications set demanding requirements on the ion source performance and it becomes of paramount importance to gain a deep understanding of the underlying physical processes. This knowledge is key to engineer or identify possible improvements to the ion source configuration to reach the target performance. It is important to mention that, besides particle accelerators for high-energy physics, ion sources are employed in a multitude of applications such as the neutral beam injector of future fusion reactors, medical accelerators as well as in industrial applications like ion implantation and thin film deposition.

1.1 Scope of the thesis

This thesis is dedicated to the investigation of the ion source plasma discharge of CERN's new H^- accelerator, Linac4. Linac4 will replace the currently operating Linac2 from 2020 and will provide a higher intensity beam for CERN's experimental facilities over the next decades. The understanding of the plasma parameters in the ion source plays a crucial role in determining the processes at the origin of H^- production, allowing the assessment of design and operational parameters on the source performance.

We have developed a self-consistent simulation tool that includes the plasma heating mechanism and allows us to simulate the plasma discharge ab-initio. This tool is the first code designed for this purpose. The required verification and validation steps were achieved via convergence tests, monitoring of conservation laws and comparison to experimental results. The latter have been performed by optical emission spectroscopy at a dedicated test stand at CERN. The simulation results agree very well with experiments and demonstrate the reliability of the code to simulate the relevant plasma parameters. A subsequent parameter scan of the ion source configuration allowed investigating their effect on the plasma population densities and energy distributions, providing the mandatory insight for the optimization of the ion source.

The thesis manuscript is based on 4 papers that are reproduced in the present document, organized as follows: the remainder of chapter 1 describes CERN's accelerator complex, the need for Linac4 and its ion source. Chapter 2 is dedicated to the simulation and experimental investigation of the low-density plasma, characteristic of the initial phase of the plasma discharge. Chapter 3 describes the code developed to study the high-density steady-state plasma discharge operated during beam extraction, together with its validation by optical emission spectroscopy. In chapter 4 we performed a parameter scan of the ion source configuration to quantify their impact on the plasma parameters. Finally in chapter 5 we draw conclusive remarks and highlight guidelines for future work.

The work of this thesis comes in the framework of the Linac4 ion source work package that encompasses the design, production and test of all ion source components and of the ancillary systems. I actively contributed in the following domains that were published in scientific journals and conference proceedings:

- Ion source technical design and operation. I participated in design meetings, selection and installation of experimental equipment, operation of the ion source for the Linac4 accelerator and at a dedicated test-stand: [2, 3, 4, 5]
- Plasma and electromagnetic simulations including the development of Particle-In-Cell Monte Carlo Collision (PIC-MCC) codes, application of collision-radiative models and radio-frequency circuit modelling [6, 7, 8, 9, 10, 11, 12, 13, 14, 15, 16, 17, 18, 19, 20, 21, 22, 23]
- Optical emission spectroscopy, time-resolved photometry and fast-rise pressure mea-

surements: [24, 25, 26]. As of today, this pressure calibration is the only access to the density of neutrals in the ion source.

1.2 CERN and its accelerator complex

CERN is home of the world's most advanced scientific instruments aimed at studying the structure of matter at the atomic, nuclear and subatomic level. The basic principle consists in producing collisions between a highly energetic beam of protons or ions either against a fixed target or between two beams and observe the resulting interactions. Founded in 1954, over the years CERN has been expanding its scientific research by modernizing its facilities and increasing the beam energy in the quest for the rarest particles ever to be observed. In 1957, three years after its foundation, the organization comprised a single 600 MeV synchrocyclotron which provided beams for CERN's first experiments in particle and nuclear physics. Nowadays the accelerator complex comprises 2 linear accelerators and 6 synchrotrons, culminating in the largest and most powerful accelerator ever built, the Large Hadron Collider (LHC) with design energies up to 7 TeV capable of replicating the conditions of temperature and densities that occurred very shortly after the Big Bang.

CERN's accelerator complex is depicted in figure 1.1. It is designed to provide particle beams of different energies and intensities to dedicated experiments and facilities. The acceleration of the beams takes place in different stages. A proton beam, which is used for over 10 months a year by the complex, originates in Linac2 and after a linear acceleration to 50 MeV it is injected into the first synchrotron, the Proton Synchrotron Booster (PSB). The PSB is composed of four superimposed synchrotron rings that accelerate the beam to 1.4 GeV. This beam serves the Isotope mass Separator On-Line DEvice (ISOLDE), a radioactive ion beam facility dedicated to the study of astrophysical processes, solid state physics and medical applications of radioactive beams. The PSB beam is injected into the Proton Synchrotron (PS) for a third stage acceleration to 26 GeV. The PS beam is used by three different experimental areas: the Antiproton Decelerator (AD) where studies of the properties of antimatter are performed, the neutron Time of Flight (n-ToF) facility which investigates neutron-nucleus interactions and the east area which is a dedicated detector test facility. From the PS the beam is injected in the Super Proton Synchrotron (SPS) where it reaches 450 GeV. This beam is used by AWAKE, a proof-of-principle experiment for the study of plasma wake acceleration of electrons, HiRadMat dedicated to study the reaction of materials to high energy beam induced shocks, and a second test areas (North area). Until 2012 the SPS beam was also used to send neutrinos to Italy in an experiment called Cern Neutrinos to Gran Sasso (CNGS). At last the beam enters the LHC where it is separately injected in two counter-rotating beams. The energy of each beam can be boosted up to 7 TeV each. The LHC has 4 interaction points where the main particle detectors are installed: ATLAS and CMS are two multi-purpose detectors, ALICE is dedicated to the study of quark-gluon plasmas and LHCb to the beauty quark. CERN also provides beams of heavy ions (e.g. lead, oxygen, argon). These beams originate in Linac3 and travel to the Low Energy Ion Ring (LEIR) before entering the PS where they follow the same accelerating chain

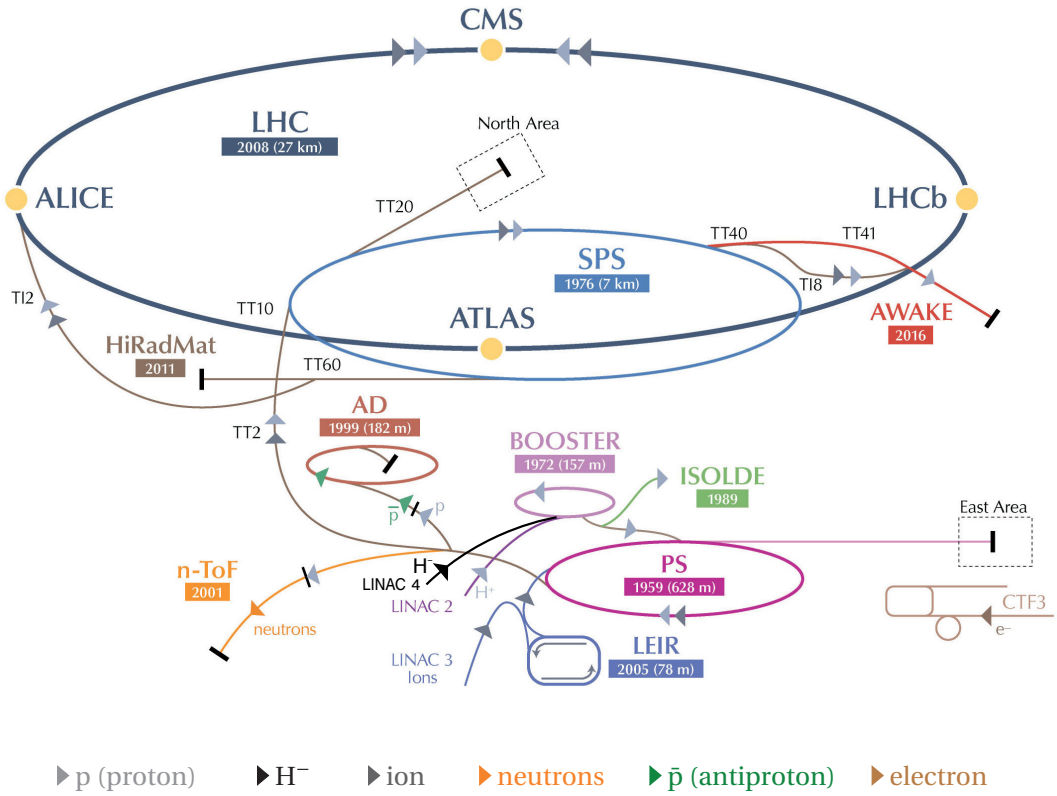

Figure 1.1 – Overview of CERN's accelerator complex. Two ion beams are currently employed: a proton beam starting its journey in Linac2, and a heavy ion one (e.g. lead, oxygen) which originates in Linac3. A test facility for electron acceleration is also present (CTF3). Image adapted from [27].

of the proton beam. The main users of the ion beams are the North Area and the LHC, where it is possible to collide proton-proton, proton-lead and lead-lead ions, allowing a wide range of fundamental processes to be investigated.

1.3 LHC's luminosity upgrade

The full exploitation of the LHC is the highest priority in the European Strategy for Particle Physics [28] and projects are already ongoing to optimize the LHC to extend its discovery potential. The performance of the LHC, or any other collider, is defined by the rate of collisions delivered to the experiments, a parameter that is known in the literature as the collider luminosity $\mathscr{L}$. In the general case of two Gaussian beams colliding head-on $\mathscr{L}$ is given by:

$$\mathscr{L} = \frac{f N_1 N_2 N_b}{4\pi\sigma_x\sigma_y} \tag{1.1}$$

where f is the revolution frequency, N_1 and N_2 the number of particles per bunch, N_b is the number of bunches and σ_x, σ_y characterize the transverse beam profile in the horizontal and vertical direction respectively. The number of particles per bunch circulating in the collider, as well as the beam characteristics do not only depend on the LHC itself, but also on the properties of the injected beam from the accelerating chain. This implies that if one wishes to increase the collider luminosity, an optimization of the full acceleration chain must be performed.

The LHC Injector Upgrade (LIU) project was therefore launched at CERN in order to coordinate the efforts required to deliver the beam characteristics for the High Luminosity LHC (HL-LHC). The goal of the HL-LHC project is to increase the LHC luminosity by a factor of 10 beyond the original design value (from 300 to 3000 fb^{-1}) around the year 2020. It was identified that one of the main improvements to the current design lies at the beam injection from Linac2 to the PSB. Due to space charge forces, the maximum intensity at injection scales proportionally to $\beta\gamma^2$ with β the ratio between the velocity and the speed of light and $\gamma = (1-\beta^2)^{-1/2}$. This implies that if one wishes to increase the maximum intensity at injection, a higher injection energy is required. Secondly, when injecting the beam from a linear to a circular machine, we can accumulate the beam over multiple turns to fill the available phase-space (position, velocity) of the machine. At injection however, there is no way to inject the incoming proton beam into the phase-space of the already circulating proton beam. This sets a limit to the number of turns achievable, which in the case of the Linac2-PSB corresponds to 13 turns. This limitation can be overcome by charge-exchange injection (section 1.4), justifying the decision to build a new H^- injector for the PSB which today materializes in the construction of Linac4.

1.4 Linac4, a new injector for the Booster

Linac4 is CERN's new 160 MeV negative hydrogen ion (H^-) linear accelerator which will replace Linac2 from 2020. The layout of the PS with its booster ring and the proton, H^- injectors is illustrated in figure 1.2. The goal of Linac4 is to double the beam intensity in the accelerator complex, by providing the suitable beam characteristics at the injection into the Booster. Linac4 accelerates H^- and uses a charge-exchange injection scheme in the PSB. (figure 1.3). When the H^- beam first arrives at the injection point it passes through a stripping foil which knocks out the electrons from the H^- leaving a proton beam circulating in the PSB. The circulating beam is now of opposite charge from the injected beam and this allows to overlap the two beams onto the same phase-space. This procedure is performed just before passing through the stripping foil, where the electrons are then removed, leaving a more intense proton beam circulating. The beam intensity is thus increased in the PSB by injecting over multiple turns. During injection, the circulating proton beam is slightly deviated from its orbit to overlap with the H^- beam. Secondly, Linac4 is designed to deliver a beam of 160 MeV, which corresponds to a factor 2 increase of $\beta\gamma^2$ compared to the 50 MeV provided by Linac2. This doubles the maximum injection intensity, leading to a similar increase in the rest of the accelerator's chain.

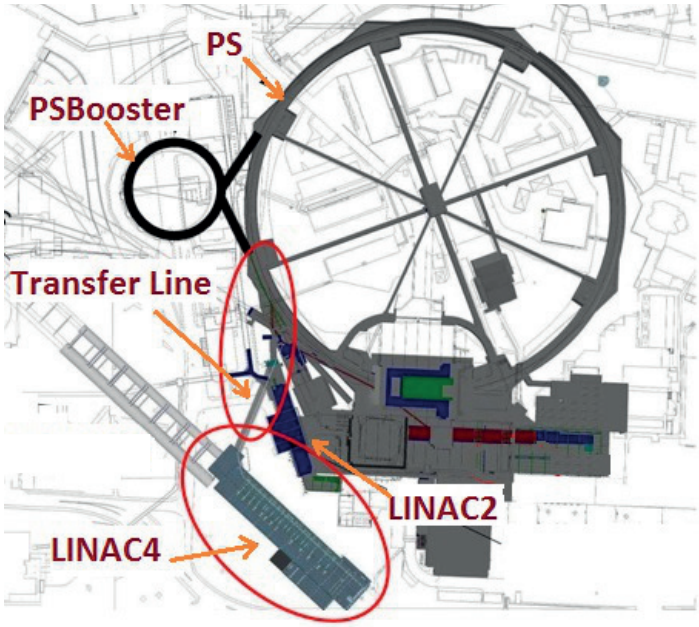

Figure 1.2 – Layout of the PS complex. The proton, H^- injectors and the PSB are indicated. At present the proton beam is injected from Linac2 to the PSB before entering the PS. This configuration will be modified in 2020 when Linac4 will provide a 160 MeV H^- beam to the PSB. The light grey at the end of Linac4 indicates a possible extension called Super-conducting Linac (SL) [29].

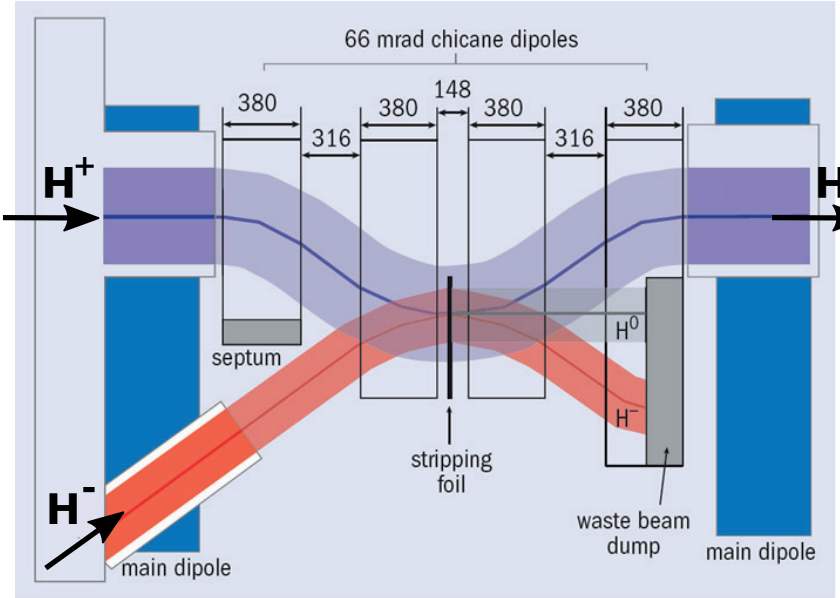

Figure 1.3 – Schematics of the charge-exchange injection. The H^- beam from Linac4 is passed through a stripping foil which leaves a proton beam circulating in the PSB. Unstripped and singly stripped H^- are dumped in a dedicated beam dump. The orbit of the circulating proton beam is slightly deviated to overlap with the injected H^- beam [30].

Linac4 is an 80 m long H^- accelerator whose schematics is shown in figure 1.4. It is composed of several accelerating structures, each designed for a specific energy range. A detailed description of the Linac4 design can be found in [30].

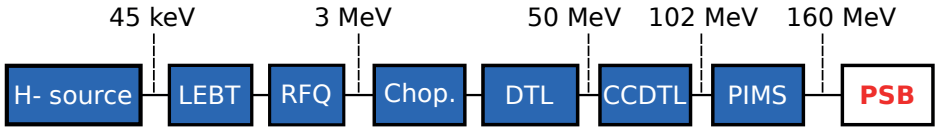

Figure 1.4 – Block diagram of the Linac4 layout with the energy delivered by each accelerating structure. From the H^- source, Linac4 is composed of a Low Energy Beam Transport (LEBT), a Radio-Frequency Quadrupole (RFQ), a chopper and buncher (Chop.), Drift Tube Linac (DTL), Cell Coupled Drift Tube Linac (CCDTL), Pi-mode structures (PIMS) before entering the Proton Synchrotron Booster (PSB).

The components of Linac4 are:

H^- ion source: The Linac4 ion source has to provide 50 mA of H^- beam at an energy of 45 keV and within an RMS emittance of 0.25 π mm mrad. A detailed description of the ion source and its operational principle follows in section 1.6.

Low Energy Beam Transport (LEBT): its role is to match the beam characteristics from the source to the entrance of the next accelerating structure, the Radio-Frequency Quadrupole (RFQ). It is composed of two solenoids and four steerers for a total length of 1.2 m. Between the two solenoids beam diagnostics are installed to monitor the source and characterize the beam.

Radio-Frequency Quadrupole (RFQ): The RFQ serves the multiple purpose of accelerating, focusing and bunching (separating in "micro-pulses") the beam. It is composed of 4 vanes (figure 1.5), each modulated with a characteristic wavelength proportional to the particle's velocity. The four vanes shape the 352 MHz RF field to produce an electromagnetic field both on the longitudinal direction (accelerating and bunching) as well as in the perpendicular direction (focusing). The RFQ accelerates the beam from 45 keV to 3 MeV.

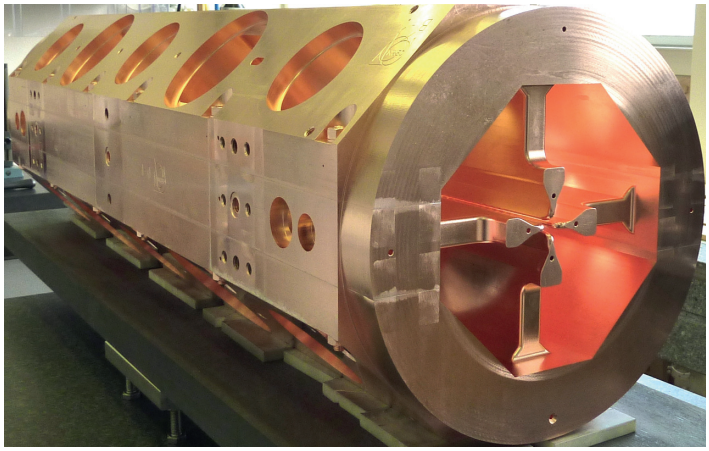

Figure 1.5 – The 352 MHz Radio-Frequency Quadrupole (RFQ) with the characteristic 4 vanes structure.

Chopper and buncher (Chop.): The purpose of the chopper is to select only the sequence of beam bunches that will be accepted by the PSB. As the PSB is composed of 4 superimposed rings, it is highly desirable to allow a beam free switch between the rings. Since beam losses at the injection energy of 160 MeV can induce significant radiation, it is preferable to stop the unmatched bunches at lower energy of 3 MeV. The chopper is composed of two fast-switching electrostatic plates which are powered to deflect the unwanted bunches onto a beam dump. The buncher is composed of a set of RF cavities that affect the beam in the longitudinal direction allowing an improved bunching structure.

Drift Tube Linac (DTL): A DTL is composed of a series of metallic drift tubes separated by gaps as shown in figure 1.6. The metallic rings shape the RF field to produce an electric field in the gaps, accelerating the H^- ions during their transit. By Faraday screening the field in the metallic drift tube is shielded during the reversed polarity phase, in order to avoid a

decelerating force on the beam. The length of the drift tubes and the gaps is proportional to the particles velocity and therefore increase in length with increasing energy. Furthermore, the drift tubes are equipped with quadrupole magnets to compensate for the defocusing space charge forces. One peculiarity of the Linac4 DTL is the use of permanent magnets for the first short drift tubes, in contrast to conventional electromagnets. After the DTL, composed of 108 drift tubes, the beam reaches an energy of 50 MeV.

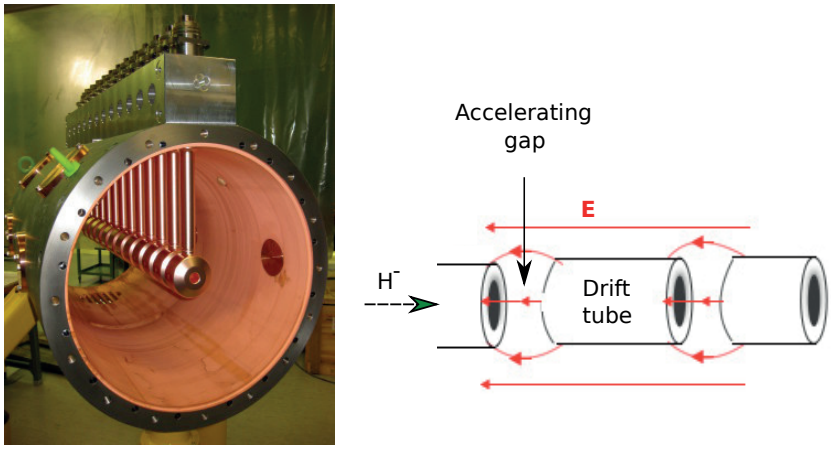

Figure 1.6 – Left) picture of one of Linac4 DTL modules. Right) working principle of a DTL, the particle acceleration takes place within the gaps with a force $\vec{F} = q\vec{E}$ ($q = -1$ for H^-). The electric field is shielded in the metallic drift tubes.

Cell Coupled Drift Tube Linac (CCDTL): With increasing energy the space charge forces become less severe. This allows a design of tanks containing a set of two drift tubes while the focusing elements (quadrupoles) are placed between tanks (figure 1.7). The main advantage of this design is a simpler construction and alignment, which in turns implies a lower price per meter as compared to a DTL. The CCDTL increases the beam energy to 102 MeV.

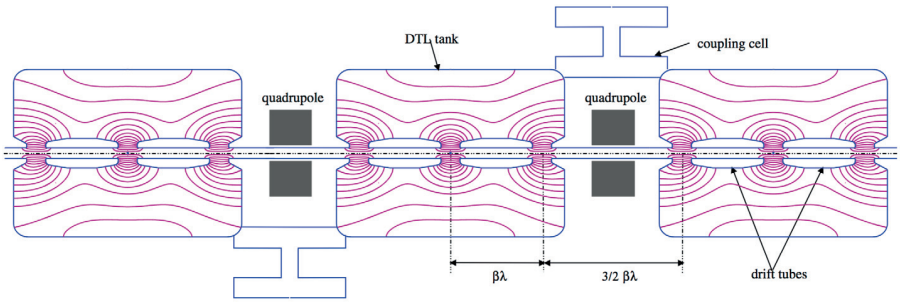

Figure 1.7 – Structure of the CCDTL with the electric field lines indicated. The quadrupole magnets are installed between tanks.

Pi-mode structures (PIMS): PIMS are so-called because they accelerate the beam every half period of an RF cycle (π radians). As in drift tubes, the acceleration is performed within the gaps of the cavities. In Linac4 there are 12 seven-cell PIMS bringing the energy from 102 to 160 MeV. A schematic of a PIMS is shown in figure 1.8.

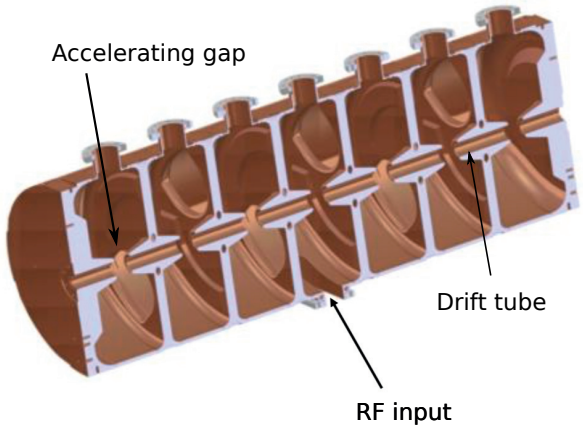

Figure 1.8 – Schematics of one of the 12 seven-cell PIMS of Linac4.

The Linac4 connects to the PSB via a 70 m long transfer line from the end of Linac4 to the charge-exchange injection into the PSB as shown in 1.2.

1.5 Fundamental processes of H^- formation

At the origin of Linac4 lies the ion source which is responsible to produce the initial H^- beam. An H^- is a neutral hydrogen atom with an additional electron attached. The binding energy of the additional electron is called electron affinity and in hydrogen it corresponds to 0.754 eV. This value is particularly small compared to the 13.6 eV binding energy of the primary electron bound to the nucleus. Consequently, in a plasma H^- are very fragile and collisions with other particles can be very efficient in detaching the additional electron. For an ion source, this has the important consequence that only the H^- produced in the proximity of the beam formation region will effectively contribute to the beam, while the others will likely be destroyed before reaching it. The production and destruction processes of H^- have extensively been studied since the 70's, both theoretically and experimentally. There are two main paths of production, called volume [31] and surface production [32].

1.5.1 H⁻ volume production

In the so-called volume production, H^- are formed by electron-impact collisions in the volume of the plasma. The most efficient production channel is the Dissociative Attachment (DA) of low energy electrons to vibrationally excited molecules [33]:

$$e + H_2(v) \rightarrow H^- + H \tag{1.2}$$

The vibrational level v of the hydrogen molecule has a drastic influence on the DA production cross-section σ_{DA} (figure 1.9). The peak value for $v = 0$ is only in the order 10^{-25} m^2, but it increases by 6 orders of magnitude for $v = 9$. Furthermore, the threshold energy of σ_{DA} decreases with increasing v, implying that low energetic electrons are very efficient in producing H^- via DA.

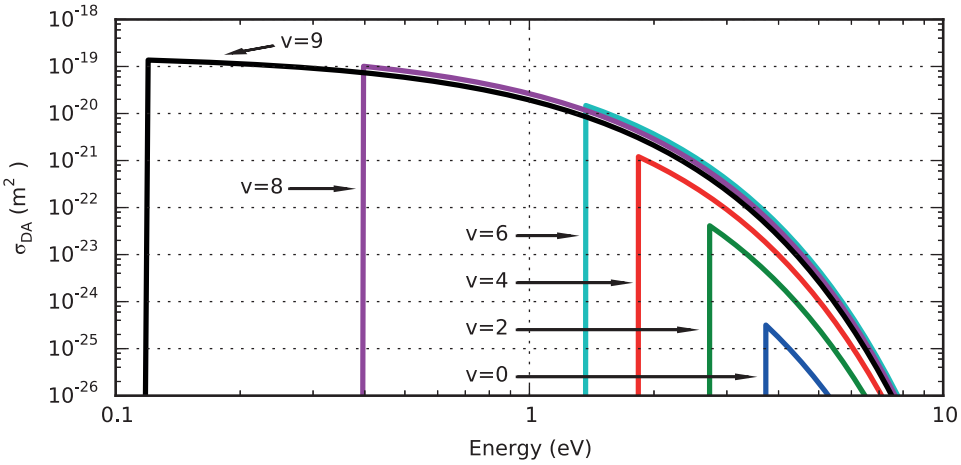

Figure 1.9 – Dissociative attachment (DA) cross section as a function of the molecular vibrational level v. Data taken from [34].

From equation 1.2 it is clear that a large population of vibrationally excited molecules is required to enhance the H^- volume production. The molecular vibrational excitation can also proceed via electron-impact processes. The two most efficient channels are via an H_2^- resonant state and by radiative decay from the singlet electronic excited states of H_2.

$$e + H_2(v) \rightarrow H_2^- \rightarrow e + H_2(v') \quad v' > v \tag{1.3}$$

$$e + H_2(v) \rightarrow e + H_2^* \rightarrow e + H_2(v') + h\nu \quad v' > v \tag{1.4}$$

The resonant process described by equation 1.3 is effective at producing vibrational excitation even with low energetic electrons, but the most probable transition is for a vibrational change $\Delta v = 1$. The population of high vibrational levels must therefore proceed via a multi-step process, requiring a large collision frequency. The cross-section for the transition v=0 to v=1 is shown in figure 1.10.

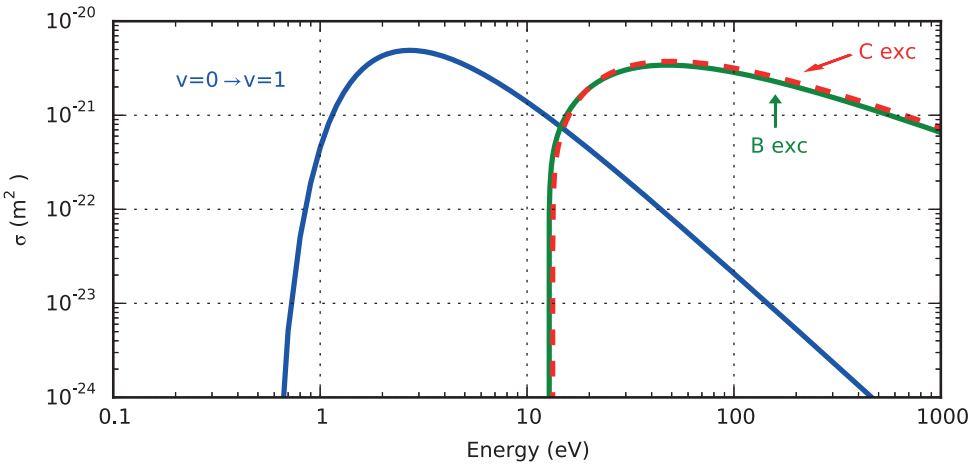

Figure 1.10 – Cross-section of the resonant reaction described by equation 1.3 for the transition $v = 0 \rightarrow v = 1$ and of the B, C electronic excitation of $H_2(v = 0)$ described by equation 1.4.

The radiative process described in equation 1.4 can excite molecules directly from the ground state to a high vibrational level. Among the singlet state, the B and C electronically excited states have the largest electron-impact cross sections and their radiative transition are also the largest [34]. The transition probabilities as a function of the vibrational state can be found in [35]. The peak value of the B and C excitation is comparable to the resonant process 1.3, but due to the threshold energy of excitation, this reaction only takes place for electron energies > 12.7 eV as illustrated in figure 1.10.

Another path to populate vibrationally excited molecules is atomic recombination on the wall. Depending on the material, temperature and surface vibrational levels up to 9 have been reported [33].

1.5.2 H^- surface production

The basic principle of H^- surface production is the transfer of an electron from the surface to an atom leaving the surface. The electron transfer can be enhanced by lowering the work function of the surface. This can be achieved by depositing an alkali on a metallic surface. Classical coverages include Cesium on Tungsten (Cs-W) and Cesium on Molybdenum (Cs-Mo).

Different physical process are responsible for production of H^- on the surface: backscattering of hydrogen ions (H_x^+), backscattering of a thermal or suprathermal distribution of hydrogen atoms, sputtering of adsorbed hydrogen by cesium or hydrogen ion bombardment [36]. The H^- yield Y, defined as the ratio between the flux of H^- leaving the surface and flux of impinging particles, depends on the energy of the incoming flux and the surface work function. As an example, the yield due to backscattering of impinging ions or atoms can be estimated as

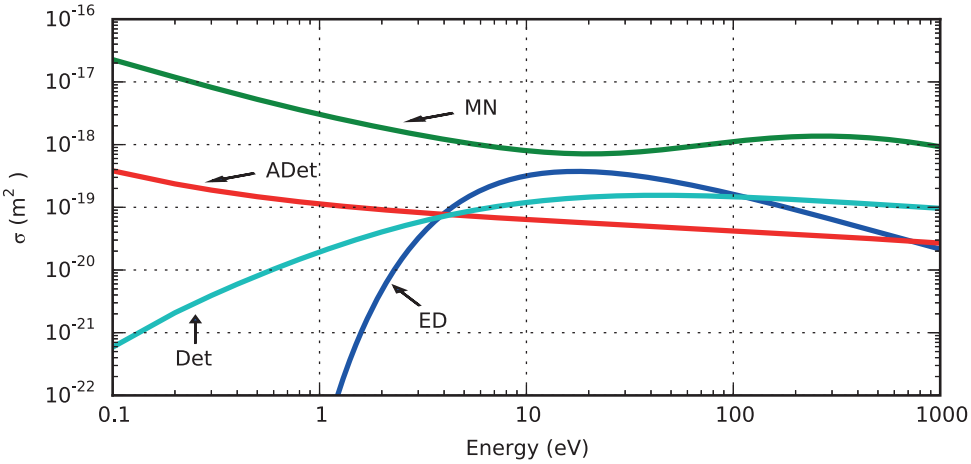

Figure 1.11 – H^- destruction processes. The energy value corresponds to the center of mass for Associative Detachment (ADet), non-associative Detachment (Det) and Mutual Neutralization (MN), whereas lab frame is used for Electron Detachment (ED) [34].

[37, 38]:

$$Y(E_{in}) = R_N \eta_0 \left(1 - \frac{(\phi - E_A)/R_E}{E_{in}}\right) \tag{1.5}$$

With E_{in} the kinetic energy of the impinging particle, R_N the particle reflection coefficient, η_0 the probability of reflection as an H^-, ϕ the surface work function, E_A the electron affinity and R_E the energy reflection coefficient. For a cesiated Molybdenum surface, the recommended values deduced from experimental data [37] are $R_N\eta_0 = 0.42$ and $R_E = 0.71$. From equation 1.5 we can observe that the optimal conditions to achieve a large H^- yield Y are a low surface work function and a high energetic flux of atoms or ions.

1.5.3 H^- destruction processes

The destruction processes of H^- can proceed mainly via four channels:

$$H^- + H^+ \rightarrow H + H \quad (MN) \tag{1.6}$$
$$H^- + e \rightarrow e + H + e \quad (ED) \tag{1.7}$$
$$H^- + H \rightarrow H_2 + e \quad (ADet) \tag{1.8}$$
$$H^- + H \rightarrow H + H + e \quad (Det) \tag{1.9}$$

By far the most important process is Mutual Neutralization (MN) with a cross section reaching 10^{-17} m^2 (figure 1.11). Electron Detachment (ED) is also efficient for electron energies of 10-20 eV, indicating that highly energetic electrons are detrimental to achieve a large population of H^-. Associative Detachment (ADet) and non-associative Detachment (Det) proceed without threshold energy and can be efficient destruction channels when the atomic density is large.

An efficient H^- ion source will therefore require a combination of a heating region, where hydrogen dissociation and vibrational excitation take place, and a cold region where H^- are formed via DA and surface conversion. This can be achieved by interposing a magnetic filter field between the two regions [39], leading to a decrease of the electron energy and density via collisional diffusion towards the beam formation region. Beam formation simulations [40] indicate that typical H^- densities in the Linac4 ion source correspond to an order 10^{17} m^{-3} from volume production and a surface emission in the range 300-3000 A/m^2.

It is important to notice that the optimality conditions in volume or surface mode have opposite requirements in terms of neutral populations, i.e. the atomic n_H and molecular n_{H_2} densities. Volume mode requires a large population of vibrationally excited molecules (thus low dissociation degree $n_H/(n_H + n_{H_2})$), whereas surface production requires a large dissociation degree to maximise the atomic flux onto the low work function surface.

1.6 Linac4 ion source

The Linac4 H^- ion source [5] is required to deliver 50 mA of H^- at 45 keV within an RMS emittance of 0.25 mm mrad and in pulses of 600 μs with a repetition rate up to 2 Hz. The ion source configuration is shown in figure 1.12. It is composed of a plasma generator in which H^- are produced, and an extraction system aimed at forming and accelerating the beam.

The plasma generator comprises a cylindrical plasma chamber made of Aluminium Oxyde (Al_2O_3) or Aluminium Nitrate (AlN) with a radius of 24 mm and a length of 138 mm. The plasma is heated by a 5 turn solenoid coil which is surrounded by 6 ferrites and embedded in epoxy to avoid RF breakdown. An external cusp magnet in Hallbach configuration surrounds the plasma chamber with the aim of minimizing electron losses to the wall. A dipole filter field is installed between the coil and the beam formation region to enhance H^- production and minimize their destruction (see section 1.5). On the plasma chamber flange 5 inlets are installed: a gas delivery pipe from which hydrogen is injected in pulsed mode by means of a piezo-valve; 3 optical view ports oriented on the plasma chamber axis, at 19 deg and 26 deg with respect to it, and a Cs delivery line used to distribute Cs onto the Mo plasma electrode in order to reduce its effective work function and therefore enhance the H^- surface production. The plasma electrode is perforated with a diameter of 6.5 mm, from where the H^- beam is extracted. The plasma generator is held on the main flange which is connected to a -45 kV power supply.

The extraction system comprises three electrodes aimed at forming and shaping the beam for the next accelerating stage: a puller-dump set to +10 kV with respect to the plasma generator, a ground electrode and an Einzel lens set to +45 kV [41]. The purpose of the puller-dump is twofold, as indicated by its name. Its potential difference with respect to the main flange creates an electric field that "pulls" negative charges (electrons and H^-) from the plasma, thus forming the initial beam. Secondly, as electrons are unwanted by-products, it "dumps" them onto a titanium plate by means of a dipole magnetic field. The H^- due to their larger masses

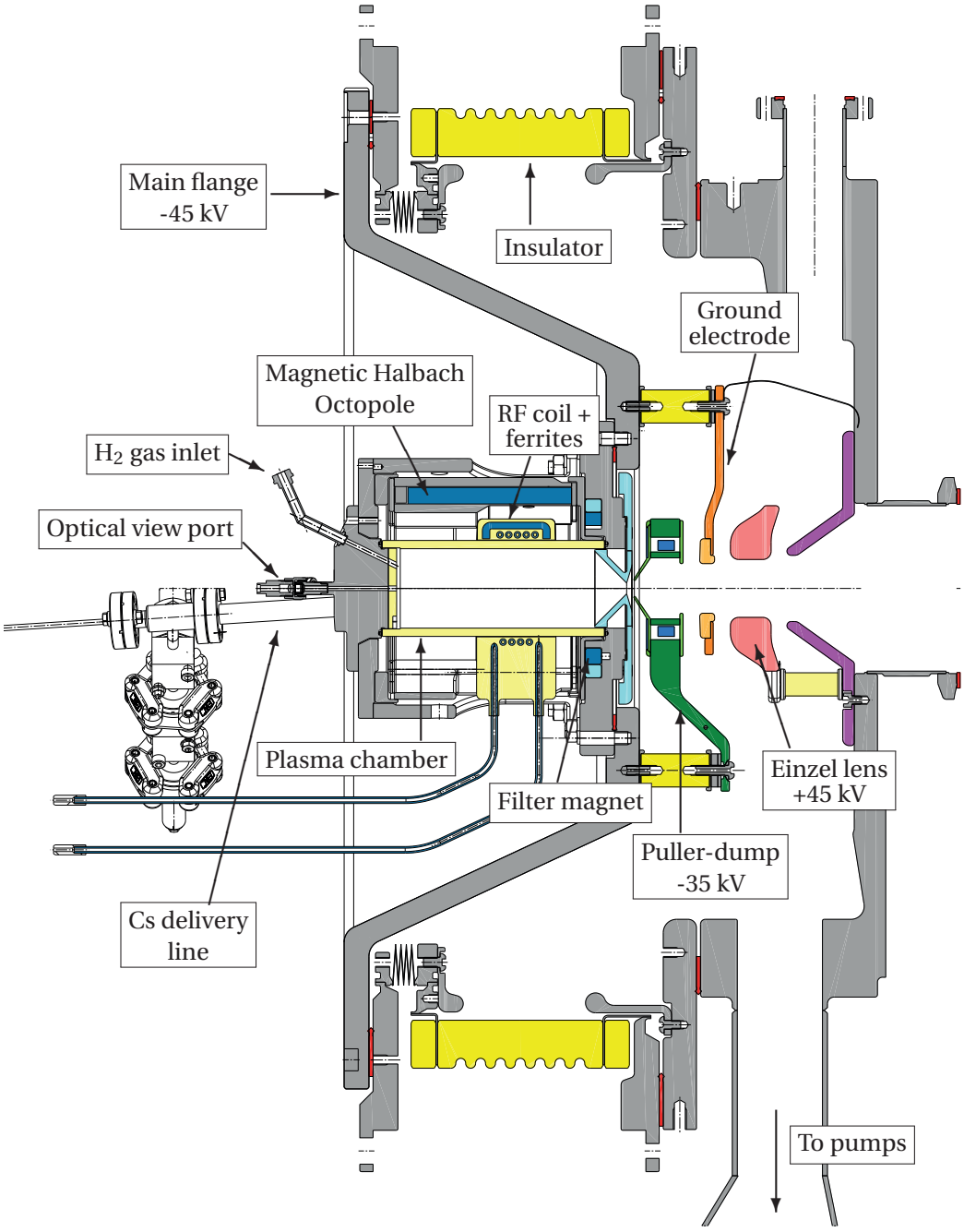

Figure 1.12 – Cross-sectional view of the Linac4 H^- ion source with its plasma generator and extraction system.

are only slightly affected on their trajectory and continue on their journey. The ground electrode imparts the full energy to the H^- beam that reaches 45 keV at this stage. The last electrode is the Einzel lens, which is used for shaping the beam for the Low Energy Beam Transport (LEBT). Here two solenoids are used to match the beam characteristics for injection into the RFQ.

1.6.1 Ion source operation

The Linac4 H^- ion source is operated in pulsed mode, based on the Start EJection (SEJ) trigger signal issued by the PSB. SEJ defines the time at which the H^- beam is ejected from the Linac4 and injected into the PSB. This implies that the ion source must be ready to deliver the H^- at SEJ minus the Time of Flight (ToF) of the beam from the source to the PSB, with ToF = 2 μs.

To that extend, a sequence of timings triggers each ion source sub-system as illustrated in figure 1.13. The gas injection is controlled by a piezo-valve, which opens 2.5 ms before SEJ for a duration of 0.5 ms. This timing allows the gas to expand into the plasma chamber, reaching a pressure of 3 Pa during the plasma pulse [26]. The High Voltage (HV) power-supplies (source, puller-dump and Einzel lens) are all triggered simultaneously, starting 0.6 ms before SEJ for a duration of 1.35 ms. The plasma pulse is controlled by the RF power signal, which is typically switched on 0.1 ms before SEJ in order to allow sufficient time for the plasma to reach steady state. The RF pulse lasts typically 0.7 ms.

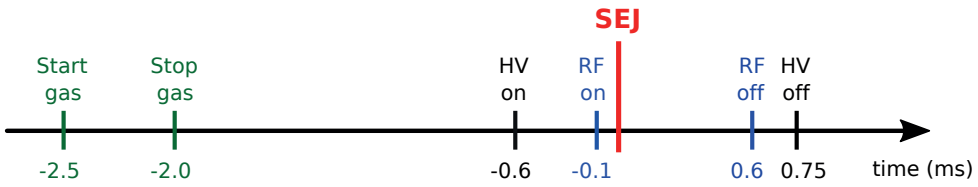

Figure 1.13 – Sequence of trigger signals of the Linac4 H^- ion source.

A typical pulse structure is shown in figure 1.14. The HV ramps to its target value in approximately 0.5 ms, stabilizing at flat-top before the plasma is ignited. The flat-top value is maintained throughout the duration of the pulse with a stability within 1% [42]. The RF power is delivered to the plasma by a 2 MHz, 100 kW peak power amplifier. Three signals are recorded: the forward power (FWD) representing the power delivered by the RF amplifier, the reflected power (RFL) indicating the amount of power not absorbed by the system, and the delivered power (DEL) which is the difference FWD-RFL. A minimization of the RFL power is achieved by tuning the RF frequency in the range 1.9-2.1 MHz, matching the total impedance to the 50 Ω of the RF amplifier [43]. The ion source currents are measured by a current transformers installed in the HV racks. The puller-dump (PD) current corresponds to the amount of electrons dumped on the electrode. By design [42] the PD current is fed back to the source power supply, implying the measured source current corresponds to the H^- current

leaving the source plus any residual electron current undumped on the PD. The Einzel Lens (EL) current monitors the component of the beam that hits the electrode and it is typically very low. The beam current is measured in the LEBT either by a beam current transformer during nominal operation or by a Faraday cup during testing.

The Linac4 ion source can operate in two H^- production modes as described in section 1.5. When operated in volume mode (i.e. without the addition of Cs) the source reached 30 mA of H^- current [4] with extracted electron to ion ratio e/H^- ≈30. With the addition of Cs evaporated on the Mo plasma electrode, H^- currents up to 60 mA have been recorded with a significant reduction of the e/H^- to ≈ 2. The ion source is operated with a plasma duty cycle of 0.1%. Due to plasma surface interactions, the deposited Cs layer has a lasting effect of about 1 month after which the H^- current gradually reduces accompanied by an increase of the e/H^-. At this time, a new cesiation is performed to re-establish the optimal conditions.

The e/H^- has two major implications on the ion source performance. Firstly, the power deposited by the electron beam onto the puller-dump should not exceed the surface sublimation threshold of the electrode's material. For a beam of 700 μs this corresponds to approximately 1 kW/mm^2 for Tungsten and 0.2 kW/mm^2 for Titanium, setting a maximum electron current of 1.2 A and 240 mA respectively [41, 44]. This indicates that, even if the ion source were to provide 50 mA H^- beam in volume mode, a factor 30 e/H^- would prevent operation due to the thermal load on the puller-dump. Secondly, the electron beam contributes to the space-charge forces of the H^- beam. For the operation of the Linac4 H^- ion source an $e/H^- \leq 8$ is deemed sufficient to limit the space charge forces induced by the co-extracted electron beam.

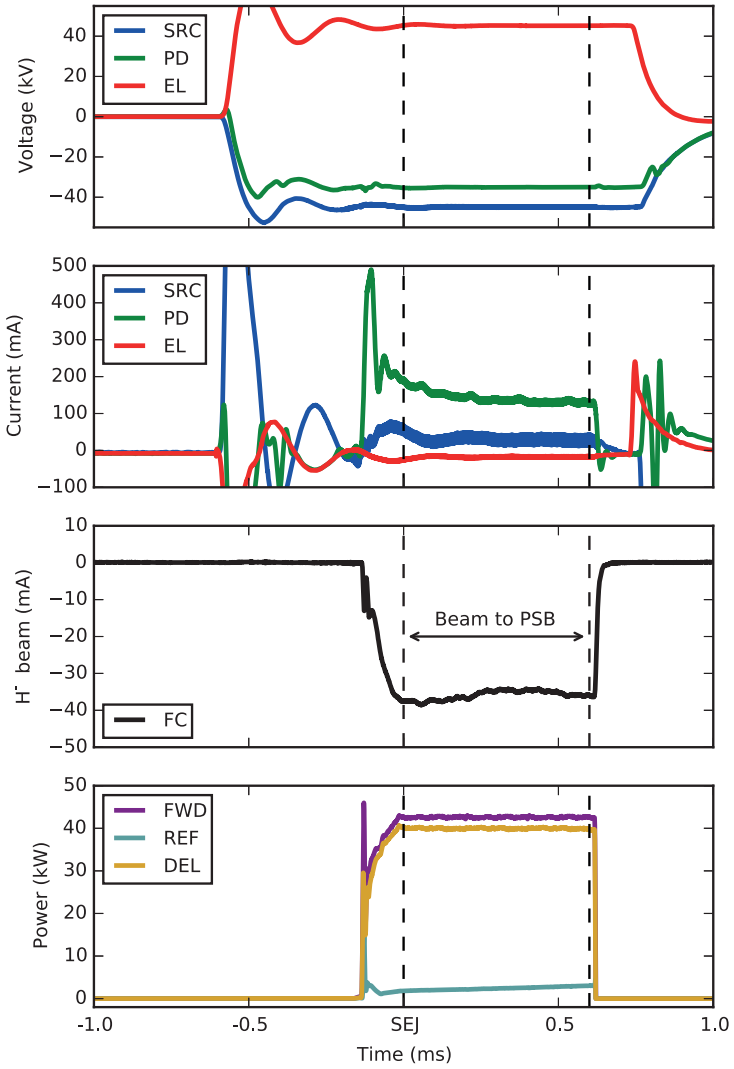

Figure 1.14 – Typical pulse structure of the Linac4 ion source. The top two plots show the voltage and current of the source electrodes: source (SRC), puller-dump (PD) and Einzel Lens (EL). The H^- beam is measured by a beam current transformed or a Faraday Cup (FC) installed in the LEBT. The RF power signals (bottom plot) refer to the forward (FWD), reflected (RFL) and delivered (DEL) power, with DEL=FWD-RFL.

2 Simulation and experimental validation of a low density plasma

The plasma heating mechanism of the Linac4 H^- source is based on electromagnetic induction. When a time-varying current flows through its external solenoid coil, a time-varying magnetic field is produced which oscillates in the axial direction. This in turn induces an electric field in the azimuthal direction that accelerates electrons and ions in the plasma chamber. If sufficient energy is imparted, collisions with the neutral gas will lead to ionization and thus to the sustainment of the plasma. Due to the operating frequencies and the plasma heating geometry, these discharges are called Radio-Frequency Inductively Coupled Plasmas (RF-ICP).

Interestingly, the same geometry also provides capacitive coupling to the plasma. In order to flow an RF current I_{RF} in the coil, an RF voltage V_{RF} must be applied between the two coil ends. The value of V_{RF} can be estimated as [45]:

$$V_{RF} \approx L\omega_{RF} I_{RF} \tag{2.1}$$

with ω_{RF} the angular frequency and L coil inductance. For the Linac4 ion source this corresponds to $V_{RF} \approx 3800$ V for $L = 3$ μH and $I_{RF} = 100$ A. The electric field due to V_{RF} is known to drive the first plasma discharge from ignition to a low plasma density plasma [45]. In analogy to electrostatically driven discharges, this operating regime is called electrostatic mode (E-mode). When the density increases, the plasma screens the electric field due to V_{RF} and induction drives the heating process. From the symbol associated with induction this operating mode is known as H-mode.

The operation of the Linac4 ion source requires to form a new plasma at each pulse. During the first few μs of the RF pulse, the plasma ignites and undergoes a rapid transition from the E to the H-mode while the RF power is ramped-up. In order to investigate the plasma dynamics during the E-H transition and to characterize the effect of design and operational parameters, we have performed a numerical study and compared its results with experiments. This work has been published on a peer-reviewed journal, reported here. The agreement between simulations and measurements is a very positive sign that the relevant processes are included in the simulations.

2.1 Publication 1: Kinetic simulations and photometry measurements of the E-H transition in cylindrical inductively coupled plasmas

S Mattei[1,2], K Nishida[3], S Mochizuki[3], A Grudiev[1], J Lettry[1], M Q Tran[2], A Hatayama[3]

[1] CERN, CH-1211 Geneva 23, Switzerland
[2] Swiss Plasma Center, EPFL, Station 13, CH-1015 Lausanne, Switzerland
[3] Faculty of Science and Technology, Keio University, 3-14-1 Hiyoshi, Kohoku-ku, Yokohama 223-8522, Japan

Plasma Sources Science and Technology, Volume 25, Number 6, 2016
doi: 10.1088/0963-0252/25/6/065001
http://stacks.iop.org/0963-0252/25/i=6/a=065001

The paper was reformatted for uniformity and the references integrated into the thesis' bibliography, but otherwise the content remains unchanged.

2.1.1 Abstract

Inductively Coupled Plasmas (ICP) are well known to exhibit two modes of operation: a low density capacitive E-mode and a high density inductive H-mode. In this study we investigate the E-H transition in a cylindrical ICP, and show the effect of an external magnetic cusp field on the transition dynamics. The plasma is simulated by an Electro-Magnetic Particle-In-Cell Monte Carlo Collision code in order to take into account spatio-temporal variations of the plasma dynamics as well as kinetic effects. Simulations are compared to photometry measurements on the Linac4 H^- ion source plasma chamber. We show that the E-H transition is characterized by strong spatial variations of the plasma parameters, with an axial plasma oscillation in E-mode followed by a centring in the coil region in H-mode. The external magnetic cusp field prevents electrons close to the wall to be accelerated and reduces the inductive power deposition in the plasma. This resulted in a $\approx 50\%$ higher current to achieve E-H transition compared to the configuration without cusp field. The results indicate possible improvements to the magnetic cusp field configuration in order to achieve optimal power transfer.

2.1.2 Introduction

Inductively Coupled Plasmas (ICP) are routinely used in many applications ranging from integrated circuit manufacturing to medical devices [46, 47]. Two modes of operation are typically supported by ICPs. In the low density regime, the high voltage across the coil couples

to the plasma capacitively (E-mode), while in high density the discharge is sustained by the electric field induced by the Radio Frequency (RF) current in the coil [45].

Previous studies [48, 49, 50] have shown that a sharp transition occurs between these two modes (E-H) if a sufficiently high current is driven through the coil. During the transition a sudden jump of the electron density and light emission is observed, accompanied by a modification of the Electron Energy Distribution Function (EEDF) [51]. Phase and space resolved optical emission spectroscopy measurements in planar ICPs showed the importance of the plasma spatial distribution in understanding the E-H transition [52]. This was also observed in Langmuir probe measurements and investigated as a function of the gas pressure [53]. Fluid simulations of the E-H transition were also performed in planar ICPs highlighting the spatial variations in the the two modes [54]. Numerical simulations of cylindrical ICPs, on the other hand, have only been performed in either E- or H-mode [11, 23], while the detailed description of the E-H transition has not yet been performed. Also, albeit external magnetic fields are commonly employed in conjunction with ICPs, their effect on the E-H transition dynamics requires further investigation. This finds particular importance in the operation of pulsed discharges, as the E-H transition occurs at the beginning of each pulse during the RF power ramp-up where an optimal power transfer is required.

In this study we investigate the E-H transition in a cylindrical ICP and show the effect of an external magnetic field on the transition dynamics. We have simulated the discharge with an Electro Magnetic Particle-In-Cell Monte Carlo Collision (EM-PIC-MCC) code in order to self-consistently take into account spatio-temporal variations of the plasma parameters as well as kinetic effects. The results are compared to photometry measurements performed on the plasma chamber of the Linac4 H^- ion source at CERN [5]. Our goal is to determine under what conditions the discharge evolves from a low density to the E-H transition and suggest possible optimizations to the magnetic field configuration to achieve optimal power transfer.

2.1.3 Geometry and numerical model

Our investigation is carried out on the plasma chamber of the Linac4 H^- ion source [5], which geometry is shown in figure 2.1. The hydrogen plasma is formed in a Al_2O_3 cylindrical chamber with diameter 48 mm and length 136 mm. A 5 turn coil, surrounded by 6 ferrites, is installed around the plasma chamber and it is operated at 2 MHz with an available peak power of 100 kW (maximum 300 A coil current). The plasma is ignited for 500 μs with a repetition rate up to 2 Hz. Hydrogen is injected by a piezo valve in pulsed mode. The magnetic configuration comprises a magnetic octupole field in Halbach configuration [55] and a dipole filter field. Three optical view ports are mounted on the back side to capture the light emitted by the plasma, pointing to: the plasma chamber axis, the center of the solenoid and the plasma electrode.

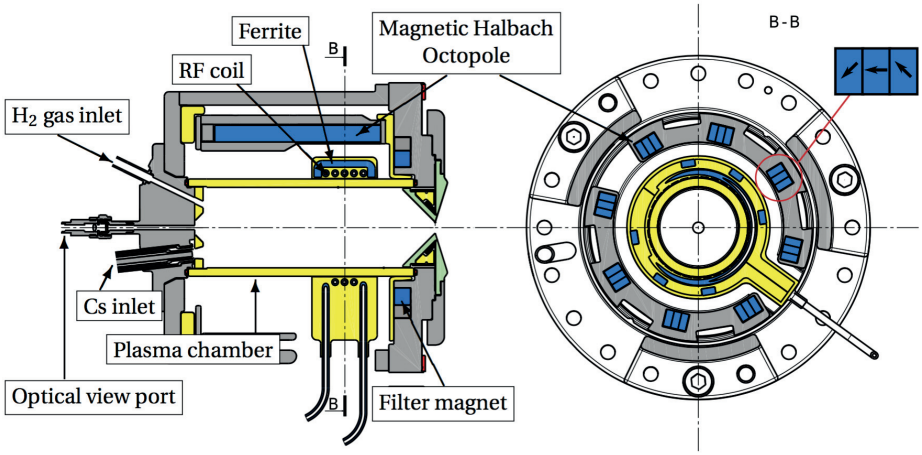

Figure 2.1 – Longitudinal and transversal cross-section of the Linac4 H^- ion source plasma generator. The plasma chamber is made of Al_2O_3. The RF coil is surrounded by 6 ferrites and embedded in epoxy to avoid RF breakdown. Gas is injected in pulsed mode by a piezo-valve. The optical view port has a capture angle of 3°. The magnetic Halbach octupole is formed by alternating magnets with clockwise and counter-clockwise magnetization. The filter field is a dipole magnet with vertical magnetization. The Cesium inlet is used to evaporate Cs onto the plasma electrode for the source operation, but it is unemployed in the present study.

Numerical model

The aim of our simulations is to characterize the plasma evolution during the E-H transition. We employ the combination of our EM-PIC-MCC, coupled with two commercial software applications for the simulation of the external electromagnetic fields - Ansys HFSS for the RF fields in vacuum and Opera VectorFields for the magnetic octupole, described later.

The EM-PIC-MCC is a 2.5 D code in cylindrical coordinates, meaning that the electromagnetic fields generated by the plasma ($\boldsymbol{E_{pl}}, \boldsymbol{B_{pl}}$) are solved in 2D assuming axisymmetry ($\partial/\partial\theta = 0$) while the particle motion is fully 3D. The code is the one employed in [11], supplemented with the routines to couple the external magnetic field. The simulation domain is shown in figure 2.2. Specifically $\boldsymbol{E_{pl}}, \boldsymbol{B_{pl}}$ are solved with the Finite Difference Time Domain (FDTD) method [56] with absorbing boundary conditions: Mur [57] at the axial boundary, while Bayliss and Turkel [58] at the radial boundary. The dimensions of the simulation domain are twice the plasma chamber size to avoid large reflections at the boundary. The particle motion is solved by the Boris-Buneman version of the Leap-Frog method [59] and weighting to the grid is performed using a volume ($r^2 - z$) bilinear interpolation function with volumes treated following Verboncoeur [60]. Particles reaching the boundary of the plasma chamber are removed from the computation. The simulated plasma is composed by electrons, protons

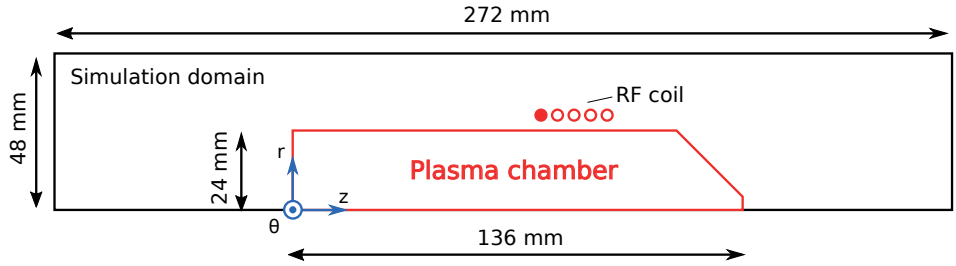

Figure 2.2 – Simulation domain and inner dimensions of the plasma chamber. The simulation domain is twice the plasma chamber to avoid large reflections at the boundary. The RF coil position is indicated, in which the filled dot represents the high voltage connection while the opposite end is grounded.

and molecular ions (H_2^+), initially loaded uniformly in the plasma chamber. The plasma current $\boldsymbol{j}$ required for the calculation of $\boldsymbol{E_{pl}}, \boldsymbol{B_{pl}}$, is the average value in the θ direction. Cell size and time step are chosen to satisfy the stability conditions of the EM-PIC scheme [59]. Electron-neutral and electron-ion collisions are taken into account by a Null-Collision Monte Carlo method [61] while Coulomb collisions are neglected in the present study. This choice follows since the e-neutral collision frequency is much larger than Coulomb collision one for the H_2 pressures (1-10 Pa) and plasma densities ($< 10^{16}\ m^{-3}$) simulated [16]. The sampling of the Null collisions is performed for each cell and cross sections are taken from [34]. The neutral gas is treated as a background gas.

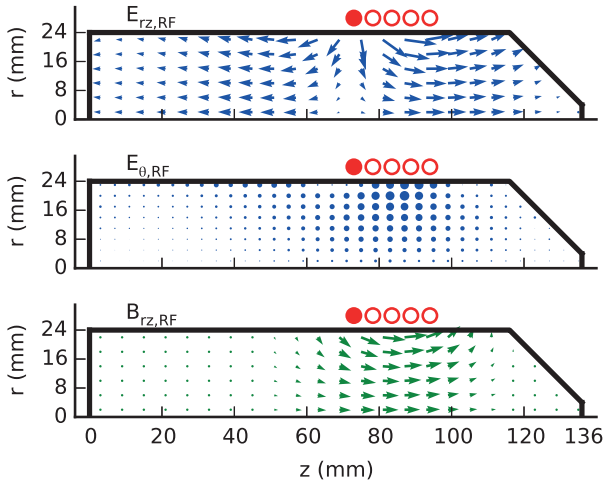

Figure 2.3 – Distribution of the vacuum electromagnetic fields $\boldsymbol{E_{RF}}, \boldsymbol{B_{RF}}$ in the r,z plane. top: $E_{rz,RF}$, middle: $E_{\theta,RF}$, bottom: $B_{rz,RF}$. The RF coil position is indicated, in which the filled dot represents the high voltage connection while the opposite end is grounded. For reference the fields for a coil current $I_{RF} = 130A$ results in maximum values of: $E_{r,RF} = 45.8\ kV/m$, $E_{\theta,RF} = 2.1\ kV/m$, $E_{z,RF} = 62.5\ kV/m$, $B_{r,RF} = 9.1\ mT$, $B_{\theta,RF} = 0$, $B_{z,RF} = 16.9\ mT$.

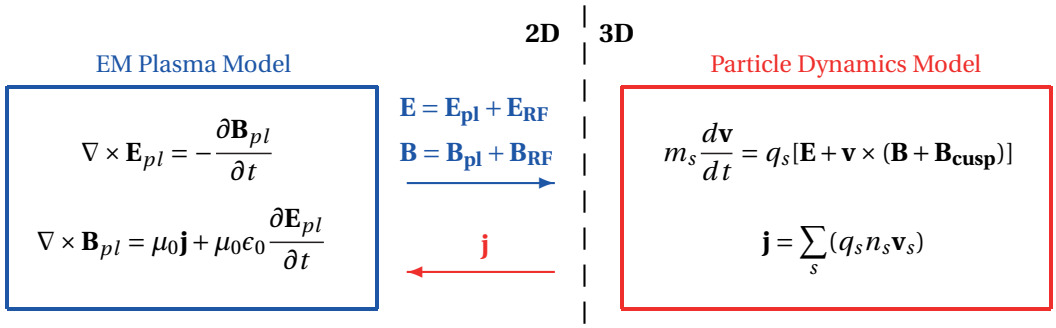

Figure 2.4 – Computational cycle performed at each time step. The plasma current $\boldsymbol{j}$ is the sum of electrons, protons and H_2^+ contribution (index s). Weighting from the particle to the grid (and vice-versa) as required by the PIC algorithm is implied. The transition between the 3D to the 2D is performed by averaging in the θ direction.

The RF electromagnetic fields in vacuum ($\boldsymbol{E_{RF}}, \boldsymbol{B_{RF}}$) are simulated in the frequency domain by Ansys HFSS, starting from the ion source 3D model with its respective material properties. Details of the simulations are described in [21]. From HFSS we export a field map of $\boldsymbol{E_{RF}}, \boldsymbol{B_{RF}}$ that we average in the θ direction. Figure 2.3 shows the distribution of $\boldsymbol{E_{RF}}, \boldsymbol{B_{RF}}$ in the plasma chamber. The static magnetic field of the Halbach octupole ($\boldsymbol{B_{cusp}}$) is simulated with Opera VectorFields and exported via a 3D field map for the particle dynamics model. The dipole filter field is neglected in the simulations. The computational cycle performed at each time step is illustrated in figure 2.4.

2.1.4 Simulated plasma parameters

We have performed simulations for a range of coil currents I_{RF} and gas pressures p_{H_2} as indicated in table 2.1. We wish to describe the time evolution of the plasma starting from a low initial density and determine the minimum current required to achieve E-H transition. We first describe the simulation without $\boldsymbol{B_{cusp}}$ at $p_{H_2} = 3\ Pa$ and $I_{RF} = 130\ A$. Different conditions are later analyzed.

Time evolution of the plasma

Figure 2.5 shows the time variation of the average plasma density. Starting from the initial uniform density of $n_e = 5 \times 10^{14}\ m^{-3}$ (chosen from previous simulations to be below the transition limit) the electron density oscillates around the initial value during the first 3 μs, then rapidly increases by one order of magnitude in the following 2 μs.

In a cylindrical ICP the azimuthal component of the electric field accounts for the inductive power deposition, while the axial and radial components are associated with the capacitive power deposition [50]. To determine the E-H transition we integrate the Joule heating power

Table 2.1 – Simulation parameters.

Parameter	Value
Cell size, $\Delta r \times \Delta z$	2×2 mm
Time step, Δt	1 ps
Initial particle number	45000
Real particles per simulated one	2.5×10^6
Initial electron density	5.0×10^{14} m^{-3}
Initial proton density	5.0×10^{13} m^{-3}
Initial H_2^+ density	4.5×10^{14} m^{-3}
Frequency	2 MHz
Gas pressure, p_{H_2}	**1 to 10 Pa**
Antenna current, I_{RF}	**up to 300 A**

over the plasma chamber volume as a function of time and separate the capacitive component P_{cap} from the inductive P_{ind}:

$$P(t) = P_{cap}(t) + P_{ind}(t) = \int_V \boldsymbol{j} \cdot \boldsymbol{E}\, dV \tag{2.2}$$

$$P_{cap}(t) = \int_V \left(j_r E_r + j_z E_z\right)\, dV \tag{2.3}$$

$$P_{ind}(t) = \int_V j_\theta E_\theta\, dV \tag{2.4}$$

where $\boldsymbol{E} = \boldsymbol{E_{pl}} + \boldsymbol{E_{RF}}$. As shown in figure 2.5, initially the capacitive component drives the plasma discharge being one order of magnitude larger than the inductive one. As the density increases, the inductive component rises sharply, and above $10^{15}\ m^{-3}$ becomes the dominant heating.

The spatial distributions of the plasma density and electromagnetic fields show significant differences in the two regimes. During the first 3 μs, in the low density regime, the RF axial electric field $E_{z,RF}$ ($\approx$ 30 times larger than the azimuthal component $E_{\theta,RF}$) drives the plasma in the axial direction as shown in figure 2.6 and 2.7. While electrons are pulled in the direction opposite to $E_{z,RF}$, ions due to their larger inertia are only partially displaced in the direction of E_{RF} during one RF cycle. This results in a space charge imbalance in the axial direction that generates a $E_{z,pl}$ opposite to $E_{z,RF}$. As the density increases $E_{z,pl}$ becomes equal in magnitude and opposite in direction to $E_{z,RF}$, cancelling the effect of the RF axial field in the plasma region. Since the plasma current exists only in a region where E_z is weak, the capacitive power deposition drops. A similar argument applies to the radial component. However since this is only appreciable in the region close to the high voltage connection of the RF coil (figure 2.3), its contribution to the volume integral remains small. The azimuthal component on the other hand does not produce space charge imbalance given its symmetry and from this point on it is the only driving component to further heat the plasma, as shown in figure 2.8.

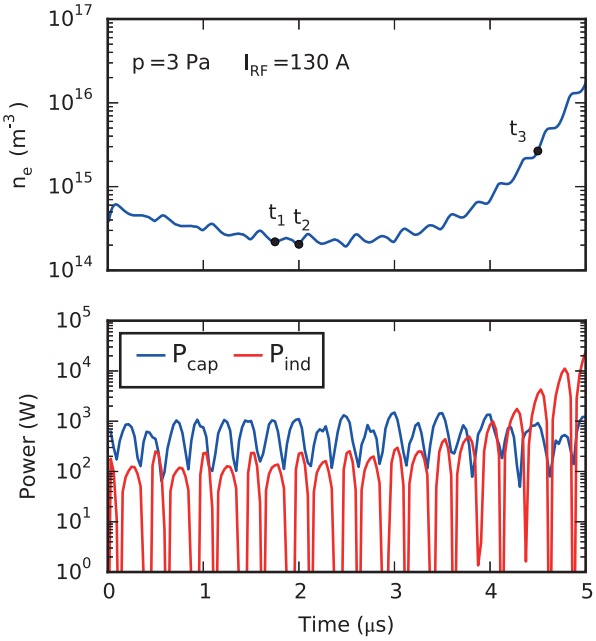

Figure 2.5 – Average electron density (top) and Joule heating power (bottom) as a function of time. t_x correspond to the phase of maximum E_{RF}. Particularly $t_1 = 1.75\ \mu s$ and $t_2 = 2.00\ \mu s$ correspond to the maximum E-field in opposite direction during the capacitively coupled regime, while t_3 is representative of the inductive coupled regime.

From a numerical point of view, it is important to remark that although the initial uniform distribution represents an artificial initial condition, the plasma is strongly redistributed during the first RF cycle under the effect of $E_{z,RF}$ in a trend similar to figure 2.6 and 2.7. Therefore the initial seeding distribution only influences the first RF cycle and does not perturb the remainder of the simulation. Furthermore, the plasma temperature is about 4-5 eV in the simulations. During the initial low-density phase as well as during the E-H transition the cell size remains comparable to the Debye length λ_{De}, avoiding numerical heating that would lead to a lack of conservation of energy. However this condition starts to be violated as the plasma density ramps to higher values in the last RF cycle. This is one of the reasons why the simulations are stopped at 5 μs and the high-density steady state cannot be simulated with the chosen cell size and Δt. The computation time form t=0 to t=5 μs is 4 days on a stand-alone PC (Intel Xeon @ 2.67 GHz, 16 GB RAM).

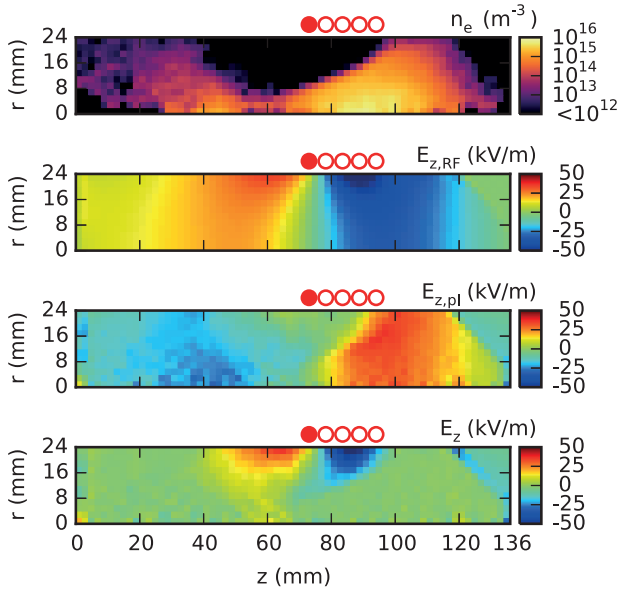

Figure 2.6 – Distribution of the plasma parameters in the plasma chamber. From top to bottom: electron density (n_e), RF axial E-field ($E_{z,RF}$), plasma axial E-field ($E_{z,pl}$), total axial E-field (E_z); evaluated at time t_1 in figure 2.5. This distribution is typical for a low density plasma driven by the capacitive field at a phase of maximum E-field. The plasma responds by generating $E_{z,pl}$ opposite to $E_{z,RF}$ resulting in a total E_z that is reduced in the plasma region.

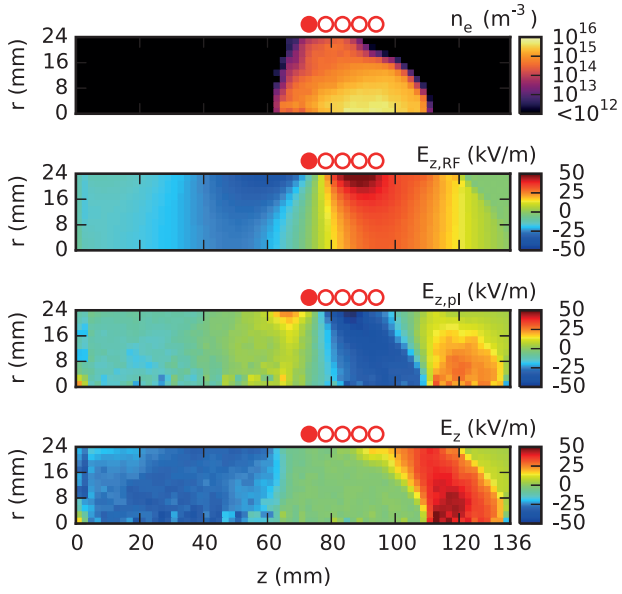

Figure 2.7 – Distribution of the plasma parameters in the plasma chamber. From top to bottom: electron density (n_e), RF axial E-field ($E_{z,RF}$), plasma axial E-field ($E_{z,pl}$), total axial E-field (E_z); evaluated at time t_2 in figure 2.5. This distribution is typical for a low density plasma driven by the capacitive field at the opposite phase of maximum E-field with respect to t_1.

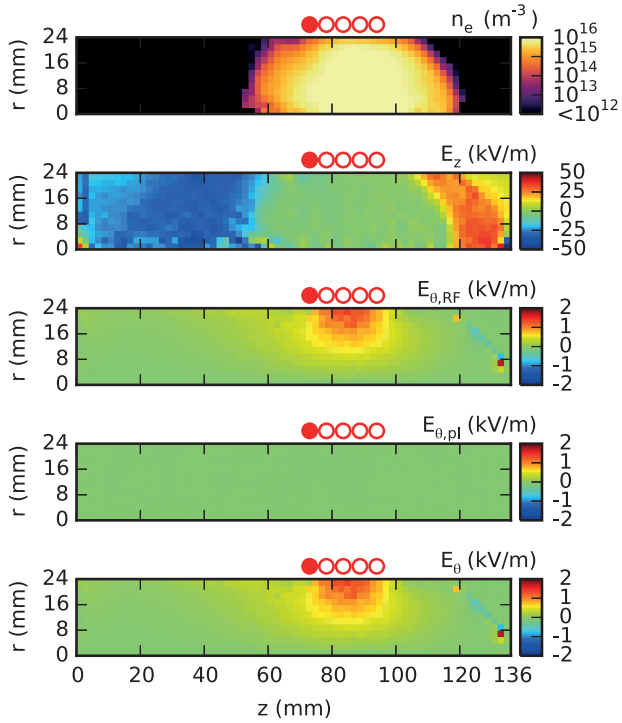

Figure 2.8 – Distribution of the plasma parameters in the plasma chamber. From top to bottom: electron density (n_e), total axial E-field (E_z), RF azimuthal E-field ($E_{\theta,RF}$), plasma azimuthal E-field ($E_{\theta,pl}$), total azimuthal E-field (E_θ); evaluated at time t_3 in figure 2.5. This distribution is representative of the density ramp-up in H-mode. While the axial field is shielded by the plasma, the azimuthal component fully penetrates into the plasma region and drives the discharge.

2.1.5 Antenna current required for E-H transition

The E-H transition current I_{EH} is defined as the value sufficient to achieve an inductive energy deposition in half RF cycle larger than the capacitive one. In other words, I_{EH} must satisfy:

$$\int_{t'}^{t'+\pi/\omega} P_{ind}(t)\,dt > \int_{t'}^{t'+\pi/\omega} P_{cap}(t)\,dt \tag{2.5}$$

where ω is the angular frequency. When this condition is met we always observe a large increase of the plasma density similar to the period around 4 us in figure 2.5. I_{EH} depends on the neutral gas pressure with a minimum around 2 Pa as shown in figure 2.9. For pressures lower than 1.2 Pa the transition does not take place and the plasma extinguishes, while for higher pressures the current increases in the whole range analysed. Comparison with experimental results will be described in section 2.1.6.

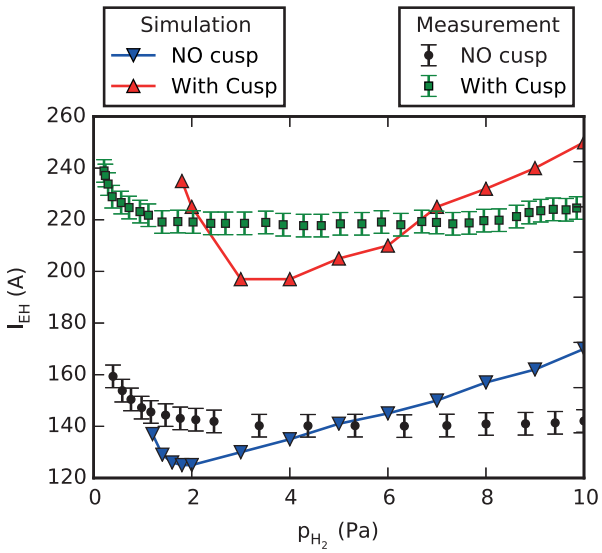

Figure 2.9 – E-H transition current I_{EH} as a function of pressure and magnetic configuration. The simulated value is the minimum current satisfying equation 2.5, while the measurement corresponds to the maximum current I_{RF} driven by the RF amplifier during the RF ramp-up.

Simulations with cusp field

When B_{cusp} is taken into account in the simulations, a redistribution of the electrons is observed as shown in figure 2.10. Electrons moving towards regions of increasing azimuthal magnetic field $B_{\theta,cusp}$ are either reflected back to the plasma or trapped in the magnetic field lines leading them to the wall.

In this configuration I_{EH} is ≈ 50% larger than the configuration without $\boldsymbol{B_{cusp}}$ (figure 2.9). This result is ascribed to the change in the spatial distribution of the inductive heating component resulting from the introduction of the $\boldsymbol{B_{cusp}}$. The inductive RF electric field $E_{\theta,RF}$ increases as a function of the radius and is therefore strongest at the radial wall (figure 2.8). Under the effect of $\boldsymbol{B_{cusp}}$ however, fewer electrons become available in this region to be accelerated. The plasma current remains therefore localized in the centre of the plasma chamber as shown in figure 2.11. In order to achieve the same inductive power deposition (equation 2.4) a larger $E_{\theta,RF}$ is therefore required, implying a larger I_{RF}.

2.1.6 Experimental investigation

This section describes the experimental investigation by optical emission photometry that we have performed on the Linac4 H^- ion source plasma chamber. We describe the experimental setup, results and comparison to simulations.

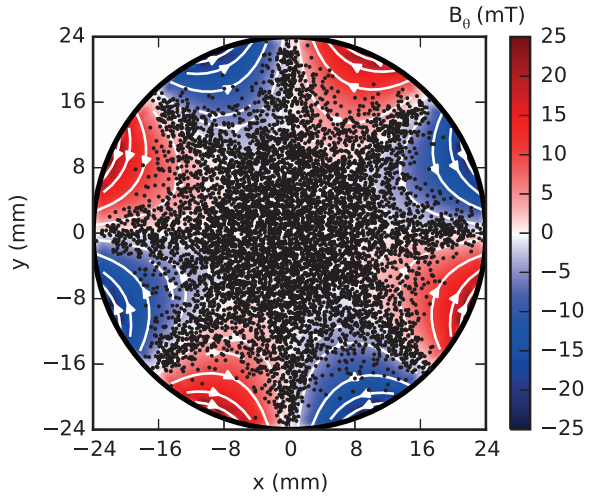

Figure 2.10 – Simulation with magnetic cusp field. The colorbar indicates the magnitude of the $B_{\theta,cusp}$ component. White streamlines indicate the direction of $\boldsymbol{B_{cusp}}$. Electrons are represented by the black dots. The 8 loss lines typical of the magnetic octupole in Halbach configuration are clearly visible.

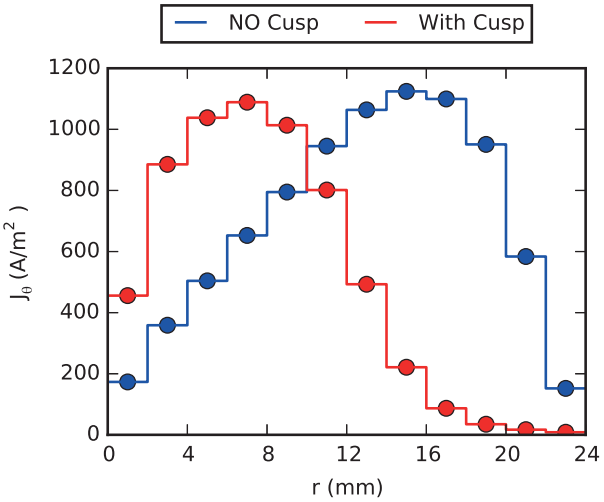

Figure 2.11 – Average plasma current j_θ in the coil region during the first half cycle satisfying equation 2.5. Simulation conditions are $p_{H_2} = 3\ Pa$ at the E-H transition current $I_{EH} = 130\ A$ for NO cusp and $I_{EH} = 200\ A$ with cusp.

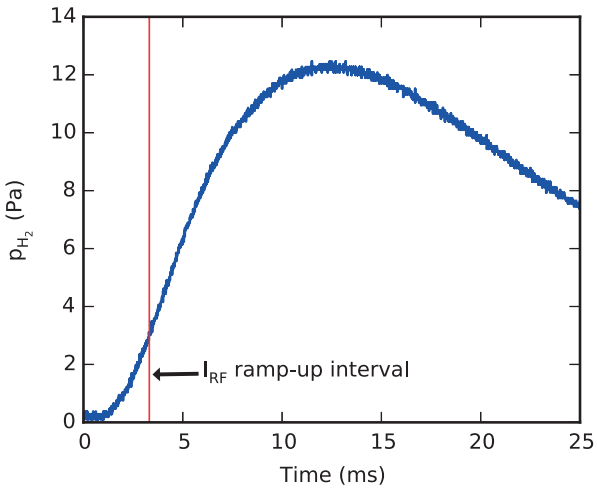

Figure 2.12 – Pressure curve for the pulsed gas injection. The piezo-valve controlling the gas flow is opened for 500 μs at t=0. The timing of the I_{RF} ramp-up is adjusted in the range 0-10 ms to select the pressure during the discharge.

Experimental setup

The experimental setup comprises 3 photomultipliers (PMT) Hamamatsu H10722-01 MOD5 to detect the plasma light emission. The light is collected by an optical fiber splitter connected to the view port on the plasma chamber axis shown in figure 2.1. Each fiber is directed to a PMT, whose output is read by a 12 bit oscilloscope (LeCroy HRO 64Zi). The PMT amplification gains are adjusted to cover different parts of the discharge as the light intensity typically spans 2-3 orders of magnitude. PMT_1 is set to the highest gain in order to capture the first light emitted by the plasma, PMT_2 is set such that when PMT_1 reaches 90% of its maximum output voltage (3 V), PMT_2 is at 10%. Similarly for PMT_2 with respect to PMT_3. This allows to reconstruct the full light signal by scaling each PMT signal by the ratio of outputs.

The RF amplifier increases I_{RF} at a rate of 10 $A/\mu s$ up to a limit of 300 A. All measurements are performed with the same input RF. A resonant network is employed to match the impedance to the 50 Ω amplifier. I_{RF} is measured by a current monitor Pearson 5046. The swift onset of the RF is synchronized to the gas injection via a piezo valve. Measurement of the pressure is taken from an off-line calibration of the pressure in the chamber as a function of the gas injection valve settings [26]. The pressure during the discharge is selected by adjusting the gas injection timing with respect to the RF ramp-up as shown in figure 2.12.

Experimental results

Figure 2.13 shows the the light emission during the I_{RF} ramp-up with $p_{H_2} = 3\ Pa$. As I_{RF} increases a faint light is first observed for a few RF cycles (10<t<12 μs), followed by a sharp

increase determining the plasma ignition. From this point the light emission enters a region characterized by asymmetric emissions with a higher peak followed by a smaller one every half RF cycle as shown in figure 2.14. As I_{RF} further increases the light emission becomes symmetric and raises by about one order of magnitude in 2 μs (figure 2.15) before reaching a maximum.

For a constant requested input power I_{RF} increases in $\approx$ 20 μs from zero to a maximum value before decreasing. The maximum I_{RF} driven by the RF amplifier depends on the gas pressure as well as the magnetic configuration. In the presence of the magnetic cusp field the maximum current observed is a factor 1.5 higher for every pressure, as shown in figure 2.9. In both configuration the maximum I_{RF} is smallest at a pressure of 2-3 Pa, it sharply increases for lower pressures while only slightly for higher ones.

The process leading to the plasma ignition has been previously reported in the literature [62], in which the authors showed that the initial faint emission is mainly originated from molecular excitation, while the first sharp peak is due to gas dissociation leading to atomic emission. The asymmetric emission is associated with the capacitive coupling driving the plasma. As shown in [18] the line integrated light emission, reconstructed from a collision-radiative model, indicates that the higher peak results from the E-field pushing the electrons towards the view port (figure 2.6) while the smaller peak to the plasma centred in the plasma chamber (figure 2.7). The main contribution to the light intensity is the distance of the photon emission to the view port and the emission roughly scales with the local electron density. As the discharge becomes dominated by the inductive component, the plasma remains centred in the coil region (figure 2.8) as $E_{z,RF}$ is shielded by the plasma. As electrons are accelerated and decelerated by $E_{\theta,RF}$ the emission increases and decreases respectively giving rise to symmetric peaks. In the simulations the electron density increases by about one order of magnitude in 2 μs which corresponds to the intensity variation observed in figure 2.15.

The maximum I_{RF} driven by the RF amplifier correlates to I_{EH} as previously reported in [50]. In the matched RF conditions (50 Ω load) the RF amplifier increases I_{RF} up to its limit of 300 A. If a plasma is formed an extra load is added to the system that scales with the plasma density [50, 13]. During the E-H transition the plasma density increases by two-three orders of magnitude, impling that the total load is no longer matched to the RF amplifier and I_{RF} decreases. In other words I_{RF} increases until the plasma has transited to the H-mode in which its impedance modifies the coupling efficiency and results in a drop of I_{RF}. The values of the maximum measured currents are reported in figure 2.9.

2.1.7 Discussion

The results highlight several important features characterizing the E-H transition dynamics. While the E-H transition is generally reported [48, 49, 50] as an average increase of the electron density and light emission, our results indicate that its detailed description must take into account the local properties of the plasma as these vary significantly in the chamber volume

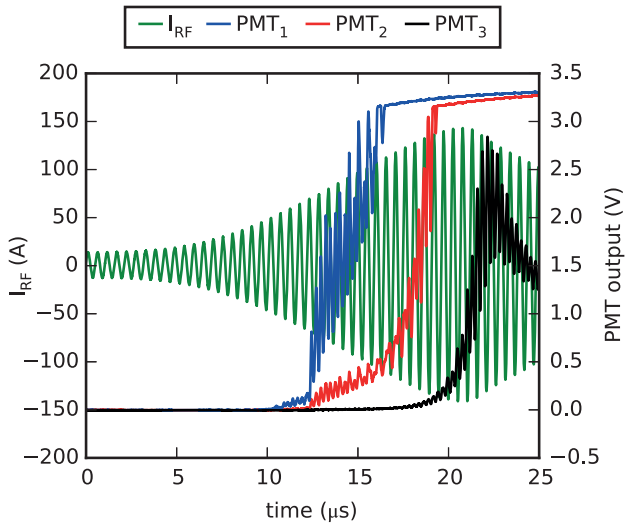

Figure 2.13 – Sample recording of the total light emitted by the plasma during the RF current ramp-up. The PMT voltages are adjusted to cover different parts of the discharge.

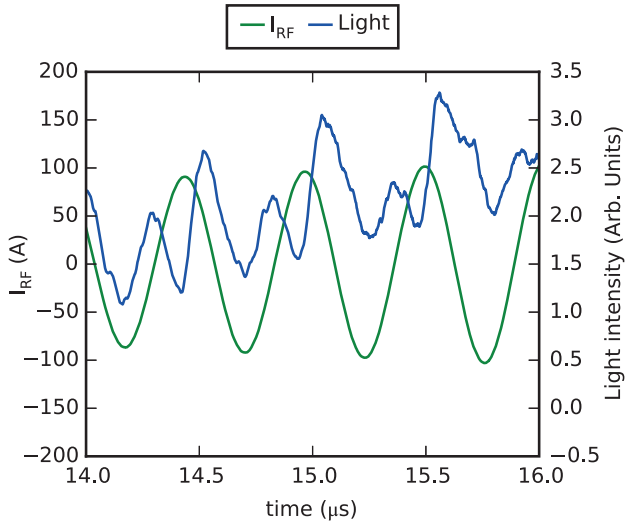

Figure 2.14 – Measured RF current and PMT light signal 2 μs following plasma ignition. The asymmetry of the peaks intensity is characteristic of the E-mode: the higher peak is representative of the electron distribution in figure 2.6, while the lower one of the distribution in figure 2.7.

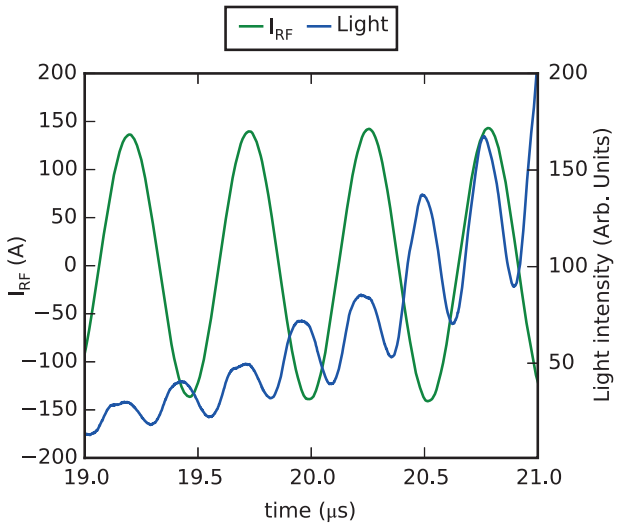

Figure 2.15 – Light emission during the density ramp-up characteristic of a discharge transited to the H-mode. The light intensity increases by one order of magnitude in 2 μs.

as a function of time and space.

The magnetic octupole field configuration also plays a crucial role in determining the amount of power required to achieve E-H transition. While $\boldsymbol{B_{cusp}}$ can limit the wall losses, an important decrease in the ionization rate results from the spatial power deposition that is significantly reduced close to the chamber wall. This suggests that optimal power transfer can be achieved by employing a magnetic configuration that, although strong at the wall, rapidly decreases towards the centre of the plasma chamber. This can be the case of magnetic cusp fields with higher number of poles. Alternatively, the external magnetic field can be installed to cover the plasma chamber except in the coil region. Since the azimuthal E-field is only effective in the coil region, the RF heating would not be influenced while preserving the plasma confinement in the rest of chamber.

The trend of the simulated I_{EH} as a function of pressure is similar to previous experimental results [48, 50] and of numerical simulations in purely inductive mode [23]. As shown in [48], $\boldsymbol{E_{RF}}$ is most effective at transferring its energy to the electrons at a pressure for which $\nu = \omega$ (ν is the collision frequency, proportional to p_{H_2}). For pressures below this value, the energy transfer is reduced as the electron mean free path becomes too large compared to the plasma chamber dimensions, while for higher pressures an increased I_{EH} is required to compensate for the reduction in electron average kinetic energy due to a higher collision frequency [23].

The comparison of I_{EH} between simulations and measurements shows two important features. First of all the range of I_{EH} obtained by simulations is comparable to the one measured experimentally, both with and without $\boldsymbol{B_{cusp}}$, result validating the numerical model employed and the treatment of $\boldsymbol{B_{cusp}}$. On the other hand the simulated I_{EH} shows a different trend as a function of the hydrogen pressure compared to the measured one (figure 2.9). The discrepancy

is similar in the case with and without $\boldsymbol{B_{cusp}}$. We believe that the discrepancy arises due to the different conditions in which simulations and measurements are performed. A major difference between simulations and experiments is that the first are performed for a constant I_{RF} starting from a given plasma distribution, while the latter are performed dynamically with a fast RF ramp-up. In the measurements we determine I_{EH} based on the change of the plasma impedance occurring due the E-H transition. The plasma impedance however scales non-linearly as a function of the electron density and temperature [50], both parameters depending on the pressure. Furthermore, one of the main assumptions in the simulations is the use of a background gas with fixed dissociation degree. Since gas dissociation depends on the electron energy, a larger dissociation degree can be expected at low pressures (higher energy) and vice-versa. This would modify the collision frequency and the ionization rate due to the different cross sections of molecular and atomic processes [34]. While the method allows a qualitative investigation and to clearly identify the effect of $\boldsymbol{B_{cusp}}$, a one-to-one comparison to the simulations is beyond the reach of the study and requires further investigations. Possible improvements could be achieved by modelling the RF circuit together with the plasma dynamics, or the use of an experimental setup similar to [48].

2.1.8 Conclusions and outlook

We have simulated the E-H transition by an EM-PIC-MCC code and compared the results to photometry measurements performed on the plasma chamber of the Linac4 H^- ion source. The results show that in the E-mode the plasma oscillates in the axial direction under the effect of the capacitive field. As the density increases the plasma shields the capacitive field and induction drives the heating process. We showed that the spatial plasma distribution plays a crucial role in the E-H transition dynamics.

The magnetic octupole modifies the electron distribution in the plasma chamber and reduces the power deposition in the region close to the wall. This resulted in a $\approx 50\%$ higher current to achieve the E-H transition.

The simulations agreed well with the experiments, reproducing qualitatively the trends during the E-H transition and quantitatively the effect of the magnetic cusp field. Quantitative analysis of the pressure variation requires the implementation of a neutral transport model as well as the inclusion of the RF circuit model in the simulations. This will be the object of further studies.

3 Simulation and experimental validation of a high density plasma

The Linac4 H^- source is required to sustain the hydrogen plasma discharge during 600 μs while the H^- beam is extracted. Following the RF power ramp-up the dominant plasma heating process is inductive (H-mode) and the plasma reaches a high density regime of 10^{19} m^{-3} [4]. In order to assess and optimize the plasma parameters for H^- production, a detailed investigation of this regime is performed.

The PIC-MCC code described in 2.1 proved very successful in simulating the plasma dynamics during the E-H transition. The natural step was therefore to extend its range of applicability to the simulation of high-density regimes. This was achieved in several stages: 1) the explicit integration scheme employed poses strict stability requirements in terms of the cell size ($\Delta x \lesssim \lambda_{De}$) and time step ($\Delta t < \Delta x/c$) making it inadequate to simulate the high density regime. A fully-implicit integration scheme was therefore developed, allowing much more relaxed numerical requirements; 2) in order to include H^- production and destruction processes, the Monte Carlo module was extended to include the relevant reaction cross-sections; 3) Coulomb and ion collisions were also added as they become important in this regime; 4) a neutral transport module was developed, within which the atomic and molecular (vibrationally resolved) populations are tracked kinetically.

The new code, named NINJA, has been described in a publication submitted to the Journal of Computational Physics (section 3.1). The simulation results were compared to Optical Emission Spectroscopy (OES) measurements providing, after analysis by collisional-radiative models, the plasma densities and temperatures in the Linac4 H^- source. A very satisfactory agreement was found. This work has been the object of two publications at the 5th Negative Ions Beams Sources (NIBS) conference 2016 and are reported in section 3.2 and 3.3. A subsequent parameter scan allowed to investigate the impact of design and operational parameters on the plasma dynamics, indicating possible improvements to the ion source design to maximize the production of H^- (chapter 4). The output from the NINJA code provides for the first time the boundary conditions required by H^- beam formation simulations [63, 40] indispensable for the engineering of the extraction system.

3.1 Publication 2: A fully-implicit Particle-In-Cell Monte Carlo Collision code for the simulation of inductively coupled plasmas

S Mattei[1,2], K Nishida[3], M Onai[3], J Lettry[1], M Q Tran[2], A Hatayama[3]

[1] CERN, CH-1211 Geneva 23, Switzerland
[2] Swiss Plasma Center, EPFL, Station 13, CH-1015 Lausanne, Switzerland
[3] Faculty of Science and Technology, Keio University, 3-14-1 Hiyoshi, Kohoku-ku, Yokohama 223-8522, Japan

Accepted for publication in Journal of Computational Physics, 2017

The paper was reformatted for uniformity and the references integrated into the thesis' bibliography, but otherwise the content remains unchanged.

3.1.1 Abstract

We present a fully-implicit electromagnetic Particle-In-Cell Monte Carlo collision code, called NINJA, written for the simulation of inductively coupled plasmas. NINJA employs a kinetic enslaved Jacobian-Free Newton Krylov method to solve self-consistently the interaction between the electromagnetic field generated by the radio-frequency coil and the plasma response. The simulated plasma includes a kinetic description of charged and neutral species as well as the collision processes between them. The algorithm allows simulations with cell sizes much larger than the Debye length and time steps in excess of the Courant-Friedrichs-Lewy condition whilst preserving the conservation of the total energy. The code is applied to the simulation of the plasma discharge of the Linac4 H^- ion source at CERN. Simulation results of plasma density, temperature and EEDF are discussed and compared with optical emission spectroscopy measurements. A systematic study of the energy conservation as a function of the numerical parameters is presented.

3.1.2 Introduction

In recent years there has been a strong interest in applications based on Inductively Coupled Plasmas (ICP): large-area integrated circuit manufacturing [46], medical devices [47], ion sources for accelerators [5] and fusion [64]. Key features of ICP driven discharges are the capability of obtaining high density plasmas (10^{17}-10^{18} m^{-3}) even at low gas pressures, and to operate without direct contact of the electrodes with the plasma. Modern applications set demanding specifications on the design and operation of ICP discharges, making it essential to develop detailed plasma models to gain insights into the underlying physics.

Theoretical and experimental studies have highlighted the importance of kinetic effects in ICPs [65, 66, 67] as well as local and non-local kinetics [68]. Modelling work of ICPs has mainly been performed using fluid [69, 70] and hybrid codes [71, 72], while only few papers

can be found on kinetic modelling that are particularly targeted at the low-density regime [14, 23, 9]. This is partially because kinetic simulations of high density, low temperature plasmas require very large computational resources and remained intractable for many years. One of the techniques to simulate plasmas from a kinetic point of view is the Particle-In-Cell (PIC) algorithm [59]. In its classical implementation, the time dependent governing equations are solved with an explicit leap-frog integration scheme. While this technique is simple and second order accurate, its limitations arise from the stringent time step Δt and cell size Δx required for its stability. In fact Δt must be kept sufficiently small to resolve the fastest wave propagations, typically electromagnetic radiation or plasma oscillations (Langmuir waves), in order to satisfy the Courant-Friedrichs-Lewy condition [59]. Δx on the other hand must resolve the finest electron scales happening at the Debye length λ_{De} to avoid a numerical plasma heating known in the literature as finite-grid instability [73]. This is a strong limitation for the simulation of ICPs, as λ_{De} can be in the order of tens of μm, while the typical plasma chamber size is several centimetres large, leading to a considerable number of cells to be simulated.

To overcome these limitations, alternative PIC implementations using implicit integration schemes have been considered since the 80's, starting with the pioneering work of Mason [74] and Denavit [75]. Implicit PICs require the concurrent solution of the non-linear coupling of the field equations with the particles' equations of motion and originally, due to the complexity of the problem, a number of semi-implicit codes were first developed (implicit moment [74, 75] and direct implicit [76]). Recently, thanks to advances in computing and numerical techniques, the fully-implicit solutions to the non-linear field-particles problem has been successfully addressed [77, 78]. These algorithms are shown to be unconditionally stable for any choice of Δt and replace the constraint on Δx to resolve λ_{De} by a much more relaxed condition that particles should not cross more that one cell in one time step. This is a significant improvement over explicit codes because the choices of Δt and Δx are no longer bound to strict stability requirements, but can be chosen to resolve only the scales of interest in the plasma under investigation.

Based on these considerations, we have developed a fully-implicit electromagnetic PIC code, called NINJA, for the kinetic simulation of ICPs. Our motivation originated from the investigation of the Linac4 H^- ion source at CERN [5], whose plasma is created in an ICP in cylindrical configuration. NINJA is a 2.5D PIC in cylindrical coordinates, where the electromagnetic (EM) fields are solved in 2D assuming azimuthal symmetry ($\partial/\partial\theta = 0$), while the particles' motion is solved in 3D3V. The model is supplemented with a Monte Carlo Collision (MCC) algorithm to describe the plasma chemistry as well as a neutral transport module including atomic and molecular (vibrationally resolved) particle tracking for hydrogen. This study represents, in our best knowledge, the first application of a fully-implicit PIC code for the simulation of bounded, collisional plasmas. We present a description of the algorithms, their implementation, a performance analysis and the application of the code to the investigation of the hydrogen discharge in the Linac4 H^- ion source.

3.1.3 Method

Governing equations

The goal of our simulations is to describe the plasma dynamics in an ICP. This requires modelling the interaction between the EM field generated by the Radio-Frequency (RF) coil and the corresponding plasma response, composed of the particles' motion and the collision processes between them. We are interested in describing the high density regime of an ICP, in which the coupling between the coil and the plasma is of the inductive type (H-mode) [45]. The electric field $\mathbf{E}$ and magnetic field $\mathbf{B}$ are given by Maxwell's equations in which the current density $\mathbf{J}$ is the sum of the plasma $\mathbf{J}_{pl}$ and the RF coil $\mathbf{J}_{RF}$ contributions:

$$\nabla \cdot \mathbf{E} = \frac{\rho}{\epsilon_0} \tag{3.1}$$

$$\nabla \cdot \mathbf{B} = 0 \tag{3.2}$$

$$\frac{\partial \mathbf{B}}{\partial t} = -\nabla \times \mathbf{E} \tag{3.3}$$

$$\frac{\partial \mathbf{E}}{\partial t} = \frac{1}{\epsilon_0 \mu_0} \nabla \times \mathbf{B} - \frac{1}{\epsilon_0} \mathbf{J} \qquad \mathbf{J} = \mathbf{J}_{RF} + \mathbf{J}_{pl} \tag{3.4}$$

with t representing time, ρ the charge density and ϵ_0, μ_0 the permittivity and permeability of free space respectively.

While $\mathbf{J}_{RF}$ is externally imposed, the plasma contribution $\mathbf{J}_{pl}$ results from the motion of the charged particles in the plasma. Kinetically this is represented by the first moment of the distribution function f_s (normalized to the plasma density n_s) of each plasma species s (e.g. electron, ion), resulting in:

$$\mathbf{J}_{pl} = \sum_s q_s \int_V \mathbf{v} f_s(\mathbf{x}, \mathbf{v}, t) \, dv \tag{3.5}$$

with $\mathbf{x}$ the position, $\mathbf{v}$ the velocity and q_s the electric charge of the species s. The particles' position $\mathbf{x}_p$ and velocity $\mathbf{v}_p$ define the distribution function f_s, and are mathematically described by Newton's equations of motion:

$$\frac{d\mathbf{x}_p}{dt} = \mathbf{v}_p \tag{3.6}$$

$$m_s \frac{d\mathbf{v}_p}{dt} = q_s(\mathbf{E}_p + \mathbf{v}_p \times \mathbf{B}_p) + \mathbf{F}_c \tag{3.7}$$

where m_s is the mass of the particle species s; $\mathbf{E}_p, \mathbf{B}_p$ represent the EM field acting on the particle p and $\mathbf{F}_c$ is the collisional force. Similarly, the motion of the neutral particles is described by equations (3.6,3.7) with $q_s = 0$. The self-consistent solution of the field equations

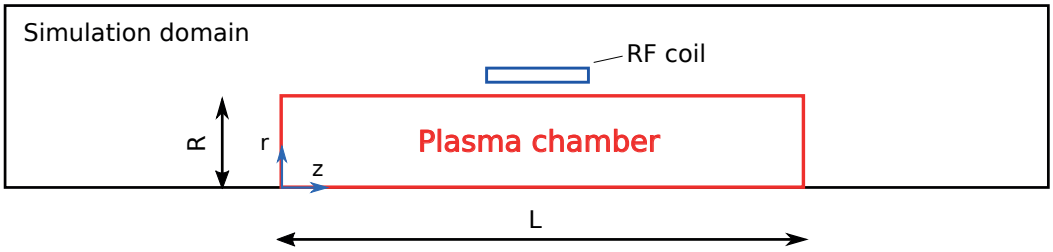

Figure 3.1 – Typical simulation domain: the plasma chamber is a cylinder of radius R and length L, while the calculation of the electromagnetic fields is performed on a larger domain. The RF coil is modelled as a perfect conductor with rectangular cross-section and given input current.

(3.1,3.2,3.3,3.4) and Newton's equations of motion (3.6,3.7), non-linearly coupled via equation (3.5) represent the full system of equations to be solved.

The governing equations are solved on a domain similar to the one represented in figure 3.1: the plasma chamber is a cylinder of radius R and length L while the calculation of the electromagnetic fields is performed on a larger domain in order to include the coil and to avoid large EM reflections at the boundary. The coil is modelled as a perfect conductor, with rectangular cross-sectional area and a given input $\mathbf{J}_{RF}$. Our model is developed in cylindrical coordinates. Given the azimuthal symmetry of this configuration we assume that the EM field is independent of the azimuthal coordinate ($\partial/\partial\theta = 0$), while the particle motion is fully 3D3V.

PIC scheme

We solve the governing equations using an implicit θ-scheme time integration and central differences on a Yee cell [56] for the spatial discretization (standard and not explicitly indicated). The time-discretized Maxwell's equations become:

$$\frac{\mathbf{B}^{n+1}-\mathbf{B}^{n}}{\Delta t} = -\nabla \times \mathbf{E}^{n+\theta} \tag{3.8}$$

$$\frac{\mathbf{E}^{n+1}-\mathbf{E}^{n}}{\Delta t} = \frac{1}{\epsilon_0 \mu_0}\nabla \times \mathbf{B}^{n+\theta} - \frac{1}{\epsilon_0}\mathbf{J}^{n+\frac{1}{2}} \tag{3.9}$$

where the superscript indicates time in units of Δt, and the fields on the right hand side are evaluated as a weighted average between the current time step n and the new one n+1:

$$X^{n+\theta} = \theta X^{n+1} + (1-\theta)X^{n} \tag{3.10}$$

The parameter θ affects the energy conservation and must be chosen $0.5 \leq \theta \leq 1$ else the scheme is divergent, while $\mathbf{J}$ is weighted at the half time step to avoid unphysical plasma

heating/cooling [79]. The two divergence equations (3.1,3.2) are not explicitly solved as equation (3.1) is automatically satisfied as long as charge conservation holds while equation (3.2) is always valid if satisfied initially [59].

The particles' equations of motion are first solved in the PIC scheme in their collision-less form, the inclusion of the collision operator is shown in section 3.1.3. Equations (3.6,3.7) are discretized as follows:

$$\frac{\mathbf{x}^{n+1}-\mathbf{x}^{n}}{\Delta t} = \mathbf{v}_p^{n+\frac{1}{2}} \tag{3.11}$$

$$\frac{\mathbf{v}^{n+1}-\mathbf{v}^{n}}{\Delta t} = \frac{q_s}{m_s}(\mathbf{E}_p^{n+\theta} + \mathbf{v}_p^{n+\frac{1}{2}} \times \mathbf{B}_p^{n+\theta}) \tag{3.12}$$

The fields $\mathbf{E}_p^{n+\theta}, \mathbf{B}_p^{n+\theta}$ acting on the particle p are evaluated at $\mathbf{x}_p^{n+\frac{1}{2}}$, interpolated from the 4 grid points surrounding the particle via a volume $(r^2 - z)$ weighting function W. The plasma current required by Maxwell's equations is loaded to the grid by the same weighting function and is given by:

$$\mathbf{J}_{pl}^{n+\frac{1}{2}} = \sum_{s}^{N_s} \sum_{p}^{N_{p(s)}} q_s \mathbf{v}_p^{n+\frac{1}{2}} W \tag{3.13}$$

where we employ Verboncoeur volume corrections [60] to avoid errors in the charge accumulations arising in curvilinear coordinate systems. In equation (3.13), N_s is the number of charged species in the plasma and $N_{p(s)}$ the number of simulated particles of a given species s. Every charged particle has the same specific weight w_c (ratio of real particles per simulated particle) independently of the species.

We employ absorbing boundary conditions for the charged particles on the plasma chamber, removing them from the computation once they reach the wall. For the EM fields, we employ absorbing boundary conditions at the limits of the simulation domain: Mur [57] at the axial ends and Bayliss-Turkell [58] at the radial one, both solved implicitly.

Solution of the non-linear system

At each time step we seek the solution of $6N_g$ field equations (3 components of $\mathbf{B}^{n+1}$ and 3 of $\mathbf{E}^{n+1}$ on each grid point), together with $6N_{p(s)}N_s$ equations of motion (3 spatial components of $\mathbf{x}_p^{n+1}$ and 3 velocity ones of $\mathbf{v}_p^{n+1}$ for each particle) coupled to each other via $\mathbf{J}$. For a typical simulation with $N_g \approx 10^4$ and $N_p \approx 10^6 - 10^7$ this would result in matrices whose size is impractical to solve. Following [80] we use a technique called kinetic enslavement which allows embedding the solution of the particles' equations of motion within function evaluations of the EM fields, keeping the matrices' size to the $6N_g$ EM field equations only.

We solve the system of equations (3.8,3.9,3.11,3.12,3.13) using the Jacobian-Free Newton Krylov (JFNK) method available in the NITSOL package [81]. NITSOL provides well-developed, simple to use algorithms for solving large-scale nonlinear systems, offering user flexibility (e.g. specific preconditioning) with easy adaptation to parallel environments. The field equations (3.8,3.9) are first rewritten in residual form:

$$\mathbf{F}(\mathbf{y}) = \mathbf{0} \tag{3.14}$$

with $\mathbf{y}$ a vector containing the unknowns $\mathbf{B}^{n+1}$, $\mathbf{E}^{n+1}$ and $\mathbf{F}(\mathbf{y})$ a non-linear operator. The non-linearity arises since $\mathbf{J}$ depends on $\mathbf{x},\mathbf{v}$ which are coupled to $\mathbf{E},\mathbf{B}$ via equations (3.11,3.12). Using a Newton method, we seek successive approximations to the system (3.14) based on information about the current guess $\tilde{\mathbf{y}}_k$ and its derivative:

$$\frac{\partial \mathbf{F}(\tilde{\mathbf{y}}_k)}{\partial \mathbf{y}} \delta \mathbf{y}_k = -\mathbf{F}(\tilde{\mathbf{y}}_k) \tag{3.15}$$

where the increment $\delta \mathbf{y}_k$ defines the new guess:

$$\tilde{\mathbf{y}}_{k+1} = \tilde{\mathbf{y}}_k + \delta \mathbf{y}_k \tag{3.16}$$

for each Newton iteration k. The resulting system of equations (3.15) is linear and can be efficiently solved by the Generalized Minimal RESidual (GMRES) method. The Jacobian matrix $\partial \mathbf{F}(\tilde{\mathbf{y}}_k)/\partial \mathbf{y}$ required in (3.15) at each Newton iteration is approximated by finite-differences. We use the standard NITSOL termination criteria in which iterations are stopped based on an absolute tolerance on the function evaluation $\|\mathbf{F}\| \leq$ ftol, or on a step tolerance: $\|\delta \mathbf{y}_k\| \leq$ stptol, as described in [81].

In the kinetic enslavement technique, the particles' equations of motion are embedded within function evaluations of the system (3.14). More precisely, at each GMRES iteration the latest guess of the EM fields $\tilde{\mathbf{B}}^{n+1}$ and $\tilde{\mathbf{E}}^{n+1}$ are available in the vector $\tilde{\mathbf{y}}$ and can be used to advance the particles via equations (3.11,3.12). With the new values of the particles' position and velocity we have all the information needed to form a new guess for $\tilde{\mathbf{J}}_{pl}$ via equation (3.13) and to advance to the next iteration. The operator $\mathbf{F}(\mathbf{y})$ besides containing the spatial discretization operators acting on $\mathbf{B}$ and $\mathbf{E}$ includes the particle mover used to update $\mathbf{x}_p$ and $\mathbf{v}_p$ as shown in algorithm 1 and section 3.1.3.

Algorithm 1: Function evaluation routine.

Input: latest guess $\tilde{\mathbf{y}}$, containing $\tilde{\mathbf{B}}^{n+1}$ and $\tilde{\mathbf{E}}^{n+1}$

Calculate $\tilde{\mathbf{B}}^{n+\theta}$ and $\tilde{\mathbf{E}}^{n+\theta}$

# For each particle find $\tilde{\mathbf{x}}_p^{n+\frac{1}{2}}$ and $\tilde{\mathbf{v}}_p^{n+\frac{1}{2}}$:
for $s = 1$ **to** N_s **do**
  for $p = 1$ **to** N_p **do**
    Solve equations of motion (3.11,3.12), see section 3.1.3
  end
end

Calculate $\tilde{\mathbf{J}}_{pl}^{n+\frac{1}{2}}$ via equation (3.13)
Evaluate residual via equation (3.14)

Particle mover

The particle mover contains the routines used to solve equations (3.11,3.12) leading to the update of $\mathbf{x}_p$ and $\mathbf{v}_p$ at each time step. Within the kinetic enslavement technique the particle mover can be chosen independently from the method used on the field solver, allowing greater freedom on the selection of the numerical techniques used.

To solve the particles' equations of motion (3.11,3.12) we seek to determine $\mathbf{x}_p^{n+1}$ and $\mathbf{v}_p^{n+1}$ based on the information of the grid values $\mathbf{E}^{n+\theta}$ and $\mathbf{B}^{n+\theta}$ stored in the vector $\tilde{\mathbf{y}}$ at each GMRES iteration. While the EM field on the grid is available, the force acting on the particle p depends on the position at half time step $\mathbf{x}_p^{n+1/2}$ which is yet unknown. Starting from the free streaming approximation we first estimate the position $\mathbf{x}_p^{n+1/2} = \mathbf{x}_p^n + \mathbf{v}_p^n \Delta t/2$ that we then subsequently refine by Picard iteration until convergence is reached.

The velocity at half time step $\mathbf{v}_p^{n+\frac{1}{2}}$ can be directly computed with an algebraic manipulation of equation (3.12) as shown in [82]. This leads to:

$$\mathbf{v}_p^* = \mathbf{v}_p^n + \alpha \mathbf{E}_p^{n+\theta} \qquad \text{with: } \alpha = \frac{q_s \Delta t}{2 m_s} \tag{3.17}$$

$$\mathbf{v}_p^{n+\frac{1}{2}} = \frac{\mathbf{v}_p^* + \alpha \left[\mathbf{v}_p^* \times \mathbf{B}_p^{n+\theta} + \alpha (\mathbf{v}_p^* \cdot \mathbf{B}_p^{n+\theta}) \mathbf{B}_p^{n+\theta} \right]}{1 + (\alpha \mathbf{B}_p^{n+\theta})^2} \tag{3.18}$$

With $\mathbf{v}_p^{n+\frac{1}{2}}$ available, the position $\mathbf{x}_p^{n+1}$ and velocity $\mathbf{v}_p^{n+1}$ at the new time step are computed as:

$$\mathbf{x}_p^{n+1} = \mathbf{x}_p^n + \Delta t \mathbf{v}_p^{n+\frac{1}{2}} \tag{3.19}$$

$$\mathbf{v}_p^{n+1} = 2\mathbf{v}_p^{n+\frac{1}{2}} - \mathbf{v}_p^n \tag{3.20}$$

In cylindrical coordinates one should include the extra inertial forces arising from the curvilinear transformation. Following Boris [83] this can be avoided by employing a local Cartesian coordinate system for each particle. More precisely at each time step n we align a Cartesian frame to the particle position such that $x^n = r^n$, $y^n = 0$ and $z^n = z^n$, with the velocity components $v_x^n = v_r^n$, $v_y^n = v_\theta^n$ and $v_z^n = v_z^n$. The particle advance is then performed in the local Cartesian frame where equations (3.18,3.19,3.20) are valid; the updated values are then retransformed to their respective cylindrical coordinates. During the step, the EM forces acting on the particle must also be rotated to align with the local coordinate frame. The sequence of operations is described in detail in [84], of which we follow the same steps.

Monte Carlo Collision method

Particle collision processes are taken into account via a Monte Carlo Collision (MCC) method, in which electron-neutral, electron-ion and ion-neutral collisions are handled via a null-collision method [61], whereas Coulomb collisions are treated with the binary collision method [85] following the work of [16]. The sampling of the null-collision is performed on each cell to take into account the local density of the target particles.

We implemented the model for a hydrogen discharge; the list of cross-sections and the respective references are listed in table 3.1,3.2. Following [61] we employ a constant time-step approach, in which collisions are calculated separately from the motion of particles and only need to be evaluated between time steps. This technique is valid as long as the collision time-step Δt_{coll} is much smaller than the mean free time τ, calculated for each species as the inverse of the maximum collision frequency ν_{max} in the energy range considered of 0-200 eV. Empirically we observe no difference in the results as long as $\Delta t_{coll} < \tau/100$. When a collision happens, a partner particle is selected in the same cell. The post-collision energies are taken from [86] with their respective velocities isotropically distributed [61].

Table 3.1 – Electron impact processes.

Partner	Reaction	Formula	Reference
H	Elastic	$e + H \longrightarrow e + H$	[87]
	Electr. exc.	$e + H \longrightarrow e + H(nl)$	[34]
	Ionization	$e + H \longrightarrow e + H^+ + e$	[34]
H_2	Elastic	$e + H_2 \longrightarrow e + H_2$	[88]
	Vibr. exc.	$e + H_2(v = 0) \longrightarrow e + H_2(v = 1,2)$	[34] $\star$
		$e + H_2(v \geq 1) \longrightarrow e + H_2(v \pm 1)$	[89] $\star$
		$H_2(B^1\Sigma_u^+) \longrightarrow H_2(v') + h\nu$	[35]
		$H_2(C^1\Pi_u) \longrightarrow H_2(v') + h\nu$	[35]
	Electr. exc.	$e + H_2(v) \longrightarrow e + H_2(B^1\Sigma_u^+)$	[34]
		$e + H_2(v) \longrightarrow e + H_2(C^1\Pi_u)$	[34]
		$e + H_2(v = 0) \longrightarrow$	
		$\longrightarrow e + H_2(B^{'}, B^{''}, D, D^{'}, EF)$	[34]
	Diss. via b^3	$e + H_2(v) \longrightarrow e + H_2(b^3\Sigma_u^+) \longrightarrow$	
		$\longrightarrow e + H + H$	[34]
	Nondiss. ioniz.	$e + H_2(v) \longrightarrow e + H_2^+ + e$	[34]
	Diss. ioniz.	$e + H_2(v) \longrightarrow e + H_2^+(^2\Sigma_u^+) + e \longrightarrow$	
		$\longrightarrow e + H^+ + H + e$	[34]
	Diss. attach.	$e + H_2(v) \longrightarrow H + H^-$	[34]
H_2^+	Diss. exc.	$e + H_2^+ \longrightarrow e + H^+ + H$	[34]
	Diss. recomb.	$e + H_2^+ \longrightarrow H + H$	[34]
	Diss. ioniz.	$e + H_2^+ \longrightarrow e + H^+ + H^+ + e$	[34]
H_3^+	Diss. exc.	$e + H_3^+ \longrightarrow e + H^+ + 2H$	[34]
	Diss. recomb.	$e + H_3^+ \longrightarrow 3H$	[34]
H^-	e-detach.	$e + H^- + \longrightarrow e + H + e$	[34]

$\star$ inverse processes evaluated by detailed balance

Table 3.2 – Ion impact processes.

H^+ impact processes

Partner	Reaction	Formula	Reference
H	Elastic	$H^+ + H \longrightarrow H^+ + H$	[90]
	Charge Exc.	$H^+ + H \longrightarrow H + H^+$	[34]
H_2	Elastic	$H^+ + H_2 \longrightarrow H^+ + H_2$	[90]
	Vibr. exc.	$H^+ + H_2(v=0) \longrightarrow H^+ + H_2(v=1\text{-}4)$	[34] ⋆
	Dissociation	$H^+ + H_2(v) \longrightarrow H^+ + H + H$	[34]

H_2^+ impact processes

Partner	Reaction	Formula	Reference
H_2	Charge exc.	$H_2^+ + H_2 \longrightarrow H_2 + H_2^+$	[34]
	CID*	$H_2^+ + H_2 \longrightarrow H^+ + H + H_2$	[34]
	H_3^+ ion form.	$H_2^+ + H_2 \longrightarrow H_3^+ + H$	[34]

H_3^+ impact processes

Partner	Reaction	Formula	Reference
H_2	Elastic	$H_3^+ + H_2 \longrightarrow H_3^+ + H_2$	[91]
	Proton transfer	$H_3^+ + H_2 \longrightarrow H_2 + H_3^+$	[34]
	CID* to proton	$H_3^+ + H_2 \longrightarrow H^+ + H_2 + H_2$	[34]
	CID* to H_2^+	$H_3^+ + H_2 \longrightarrow H_2^+ + H + H_2$	[34]

H^- impact processes

Partner	Reaction	Formula	Reference
H^+	Mutual neutr.	$H^- + H^+ \longrightarrow H + H$	[34]
H	Res. ch. exc.	$H^- + H \longrightarrow H + H^-$	[34]
	Assoc. detach.	$H^- + H \longrightarrow e + H_2$	[34]
	NA detach.	$H^- + H \longrightarrow e + H + H$	[34]
H_2	e-detach.	$H^- + H_2(v) \longrightarrow H + H_2(v') + e$	[34]

* Collision Induced Dissociation (CID)

Neutrals treatment

In a typical ICP discharge the ionization degree reaches values of a few %, implying that the largest populations are represented by neutrals. Their spatial distribution can be non-uniform in the plasma chamber, with depletion arising in the regions of highest ionization rate [92]. In molecular discharges (e.g. hydrogen) one must also take into account the long lived vibrational states, since those have significant effect on the electron and ion impact cross-sections [34].

We have implemented a neutral transport module for hydrogen, solving kinetically the equations of motion of the atomic H^0 and the 15 vibrational states of the molecular $H_2(v)$. The electronic excited states of H^0 and H_2 are not tracked in the present case given their short decay time. Electronic excitation processes are nevertheless considered in the reaction set and represent an energy sink for electrons and ions. To cope with the high density and large number of species, we employ a variable weight scheme using a rezoning technique [93]. More precisely, each neutral particle has associated its own specific weight w_n (ratio of real particles per simulated one). The scheme aims at keeping a constant number of neutral particles per species per cell $\bar{N_n}$ (typically 100), merging and splitting the simulated particles following the density variations due to transport or collisions. When the number of particles in a cell $N_n > \bar{N_n}$, following algorithm C1 in [93], we select the two closest particles of the concerned species $p = 1,2$ in phase space and replace them with a single one $p = A$ with the weighted average position, velocity and the sum of their weights w: $w_A = w_1 + w_2$, $\mathbf{x}_A = (w_1\mathbf{x}_1 + w_2\mathbf{x}_2)/w_A$, $\mathbf{v}_A = (w_1\mathbf{v}_1 + w_2\mathbf{v}_2)/w_A$. Similarly, if at any time the number of particles per cell $N_n < \bar{N_n}$ following algorithm S1 in [93] we split the particle with the highest weight $p = A$ in four particles $p = 1,2,3,4$ with the properties: $w_p = w_A/4$; $r_{1,2} = r_A \pm \Delta r/\bar{N_n}$, $r_{3,4} = r_A$; $\theta_{1,\ldots,4} = \theta_A$; $z_{3,4} = z_A \pm \Delta z/\bar{N_n}$, $z_{1,2} = z_A$. With this technique the maximum number of neutral particles to be simulated is $16 N_g \bar{N_n}$ (with 16 is the number of neutral species).

For compatibility with the MCC scheme, the range of neutral weights is larger and a multiple of the charged particle weights, i.e. $w_n \geq w_c$. This because in the event of a collision, only a fraction of the neutral particle corresponding to w_c must be considered in evaluating the post-collisional velocities, while leaving the fraction $w_n - w_c$ unaffected on its trajectory. If $w_n < w_c$ the scheme would be inconsistent. In practice therefore the merging technique is applied only when there are at least $N_n = \bar{N_n}$ particles in a cell all with at least $w_n = w_c$. Splitting is also avoided for particles with $w_n \leq 4w_c$.

The equation of motion for the neutrals only includes a collisional force as no EM field acts on them (equation 3.7). This accounts for collisions with other particles or wall interactions. Since no change in velocity happens during a time step (section 3.1.3), the equation of motion for the neutrals can therefore be solved directly with:

$$\mathbf{x}_p^{n+1} = \mathbf{x}_p^n + \Delta t \mathbf{v}_p^n \tag{3.21}$$

At the wall we employ a simple reflection boundary condition for H_2, inverting the velocity components in the directions in which the particle interacts with the wall. For H^0 wall recombination into H_2 is taken into account by a user-defined recombination coefficient γ_w that defines the reflected species by random sampling.

3.1.4 Code implementation

In this section we describe details of the code implementation and additions to the model presented in order to improve its performance. Firstly, we find it convenient to express the operator $\mathbf{F}(\mathbf{y})$ in matrix form:

$$\mathbf{F}(\mathbf{y}) = \mathbf{A}\mathbf{y} - \mathbf{b} - \mathbf{J}_{pl}(\mathbf{y}) = \mathbf{0} \tag{3.22}$$

where the matrix $\mathbf{A}$ contains the discrete spatial operator acting on $\mathbf{B}^{n+1}$, $\mathbf{E}^{n+1}$; $\mathbf{b}$ is the known term from the time step n and $\mathbf{J}_{pl}(\mathbf{y})$ is the plasma current which is a function of $\mathbf{y}$. This formulation is advantageous as, upon formation of the plasma current at each GMRES iteration, it leads directly to a vectorized implementation. Furthermore the matrix $\mathbf{A}$ has by construction a very low density and can efficiently be stored in sparse format, while $\mathbf{b}$ is a constant term at each time step and can be precomputed outside JFNK. For all sparse matrix computations we employ the SPARSKIT library [94].

Secondly, while SI units are convenient to describe the governing equations, they are not well suited for numerical computation as the numbers to be treated vary by many orders of magnitude. This may lead to a badly conditioned problem as well as to floating point rounding errors. To avoid these issues, we apply a normalization for which $\epsilon_0 = \mu_0 = 1$ leading to a speed of light $c = 1$. Furthermore we normalize time to the time step, mass to the electron mass and temperature to 1 eV. All other units follow accordingly. The conversion to normalized units is performed internally in the code, leaving inputs and outputs in SI units for ease of interpretation. As an example of the benefit of this transformation, the condition number of the matrix $\mathbf{A}$ decreases from $k(\mathbf{A}) > 10^{14}$ in SI units to $k(\mathbf{A}) = \mathcal{O}(10)$ in normalized units for typical simulation parameters.

In terms of performance, code profiling for a typical simulation with $N_g = 10^4$ and $N_p = 10^6 - 10^7$ reveals that the majority of the computing time (> 90%) is spent in the particle mover. Within the kinetic enslavement technique, at each function evaluation (algorithm 1) the full set of particles needs to be moved to calculate the new guess of the plasma current. This indicates that improvements in the code performance can be achieved either by seeking techniques to reduce the number of iterations required to achieve convergence in JFNK at each time step, or by parallelizing the computation, i.e. distributing the particles over several processes.

Preconditioning

To improve the performance of the code, it is highly desirable to reduce the number of GMRES iterations for each Newton step, which can be achieved by preconditioning the linear system (equation 3.15). An efficient preconditioner should represent an approximation of the Jacobian matrix $\partial \mathbf{F}(\tilde{\mathbf{y}}_k)/\partial \mathbf{y}$. From equation (3.22) we observe that the Jacobian matrix contains two components: the matrix $\mathbf{A}$ and a term depending on the plasma current. While the first term is known and constant, the second depends on the particular solution at any given GMRES iteration and it is not straightforward to calculate.

We employ a simple preconditioner in which the contribution acting on the plasma current is neglected. This represents a crude approximation of the Jacobian, which is sufficient to cut the number of GMRES iterations as long as the time step is not too large (see section 3.1.5). More precisely, we perform an incomplete Lower-Upper (LU) factorization of the matrix $\mathbf{A}$ with the *ilut* routine from SPARSKIT, which is later supplied to the *lusol* routine of the same library for the preconditioning within the NITSOL solver.

Parallelization

Code parallelization is implemented with the MPI interface, in which we use a domain decomposition technique at the particle level, while the EM calculation is performed serially on the full simulation domain. During the simulation time, density variations may cause the load on each process to be unbalanced. Therefore the total number of particles on each process is constantly monitored and compared to the average value, calculated as the total number of particles divided by the number of processes. If the load unbalance is > 10%, the subdomains are resized to host an approximately equal number of particles, while maintaining the boundary between sub-domains to coincide with cell's boundaries, to facilitate the treatment of the neutrals that require a constant number of particles per cell.

3.1.5 Code application

We present an application of the NINJA code for the plasma simulation of the Linac4 H^- ion source at CERN [5], whose geometry is shown in figure 2.1. The plasma chamber has a radius of 24 mm and a length of 136 mm, surrounded by a 5 turn RF coil operated at 2 MHz. At one end of the plasma chamber a 45° molybdenum electrode is installed, which is taken into account in the model by a staircase grid. No external magnetic fields are taken into account in the present study. The simulation domain is taken 3 times larger than the plasma chamber to avoid large reflections at the end of the domain. The simulation parameters and the initial conditions are listed in table 3.3. The plasma is initially seeded uniformly in the plasma chamber in a neutral state, i.e. the ion density equals to the electron plus the negative ion density. Neutrals are also initially seeded uniformly in the plasma chamber with a user-defined dissociation degree.

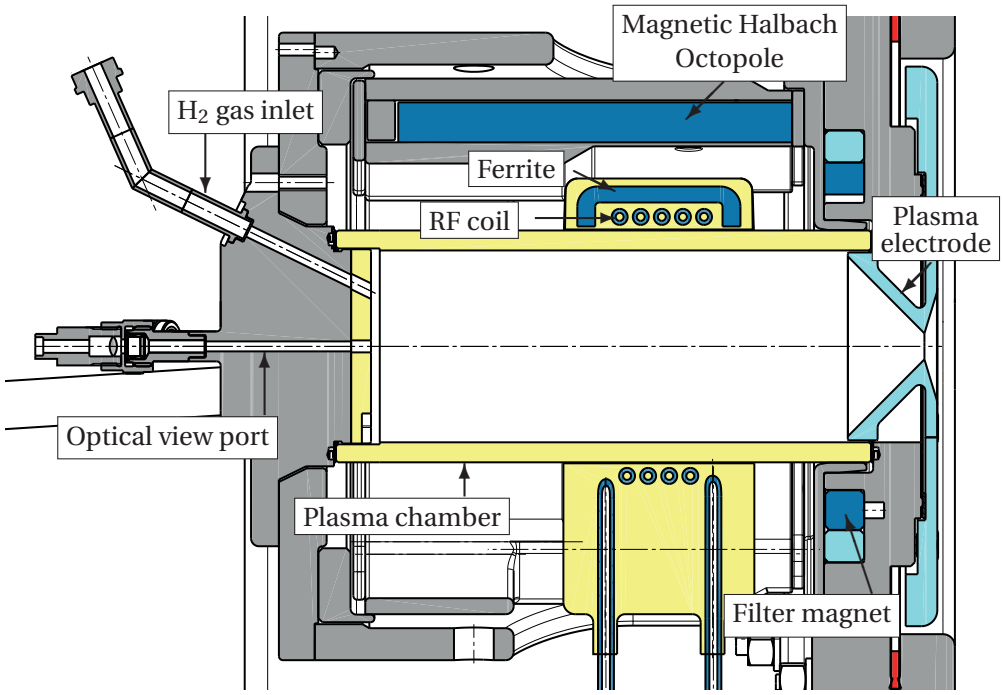

Figure 3.2 – Plasma generator of the Linac4 H^- ion source. The plasma chamber has a radius of 24 mm and a length of 136 mm. The 5 turn RF coil is surrounded by 6 ferrites and embedded in epoxy to avoid RF breakdown. The H_2 gas inlet and the optical view port used to perform optical emission spectroscopy measurements are indicated. The magnetic Halbach octupole is formed by alternating magnets with clockwise and counter-clockwise magnetization, while the filter field is a dipole magnet with vertical magnetization. The plasma electrode has an angle of 45° and is made of molybdenum.

The choice of the cell size and time step follows from an analysis of the spatio-temporal scales of interest in the plasma under investigation. More precisely, it is known that in an ICP the power transfer from the coil RF field to the electrons happens in a skin depth δ close to plasma chamber wall where the coil is located [95]. This represents a critical scale length for the simulation of ICPs and the cell size should therefore be sufficiently fine to resolve its dynamics. For the pressure and driving frequency employed an estimate of δ can be obtained as shown in [95]:

$$\delta = \frac{c\sqrt{2}}{\omega_{pe}}\sqrt{\frac{\nu}{\omega}} \tag{3.23}$$

where c is the speed of light, ω_{pe} the plasma frequency, ν the collision frequency and ω the angular frequency of the applied RF. For the case considered with $n_e \approx 10^{19}$ m^{-3} (taken from previous simulations and experimental results [25]), $\nu \approx 3.6 \cdot 10^7 p_{H_2} \approx 10^8$ Hz [96] we obtain

$\delta \approx 7$ mm. The cell size is chosen in the range $0.5 \leq \Delta x \leq 4$ mm.

For the time scales, the strictest condition is represented by the collision frequency ν implying that $\Delta t < 10^{-10}$ s to satisfy the Monte Carlo condition $\Delta t < \tau/100$ with $\tau = 1/\nu$. Such time step allows a fine resolution of the driving frequency and several of its harmonics.

We first present a simulation with $\Delta r \times \Delta z = 1 \times 1$ mm, $\Delta t = 2.5 \cdot 10^{-11}$ s and $\theta = 0.6$. The plasma distribution and the impact of the cell size on the simulation results is discussed in section 3.1.5, the Electron Energy Distribution Function (EEDF) is shown in section 3.1.5 and the energy conservation in section 3.1.5.

Parameters		**Initial conditions**	
Cell size	1×1 mm	Particle number	448'624
Time step	$2.5{\cdot}10^{-11}$ s	e^- density	$5{\cdot}10^{17}$ m^{-3}
Implicit parameter θ	0.6	e^- temp.	1 eV
Particle weight	$5{\cdot}10^{8}$	H^+:H_2^+:H_3^+	0.8:0.1:0.1
RF coil current	70 A	Ion temp.	0.1 eV
RF coil turns	5	Gas temp.	300 K
Gas pressure p_{H_2}	3 Pa (@300K)	Vib. temp.	3000 K
Wall recomb. γ_w	10^{-3}	Diss. Degree	0.3
ftol, stptol	10^{-4}, 10^{-5}		

Table 3.3 – Simulation parameters and initial conditions.

Plasma distribution

Starting from the initial uniform distribution we follow the plasma dynamics to reach steady state after 15 μs . Figure 3.3 shows the electron density and energy profile averaged in time during the last RF cycle (0.5 μs) of simulation. The electron density peaks at $n_e = 10^{19}$ m^{-3} on the central axis of the plasma chamber, in the axial region where the coil is located. The highest electron energy E_e is located in the coil region, with the hottest electrons in the vicinity of the radial wall where the RF electric field is strongest. At steady state the ion population is comprised of 85% H^+, 10% H_2^+ and 5% H_3^+, while H^- represent 1% of the negative charges. The simulation time is 2 weeks on a 12 core cluster (64 GB RAM with Intel(R) Xeon(R) CPU E5-2630L @ 2.00GHz).

Variation of the simulation results as a function of the cell size is better visualized on a line profile. Figure 3.4 shows the radial profile of n_e and E_e in the center of the coil, i.e. $z = 70$ mm. For a cell size ≤ 1 mm no significant difference is observed neither in the density nor the energy distribution. For larger cell sizes, the grid does not have the required resolution to capture the large gradients present in the skin depth and a different trend is observed, particularly in the region close to the wall $16 \leq r \leq 24$ mm.

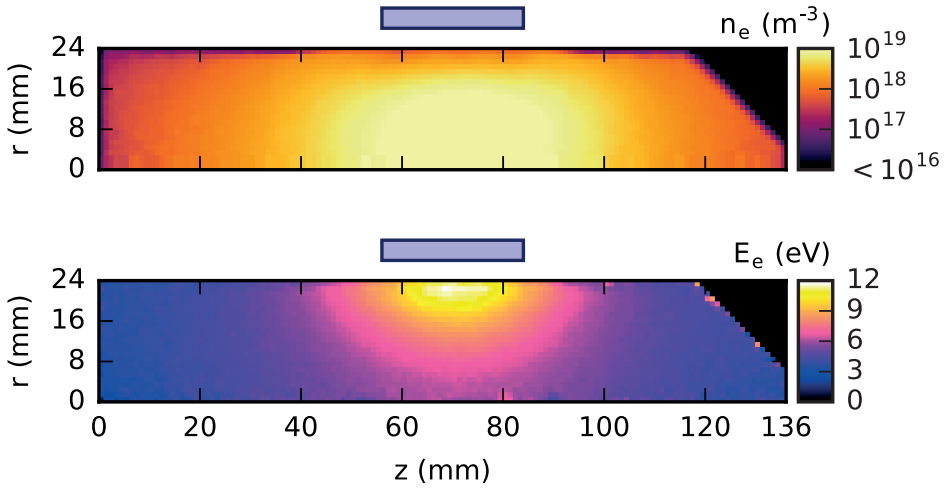

Figure 3.3 – Electron density (top) and electron energy (bottom) profiles, time-averaged during the last RF cycle of simulation with 1 mm cell size. The location of the RF coil is indicated by the blue rectangle.

Electron Energy Distribution Function

One of the most important characteristics of kinetic models is the self-consistent calculation of the EEDF in the plasma. From NINJA we can obtain the EEDF for any plasma region as a function of time. As an example we present the EEDF as a function of time during the last RF cycle in the region $0 \leq r \leq 4$ mm and $0 \leq z \leq 136$ mm. The region is selected to allow a direct comparison with Optical Emission Spectroscopy (OES) measurements performed on the axial view port of the plasma chamber (figure 3.2) [25].

Figure 3.5 shows the EEDF at two specific times corresponding to the RF current phase $\phi = 0$ and $\phi = \pi/2$. A significant deviation of the high energy tail ($E_e > 15\ eV$) of the EEDF is observed as a function of time. The time averaged-value, calculated from 16 EEDF snapshots during the last RF cycle, is well approximated by a Maxwellian distribution with T_e =4 eV.

Energy conservation

Monitoring of the energy conservation represents a crucial diagnostics to verify the implementation and the choice of the numerical parameters. If the total energy increases over time, it is an indication that numerical heating is taking place, which might lead to unphysical results. If the energy decreases, the method remains stable but one must be careful that important physics of interest is not suppressed. The conservation of electromagnetic energy is given by the Poynting theorem:

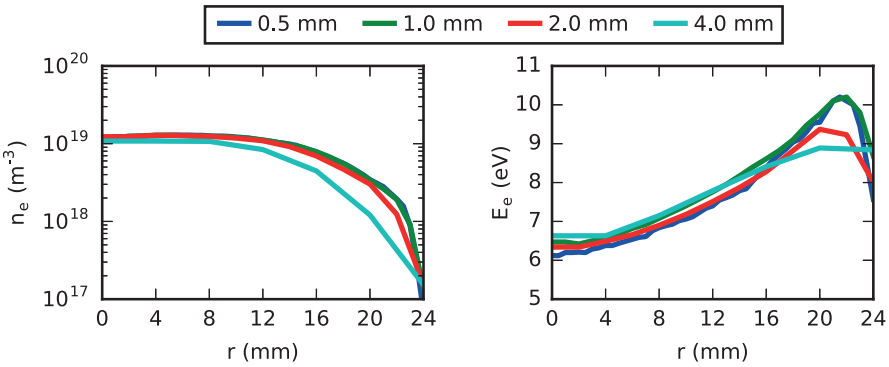

Figure 3.4 – Electron density n_e and energy E_e radial profile in the center of the coil, i.e. $z = 70$ mm for different cell sizes. All simulations are performed with $\Delta t = 2.5{\cdot}10^{-11}$ s and $\theta = 0.6$ and the profile represents the time averaged value in the last RF cycle of simulation.

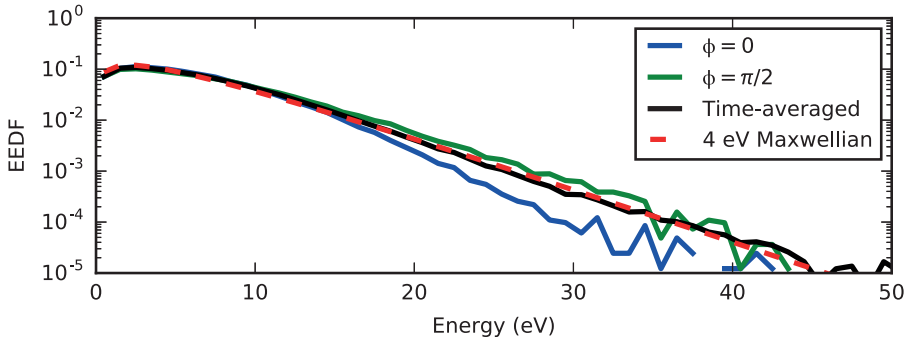

Figure 3.5 – Electron Energy Distribution Function (EEDF) for the RF current as a function of time during the last RF cycle of simulation in the region $0 \le r \le 4$ mm and $0 \le z \le 136$ mm. The time-averaged value fits a Maxwellian distribution of $T_e = 4$ eV.

$$\frac{\partial}{\partial t}(U_{EM} + U_k) = -P + W_{coll} - W_{wall} \tag{3.24}$$

$$\text{with: } U_{EM} = \int_V (\epsilon_0 \mathbf{E}^2 + \mathbf{B}^2/\mu_0) \tag{3.25}$$

$$U_k = \sum_s \sum_p^{N_{p,s}} m_s v_p^2/2 \tag{3.26}$$

$$P = \oint_{\partial V} (\mathbf{S} \cdot \hat{n})\, dA \tag{3.27}$$

where U_{EM} represents the energy stored in the fields $\mathbf{B}$ and $\mathbf{E}$, the kinetic energy U_k is given by the sum of the kinetic energy of all particles and P represents the flux through the surface, which is given by the integral of the Poynting vector $\mathbf{S} = \mathbf{E} \times \mathbf{B}/\epsilon_0$. The collisional power W_{coll} is the difference, per unit of time, between the source of EM energy given by production of

charged particles by gas ionization and the energy lost by charged particles in collisions (e.g. threshold energy lost by an electron in an atomic excitation process). The component W_{wall} represents the power deposited on the wall, i.e. the kinetic energy of the charged particles lost on the wall per unit of time.

Figure 3.6 shows the time-varying components of equation (3.24) for the simulation with $\Delta r \times \Delta z = 1 \times 1$ mm, $\Delta t = 2.5 \cdot 10^{-11}$ s and $\theta = 0.6$ during last RF cycle of simulation, representing the condition at steady state. The variation of all components show a 4 MHz oscillation, double the RF driving frequency. To evaluate the energy conservation we calculate the difference between the left-hand side and the right-hand side of equation (3.24), integrated in space over the plasma chamber volume, in time during the last RF cycle and normalized it to the RMS value of the left-hand side. The result for different simulation conditions is shown in figure 3.7, where one parameter is varied while keeping the others fixed based on the reference simulation of $\Delta r \times \Delta z = 1 \times 1$ mm, $\Delta t = 2.5 \cdot 10^{-11}$ s and $\theta = 0.6$.

The variation of the cell size indicates that, for a fixed Δt and θ, we have a tendency towards numerical heating by increasing the cell size. Increasing Δt or θ leads on the other hand to larger cooling rates, indicating that stronger damping is taking place. In other words, the choice of the numerical parameters is of paramount importance to control the energy conservation in the simulations, with smaller cell sizes requiring less numerical damping to conserve the energy. We remark that in the parameter range investigated, all simulations show an energy conservation within 2%.

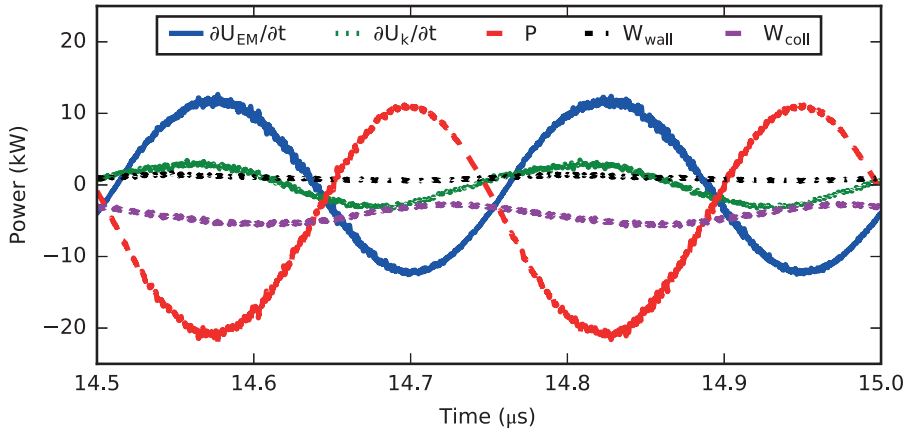

Figure 3.6 – Time variation of the energy components (see equation 3.24) for the simulation with $\Delta r \times \Delta z = 1 \times 1$ mm, $\Delta t = 2.5 \cdot 10^{-11}$ s and $\theta = 0.6$ during last RF cycle of simulation, representing the condition at steady state. All components show a 4 MHz oscillation corresponding to double the driving frequency of 2 MHz.

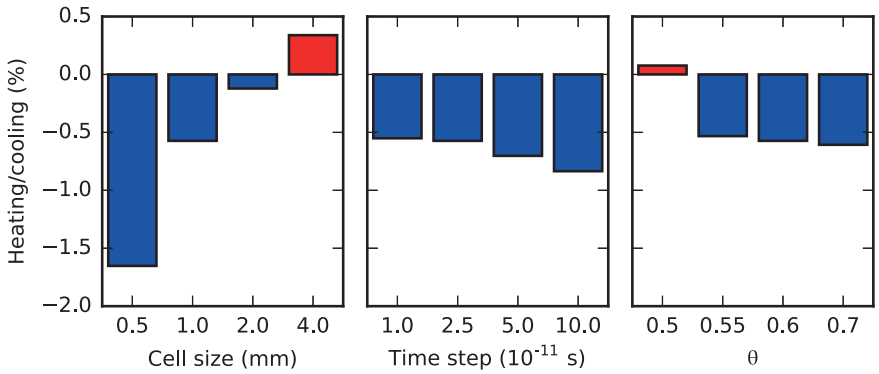

Figure 3.7 – Impact of the cell size, time step and implicit parameter θ on the energy conservation. Simulations are performed by varying only one parameter at the time, while keeping the others fixed based on the reference simulation of $\Delta r \times \Delta z = 1 \times 1$ mm, $\Delta t = 2.5 \cdot 10^{-11}$ s and $\theta = 0.6$. Energy conservation is evaluated during last RF cycle of simulation, representing the condition at steady state. Blue represents numerical cooling, while red numerical heating. In all simulations energy is conserved within 2%.

Performance

Code performance largely depends on the number of iterations required to reach convergence at each time step in JFNK. We performed an investigation of the number of function evaluations (Feval) required as a function of the time step and evaluate the effectiveness of the preconditioner. Figure 3.8 shows the number of Feval for a simulation with $\Delta r \times \Delta z = 1 \times 1$ mm and $\theta = 0.6$. The preconditioner cuts by a factor 3 to 8 the number of Feval required to reach convergence, leading to an equivalent improvement in the computational time.

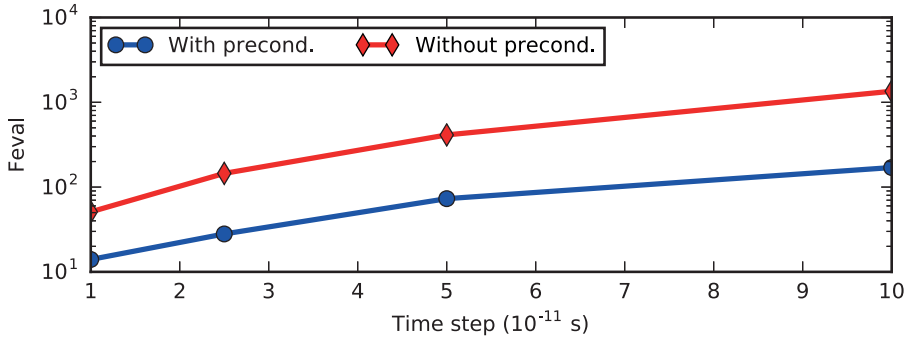

Figure 3.8 – Average number of function evaluations (Feval) required to reach convergence at each time step within JFNK. All simulations are performed with $\Delta r \times \Delta z = 1 \times 1$ mm and $\theta = 0.6$.

3.1.6 Discussion

A key feature of the model presented is the capability of simulating high density, low temperature plasmas with a cell size $\Delta x \gg \lambda_{De}$ while maintaining an accurate control of the energy conservation. This is of paramount importance to guarantee accuracy and stability for long integration time.

The numerical parameters controlling the energy conservation are the cell size Δx, the time step Δt and the implicit parameter θ. Based on our experience the recommended approach is to first choose Δx sufficiently fine to resolve the smallest spatial scale of interest; in the present case this is represented by the plasma skin depth δ required to capture the current channel in the vicinity of the RF coil. Other applications might require the detailed structure of the plasma sheath and therefore a much smaller cell size. Secondly, the time step should be chosen to resolve the spatial scales of interest including the driving frequency, the Monte Carlo condition on the collision frequency $\Delta t < \tau/100$ as well as resolving the electron gyrofrequency in case of magnetized plasmas. On the lower bound Δt is limited by preserving the energy conservation, together with the parameter θ. As Δt also strongly influences the performance, it is preferable to select Δt to be the most computationally efficient and adjust θ to conserve the energy. Should the range $0.5 \leq \theta \leq 1.0$ not be sufficient, Δt should be modified accordingly to preserve the energy conservation. While we have not pursued this option, in principle Δt and θ could be adapted dynamically during the simulation. These results are in agreement with previous analytical investigation of the energy conservation as a function of θ which has been performed in detail in [79] for an implicit moment method.

The range of plasma density and temperature simulated agrees with OES measurements performed on the plasma generator of the Linac4 H^- ion source [25] in similar conditions. Along the central optical view port, OES measurements report a line-integrated plasma density in the range $n_e = 10^{19}$ m^{-3} with an electron temperature $3.5 \leq T_e \leq 4$ eV. The results presented give an average value over the central 4 mm radius of $n_e = 5 \cdot 10^{18}$ m^{-3} with a time-averaged Maxwellian EEDF of $T_e = 4$ eV (section 3.1.5).

An important result of this study is the characterization of the time-varying EEDF, which is directly linked to the plasma light emission. Its impact should be further investigated, coupling the simulation results with a collision-radiative model taking into account the EEDF features (e.g. [97]). In the present work we have not discussed details of the neutral population (atomic and vibrational density/temperatures). This will be the object of a future publication. Furthermore, we plan to extend the model to address non-axisymmetric features, such as the external magnetic cusp and filter field.

In the specific case of the Linac4 H^- ion source, the present results represent crucial input for beam formation simulations [40, 98], that rely on the specifications of the plasma parameters in the extraction region (conical region at $z > 116$ mm). This is particularly important since spatially resolved measurements are difficult to achieve in this region due to space limitations. Coupling between these simulations, beam formation simulations and beam measurements

could indicate possible improvements to the plasma generator configuration as well as a better understanding of the beam extraction physics.

3.1.7 Conclusions and outlook

We have presented the algorithms and the implementation of a fully-implicit PIC-MCC code, NINJA, for the simulation of inductively coupled plasmas. The model solves self-consistently the coupling between the electromagnetic field generated by the RF coil and the plasma dynamics, composed of the kinetic description of charged and neutral particles together with the collision processes between them. The governing equations are solved with a kinetic enslaved Jacobian-Free Newton Krylov method, in which a preconditioner is supplied to enhance the performance.

A key feature of the method is the possibility of performing kinetic simulations of high density, low temperature plasmas with cell sizes $\gg \lambda_{De}$ and time step in excess of the Courant-Friedrichs-Lewy condition whilst preserving the conservation of the total energy. The application to the CERN Linac4 H^- ion source shows that with a cell size sufficient to resolve the plasma skin depth, an accurate representation of the plasma parameters is achieved. This is confirmed by agreement between simulations and optical emission spectroscopy measurements on the range of density and temperatures.

Simulation results show that the EEDF varies in time during one RF cycle, with a deviation of the high-energy tail from a Maxwellian distribution. Coupling with a collision-radiative model taking into account the simulated EEDF will allow to investigate its impact on the light emission and provide refined comparisons to optical emission spectroscopy measurements. The plasma parameters and neutral fluxes will be simulated for variable hydrogen densities, RF current and position of the RF coil to define the input for the optimization process of the Linac4 H^- ion source.

We have detailed the algorithms used for an ICP in cylindrical geometry with a solenoid RF coil, using hydrogen as the discharge gas. The model can easily be adapted to other gases provided the availability of collision cross-sections as well as to the simulations of ICPs in planar configuration.

3.2 Publication 3: Numerical Simulation of the RF Plasma Discharge in the Linac4 H^- Ion Source

S Mattei[1,2], K Nishida[3], M Onai[3], J Lettry[1], M Q Tran[2], A Hatayama[3]

[1] CERN, CH-1211 Geneva 23, Switzerland
[2] Swiss Plasma Center, EPFL, Station 13, CH-1015 Lausanne, Switzerland
[3] Faculty of Science and Technology, Keio University, 3-14-1 Hiyoshi, Kohoku-ku, Yokohama 223-8522, Japan

This article has been accepted for inclusion in the proceedings of the Fifth International Symposium on Negative Ions, Beams and Sources 2016, to be published by AIP Publishing.

The paper was reformatted for uniformity and the references integrated into the thesis' bibliography, but otherwise the content remains unchanged.

3.2.1 Abstract

This paper presents a Particle-In-Cell Monte Carlo Collision simulation of the Radio-Frequency (RF) plasma heating in the Linac4 H^- ion source at CERN. The model self-consistently takes into account the electromagnetic field generated by the RF coil, the external static magnetic fields and the resulting plasma response, including a kinetic description of the charged species (e^-, H^+, H_2^+, H_3^+, H^-), as well as the atomic and molecular (vibrationally resolved) populations. The simulation is performed for the nominal operational condition of 40 kW RF power and 3 Pa H_2 pressure. Results show that the plasma spatial distribution is non-uniform in the plasma chamber, with a density peak of $n_e = 5 \cdot 10^{19}\ m^{-3}$ in the RF coil region. In the filter field region the electron density drops by two orders of magnitude, with a substantial reduction of the electron energy as well. This results in a ratio $e/H^- \approx 1$ in the extraction region. The vibrational population is characterized by a two temperature distribution, with the high vibrational states showing a factor 2 higher termperature. A very good agreement is found between the simulation results and optical emission spectroscopy measurement performed on a dedicated test stand at CERN.

3.2.2 INTRODUCTION

Linac4 is the new H^- linear accelerator currently being commissioned at CERN as part of the upgrade of the LHC injector chain. Its cesiated ion source is required to deliver an H^- beam of 40-50 mA within a normalized RMS emittance of 0.25 mm mrad in pulses of 600 μs and a repetition rate up to 2 Hz [5]. H^- ions are created in a Radio-Frequency (RF) inductively coupled plasma operated at 2 MHz, where two modes of H^- production are known to take place: volume production by dissociative attachment of vibrationally excited molecules $H_2(v)$ [31], and surface conversion of protons H^+ and atoms H^0 impinging onto a cesiated surface

[32].

In previous studies we have investigated the effect of design and operational parameters on the plasma dynamics in the Linac4 H^- ion source: numerical simulations highlighted the importance of the magnetic field configuration and the gas pressure in achieving plasma ignition and transition to steady state [9, 23], the analytic model of the plasma impedance showed the impact of the plasma parameters on the RF circuit [13] and optical emission spectroscopy measurements allowed identification of the plasma parameters in different operational conditions [24]. On the other hand, a detailed description of the RF plasma heating and its effect on the plasma parameters responsible for H^- production has not yet been performed. This represents a crucial step to gain further insights into the plasma dynamics and to indicate possible improvements of the design and operational parameters to increase the source performance.

We have developed a Particle-In-Cell Monte Carlo Collision code to self-consistently simulate the coupling between the RF coil and the plasma. Our goal is to investigate the influence of the RF plasma heating on the $H_2(v)$ population and the H^+/H^0 fluxes onto the cesiated surface. The simulated plasma includes a kinetic description of the charged particles (e^-, H^+, H_2^+, H_3^+ and H^-) as well as the neutral populations of H^0 and $H_2(v)$. Output from these simulations represent crucial inputs for the modelling of the beam formation [40, 98] In this paper we present a detailed simulation of the plasma discharge at the nominal Linac4 operational conditions (40 kW RF power at 3 Pa H_2 pressure) including spatio-temporal variations of the population densities, neutral dissociation degree and vibrational temperature. The effect of the magnetic filter field is further described. Simulation results are compared to optical emission spectroscopy measurements performed on a dedicated test-stand at CERN.

3.2.3 GEOMETRY AND CODE DESCRIPTION

The aim of this work is to describe the plasma dynamics in the Linac4 H^- ion source, whose plasma generator is shown in figure 2.1. The hydrogen plasma is formed in a cylindrical Al_2O_3 plasma chamber with inner radius of 24 mm and length 136 mm. A 5 turn RF coil, surrounded by 6 ferrites, is installed around the plasma chamber and embedded in epoxy to avoid RF breakdown. The RF coil is operated at 2 MHz with an available peak power of 100 kW. The magnetic configuration includes an octupole cusp field in Halbach offset (formed by alternating magnets with clockwise and counter-clockwise magnetization) and a filter dipole field. A 45° Molybdenum electrode coated with Cesium is installed in the extraction region to allow surface conversion of impinging H^+/H^0 to H^-. Hydrogen is injected in pulsed mode by a piezo valve and the plasma is ignited for 600 μs with a repetition rate up to 2 Hz. Three optical view ports are available to capture the light emitted by the plasma, oriented on axis, 19° and 26° with respect to the cylinder central axis.

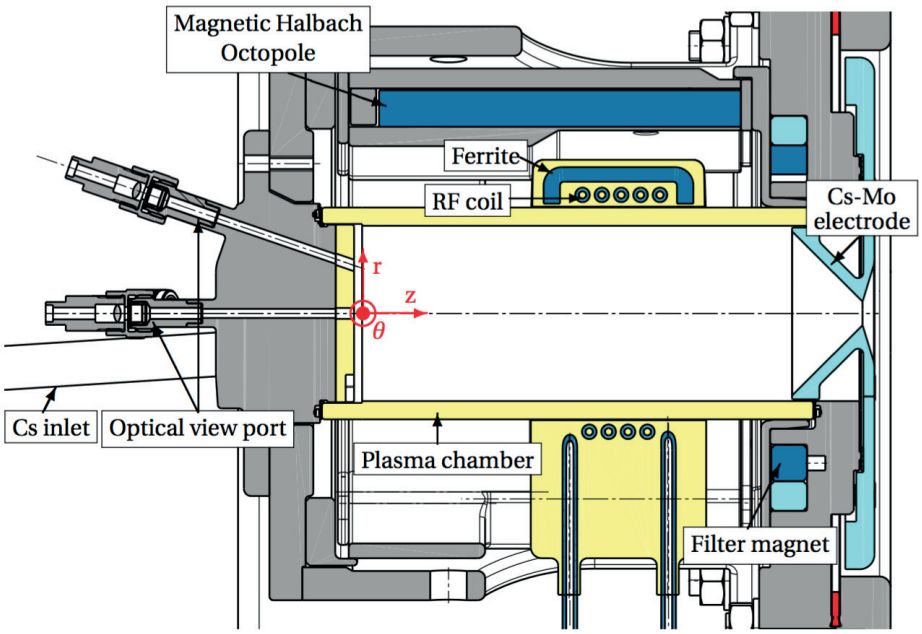

Figure 3.9 – Plasma generator of the Linac4 H^- ion source. The plasma chamber is made of Al_2O_3 and has an inner radius of 24 mm and a length of 136 mm. The 5 turn RF coil is surrounded by 6 ferrites and embedded in epoxy to avoid RF breakdown. 3 optical view ports (2 shown) are available to capture the light emitted by the plasma with a capture angle of 3° . The magnetic Halbach octupole is formed by alternating magnets with clockwise and counter-clockwise magnetization, while the filter field is a dipole magnet with vertical magnetization. The Molibdenum electrode is coated with a Cesium layer which is evaporated in a Cs oven and injected into the plasma chamber via the Cs inlet. The reference frame $\{r, \theta, z\}$ used in the simulations is indicated.

We simulate the plasma dynamics with our implicit electromagnetic Particle-In-Cell Monte Carlo Collision (PIC-MCC) code [7] supplemented with the routines to take into account the external static magnetic field (octupole + filter). The PIC-MCC code is 2.5 D in cylindrical coordinates meaning that the electromagnetic field is assumed to be 2D axisymmetric ($\partial/\partial\theta = 0$) while the particles' motion is 3D3V. The simulated plasma is composed of e^-, H^+, H_2^+, H_3^+ and H^-, as well as the atomic H^0 and the vibrationally resolved molecular $H_2(v)$ neutral populations. We employ absorbing boundary conditions for the charged particles reaching the plasma chamber wall, while reflection is employed for the neutrals. Surface chemistry, e.g. conversion $H^0 \rightarrow H^-$ is not included in the model. The Monte Carlo module includes over 200 electron-neutral, ion-neutral, electron-ion and Coulomb collision processes. The antenna is simulated by a perfect conductor of rectangular cross-section and given input current. The external static magnetic field is simulated with the 3D Tosca module of the OperaVectorfield software application and imported to the PIC-MCC via a fieldmap. The external magnetic field is interpolated at the particle level to maintain its 3D features.

3.2.4 RESULTS

We present a simulation of the plasma dynamics of the Linac4 H^- ion source in its nominal operational condition at 40 kW RF power and 3 Pa H_2 pressure. The numerical parameters employed as well as the initial conditions are listed in table 3.4. Specifically, the initial plasma density is seeded uniformly in the plasma chamber with an ion population chosen from previous simulations. The initial neutral temperature and the dissociation degree is taken from experimental results [24] measured in similar conditions. The RF current representative of a 40 kW RF power has been measured experimentally via a current transformer installed on the ion source and corresponds to I_{RF} = 200 A peak value. The time step is chosen to resolve the electron trajectories in the maximum magnetic field of 30 mT, while the cell size is selected to allow sufficient spatial resolution.

Table 3.4 – Simulation parameters and initial conditions.

Num. Parameter		Initial values	
Cell size	1×1 mm	Particle number	228'000
Time step	$2{\cdot}10^{-11}$ s	Gas temp	300 K
Particle weight	10^9	Diss degree	0.3
RF coil current	200 A	Vib temp.	6000 K
RF coil turns	5	e^- density	10^{18} m^{-3}
Gas pressure	3 Pa (@300K)	e^- temperature	1 eV
		Ion temperature	0.1 eV
		Ion distrib. H^+:H_2^+:H_3^+	20%:60%:20%

Plasma time evolution

Figure 3.10 shows the temporal variation of the average charged particle densities during the simulated time of 15 μs. Following the initial ramp up the electron density stabilizes at a level of $n_e = 6 \cdot 10^{18}\ m^{-3}$. The positive ion population significantly changes during the simulation and after 10 μs we have a distribution H^+:H_2^+:H_3^+ equal to 82%:12%:6%. H^- ions stabilize at $n_{H^-} = 4 \cdot 10^{16}\ m^{-3}$, ≈ 1% of the plasma density.

Concerning the neutrals we observe an increase of the atomic population by a factor 1.5 from $n_{H^0} = 2 \cdot 10^{20}\ m^{-3}$ to $n_{H^0} = 3 \cdot 10^{20}\ m^{-3}$, while the molecular density decreases (figure 3.11). It must be noted that the neutral population has not yet reached steady state after 15 μs of simulation. The vibrational temperature significantly changes during the simulated time. Starting from the initial vibrational temperature of 6000 K, we observe a clear increase of the high vibrational states, leading to a two-temperature distribution with T_{low} = 6500 K, and T_{high} = 13000 K where T_{low} is representative of the vibrational states v≤4 and and T_{high} of v≥5 (figure 3.12). The simulation time is 20 days on a 12 core cluster.

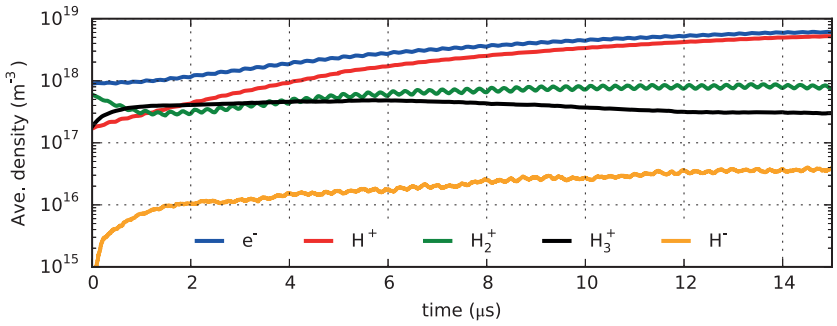

Figure 3.10 – Time evolution of the average charged particles' densities. After 15 μs of simulation the ion population is composed of 82% H^+, 12% H_2^+, 6% H_3^+, while negative ions represent $\approx$ 1% of the negative charges.

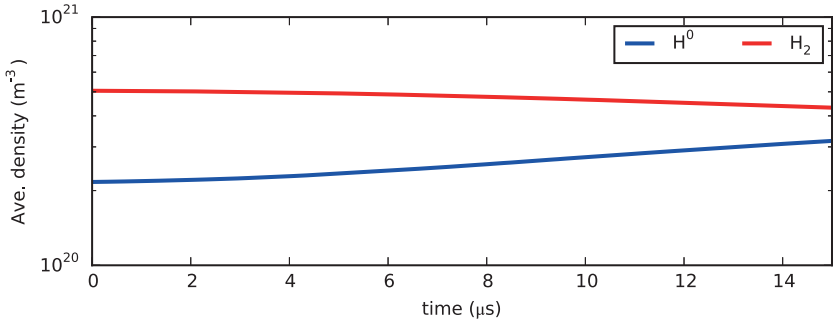

Figure 3.11 – Time evolution of the average neutral densities. The atomic population H^0 increases by a factor 1.5 during the simulation, while the moleucular one decreases. We observe that steady state is not reached during the simulation time.

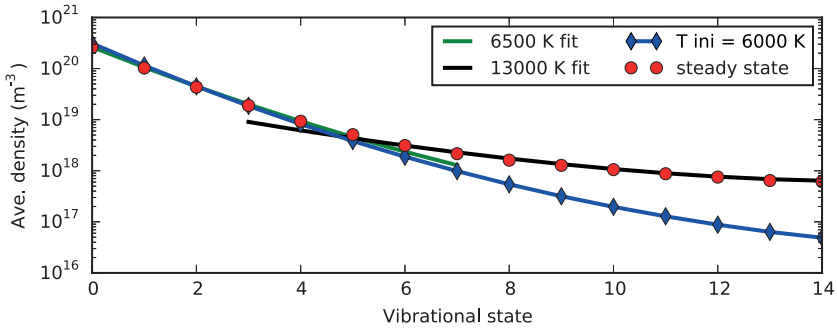

Figure 3.12 – Initial and final H_2(v) population. The initial vibrational temperature is chosen from experimental results. At steady state, the vibrational population is characterized by a two temperature distribution, T_{low} = 6500 K, and T_{high} = 13000 K where T_{low} is representative of the vibrational states v≤4 and and T_{high} of v≥5.

Plasma spatial distribution

The plasma spatial distributions are shown for the last μs of simulation, when the plasma is in quasi steady-state. Figure 3.13 and 3.14 show the time average value of the electron density and electron energy respectively, calculated from t=14 μs to t=15 μs. The electron density reaches its highest value in the coil region between 56 and 84 mm. In this region, the maximum density is found on the central axis, with a monotonically radial decrease towards the plasma chamber wall. Axially, as we move towards the extraction region the effect of the filter field increases, resulting in a clear reduction in both the electron density and energy. A plot of the distribution on the central axis better reveals the effect of the filter field on the plasma distribution. Figure 3.15 shows the electron and H^- density together with the electron energy as a function of the axial position. The maximum electron density is found in the RF coil region, where n_e peaks at $5 \cdot 10^{19}$ m^{-3}. As the filter field strength increases, the electron density decreases by 2 orders of magnitude, while the electron energy is reduced down to sub eV values. The H^- density is rather constant along the central axis, although it is important to remark that the ratio e^-/H^- significantly varies along the axis: in the plasma bulk the ratio is ≈ 100 while it drops to ≈ 1 in the extraction region. The H^0 flux onto the Cs-Mo electrode is found to be $6.45 \cdot 10^{22}$ $m^{-2}s^{-1}$. The value is calculated as the sum of all atoms impinging onto the electrode, divided by the integration time ($1\ \mu s$) and the electrode surface.

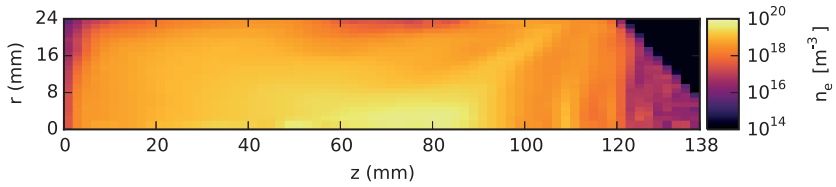

Figure 3.13 – Time averaged electron density profile during the last μs of simulation. The highest electron density is observed in the region 56 to 84 mm, where the RF coil is located. In the extraction region a clear reduction of the electron density is observed due to the presence of the filter field.

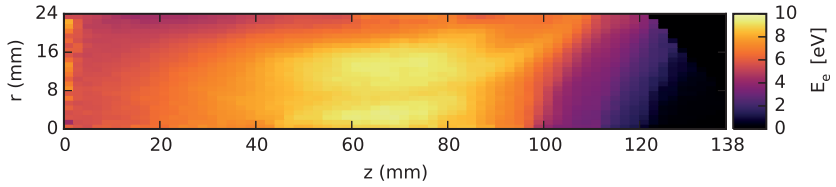

Figure 3.14 – Time averaged electron kinetic energy profile during the last μs of simulation. In the extraction region the electron energy is reduced to sub-eV levels due to the presence of the filter field.

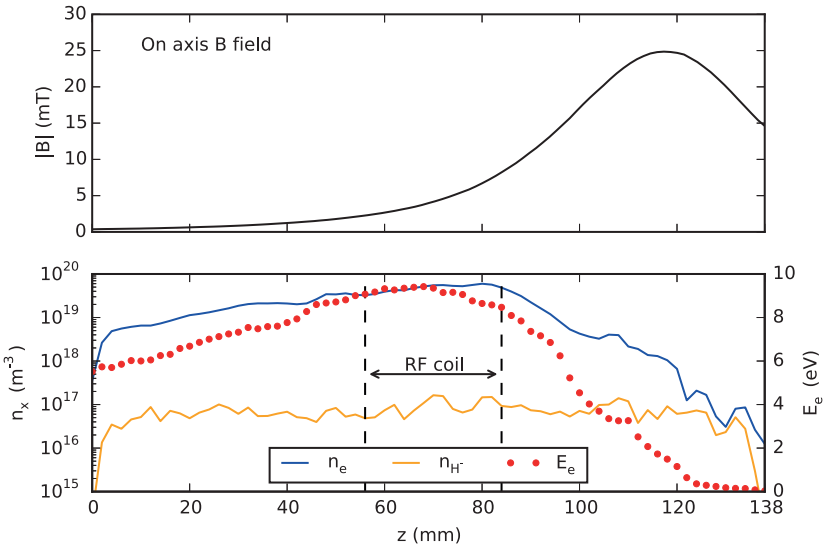

Figure 3.15 – Top: axial variation of the external magnetic field strength, evaluated on the plasma chamber central axis. Bottom: axial variation of the electron (n_e) and H^- (n_{H^-}) density together with the electron kinetic energy E_e. n_e and E_e show a clear reduction in the filter field region, while n_{H^-} remains rather constant along the axial position. The ratio e^-/H^- is ≈ 100 in the plasma bulk and reduces to ≈ 1 in the extraction region.

3.2.5 DISCUSSION

The simulations highlight several important features about the plasma parameters in the Linac4 H^- ion source. First of all, we remark strong spatial variation in the plasma chamber which depend on both the RF coil position, where a maximum n_e is found, and the magnetic filter field, which defines the drop in n_e in the extraction region. A similar trend is found for the electron kinetic energy. In the same conditions to the one simulated, optical emission spectroscopy performed on the on axis view port report an average electron density of $5{\cdot}10^{19}$ m^{-3} with a temperature of 4 eV, where a Maxwellian distribution is assumed (resulting in an average electron energy of 6 eV) [25]. As optical emission spectroscopy represent time-averaged, line-of-sight integrated measurement, a comparison to simulations can be performed by taking the average value along the central axis (figure 3.15). This results in a simulated $n_e = 2{\cdot}10^{19} m^{-3}$ and $E_e = 5.97$ eV, in good agreement with the measured parameters.

The simulation results represent crucial inputs for beam formation simulations [40, 98] which rely on the plasma parameters specified at the extraction region. Experimentally these parameters are difficult to obtain due to spatial constraints and therefore a reliable simulation of the plasma dynamics is of paramount importance to define realistic inputs. Besides the electron and ion populations, the H^0 flux onto the Cs-Mo electrode defines the emission rate of H^- from the surface, where typically a conversion rate $H^0 \rightarrow H^-$ of few % is observed [40]. In the present simulations the calculated flux would result in an H^- emission rate of ≈ 500 A/m^2

for a conversion rate of 5%. This value has been found to agree with beam measurements in previous studies [40]. It is important to notice that a future coupling to a beam formation code should be performed upstream of the extraction region, e.g. at z = 120 mm. This is to allow sufficient spatial resolution to resolve the plasma sheath close to the wall that the present simulations cannot provide.

Future studies will require longer simulation times to reach steady state for the neutral populations as well. Furthermore a systematic study of the surface chemistry (wall recombination, secondary emission, etc.) will be mandatory to investigate its role on the steady state plasma dissociation degree and the ion populations. In addition we intend to study parametric variations of H_2 pressure and RF power, performing a comparison to optical emission spectroscopy to validate the code in other regimes.

3.2.6 CONCLUSIONS

We have simulated for the first time the RF plasma heating in the Linac4 H^- ion source in the nominal operational conditions, taking into account the neutral populations as well as the external static magnetic fields. The simulated plasma parameters are in good agreement with optical emission spectroscopy measurements performed on a dedicated test stand at CERN.

The simulation tool developed allows us to gain insights into the plasma spatio-temporal behaviour in the plasma chamber, features that are otherwise inaccessible by experimental techniques. We believe that the coupling of the presented simulations together with beam formation studies is key to gain crucial information on the ion source physics and to define possible optimization to the source design and operational conditions to improve the source performance. Future work will include systematic studies on the RF power and H_2 pressure variations together with improvements in the surface treatment (e.g. wall recombination) with longer simulation times.

3.3 Publication 4: Influence of the cusp field on the plasma parameters of the Linac4 H^- ion source

S Briefi[1], S Mattei[2], J Lettry[2], U Fantz[1,3]

[1] AG Experimentelle Plasmaphysik, Universität Augsburg, 86135 Augsburg, Germany
[2] Linac4 Ion Source Team, CERN-ABP, 1211 Geneva 23, Switzerland
[3] Max-Planck-Institut für Plasmaphysik, Boltzmannstraße 2, 85748 Garching, Germany

This article has been accepted for inclusion in the proceedings of the Fifth International Symposium on Negative Ions, Beams and Sources 2016, to be published by AIP Publishing.

The paper was reformatted for uniformity and the references integrated into the thesis' bibliography, but otherwise the content remains unchanged.

3.3.1 Abstract

When the H^- ion source of CERN's Linac4 is operated in volume mode, a maximum of the extracted current is obtained at varying RF power. The power required for this maximum and its absolute value is strongly influenced by the cusp magnets installed at the source for electron confinement: without magnets, 15 – 20 mA are typically obtained at 20 kW whereas with magnets a factor of two more power is needed and 25 – 30 mA are achieved. In order to access the reasons behind the peaked performance with varying RF power and for determining the influence of the cusp field on the discharge, optical emission spectroscopy (OES) measurements of the atomic Balmer series and of the molecular Fulcher transition have been carried out. In all investigated cases, the gas temperature of the discharge has been virtually equal to the ambient temperature as the short discharge pulse length of 500 μs is not long enough for considerable heavy particle heating. When no cusp magnets are installed, the plasma parameters evaluated with the collisional radiative models Yacora H and Yacora H_2 show a minimum in the electron temperature of 3.25 eV and a maximum in the electron density of 4×10^{19} m^{-3} and also in the vibrational excitation of the hydrogen molecule at 20 kW. Assessing the relevant production and destruction processes demonstrates that the H^- yield is maximal at this point thereby explaining the optimum ion source performance. When the cusp magnets are applied, the same general trends are observed but the required RF power is a factor of two higher. The OES results indicate an optimum performance around 30 kW whereas the highest H^- current is actually achieved around 40 kW. Furthermore, a higher H^- yield is indicated without cusp magnets but a better ion source performance is observed with magnets. These differences can most likely be attributed to changing gradients in the plasma parameters which are not accessible by OES. Nevertheless, the obtained plasma parameters can be used as benchmark for RF coupling codes simulating the Linac4 ion source.

3.3.2 INTRODUCTION

Currently, an upgrade of the injector chain of the Large Hadron Collider (LHC) is realized at CERN which has the goal to improve both the particle beam brightness and the luminosity of the LHC. A crucial part of this upgrade is the construction of the Linac4 injector. It is foreseen as replacement for the ageing Linac2 which accelerates protons to 50 MeV before they are injected into the Proton Synchrotron Booster (PSB). In contrast, Linac4 is going to accelerate negative hydrogen ions up to 160 MeV and for the injection into the PSB the two electrons of the H^- ion are stripped with a thin foil [99]. The ion source of the Linac4 has to deliver an H^- current of 45 mA (for some special cases also up to 80 mA) in pulses of 500 μs at a repetition rate of 2 Hz. Negative hydrogen ions can be generated via two processes in general. The first method, the so-called volume process, relies on creating H^- in a plasma volume from vibrationally excited H_2 molecules. The second method, the so-called surface process, relies on the conversion of hydrogen atoms or ions on a surface with low work function [100]. In the latter case, caesium is evaporated into the ion source for establishing a low work function surface. Applying the surface process yields a higher H^- current but due to the high reactivity of caesium the work function of the surface and therefore the source performance degrades with time as caesium is removed and compounds are formed with the background gas. Therefore, sources operated in volume mode have the advantage of a higher temporal stability of the H^- current and reduced maintenance requirements.

At the Linac4 ion source cusp magnets are applied in order to reduce the losses of electrons to the discharge vessel wall. In general, for increasing the RF power also the extracted H^- current is increased up to one specific power level. Above this level the current decreases again. It has been observed that the cusp field has a strong influence on the RF power required for the best source performance. With magnets, the highest current is achieved at 40 kW whereas without cusp the required RF power is reduced by a factor of 2 to 20 kW. In order to assess the reasons behind this behaviour, optical emission spectroscopy measurements (OES) of the molecular Fulcher-α transition and of the atomic Balmer series have been carried out at the Linac4 test stand. During these investigations the source has been operated in volume mode i. e. without adding caesium. The emissivities obtained from OES have been evaluated with the collisional radiative (CR) models Yacora H [101] and Yacora H_2 [102, 103] yielding discharge parameters like the electron density and temperature. This allows for the investigation of the influence of the changing plasma parameters on the relevant production and destruction processes taking place in the discharge volume and therefore on the H^- yield. Unfortunately, it has not been possible to extract a beam during the measurements due to hardware problems of the high voltage system, therefore a direct comparison between the determined plasma parameters and the beam properties could not be carried out. Typically, the maximum beam current with installed cusp magnets is around 25 – 30 mA. Without magnets a reduced performance is obtained, only 15 – 20 mA are usually extracted.

3.3.3 THE LINAC4 H⁻ ION SOURCE

Only a short description of the Linac4 ion source setup is given here, a more detailed one also including the extraction and beam formation system can be found in [104]. The plasma is generated via inductive RF coupling with a helical coil of four windings (see Figure 3.16 for a sketch of the plasma chamber). The RF amplifier operates at a frequency of 2 MHz with a maximum RF power P_{set} of 100 kW. The discharge pulse length is 500 μs with a repetition rate of 2 Hz. For the RF power values in this paper, the power delivered to the ion source P_{del} is always given, i.e. the power reflected due to a mismatch between the ion source impedance and the 50 Ω output of the generator is subtracted from the power set at the generator ($P_{del} = P_{set} - P_{refl}$). In order to reduce the loss of electrons to the ceramic plasma chamber wall, a Halbach-offset octupole cusp field is created by NdFeB permanent magnets. Hydrogen gas is supplied to the ion source with a fast piezo valve opening only for a short time prior to the RF pulse. The gas diffuses through the plasma chamber and is pumped through the extraction aperture. As the gas dynamics happens on the scale of several ten milliseconds [105] (whereas the RF pulse only lasts for 500 μs) the gas pressure can be treated as approximately constant during the RF pulse.

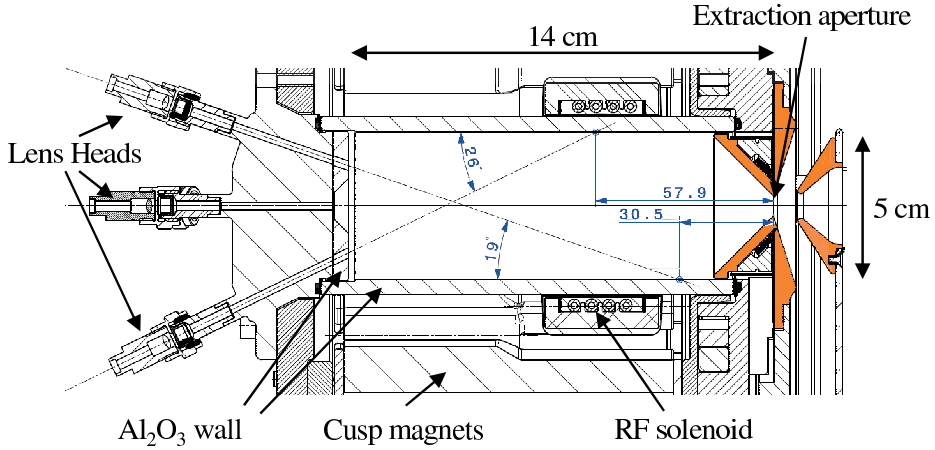

Figure 3.16 – Sketch of the Linac4 ion source plasma chamber.

For optical emission spectroscopy measurements the discharge chamber can be accessed via three lens heads collecting the light emitted by the discharge. The lens heads are separated from the discharge by a sapphire window and focus the plasma emission into optical fibres leading to a spectrometer. The different lines-of-sight determined by the lens heads are tilted with respect to the central axis of the cylindrical discharge vessel: 0° which means on-axis, 19° and 26°. For the measurements presented in this paper only the on-axis view port has been used. The utilized high-resolution spectrometer (1 m focal length, grating 2400 grooves per mm) is equipped with an ICCD camera and has a Lorentzian apparatus profile with a full width at half maximum of 8 pm around 600 nm. For acquiring spectroscopic data, only the last 400 μs of the plasma pulse are considered to avoid recording the transient ignition phase. The intensity calibration of the system has been performed via an Ulbricht sphere serving as

secondary radiation standard.

3.3.4 EVALUATING PLASMA PARAMETERS FROM OES

As already stated, the Balmer series of atomic hydrogen and the Fulcher transition of molecular hydrogen ($d\,^3\Pi_u \rightarrow a\,^3\Sigma_g^+$, located between 590 and 650 nm) were recorded by optical emission spectroscopy. For evaluating the obtained data the collisional radiative models Yacora H for atomic [101] and Yacora H_2 for molecular hydrogen [102, 103] are applied. These models calculate population densities via balancing all relevant population and depopulation processes for the particular states in the hydrogen atom or molecule, respectively. Processes including the reabsorption of photons have not been considered in order to facilitate the evaluation which means the plasma is treated as optically thin. As input parameters for the models the densities and temperatures of the neutral (H and H_2) and charged particles (electrons and H^+, H_2^+, H_3^+, H^-) are required. In order to determine plasma parameters from OES measurements, these input parameters are varied until both the absolute emissivities and the line intensity ratios of the measurements are matched thereby yielding the corresponding densities. However, for the investigated discharges, it turned out that the dominating population processes solely from atomic or molecular hydrogen and processes involving the hydrogen ions play only a very minor role. This eliminates the possibility of determining the densities of H^+, H_2^+, H_3^+ and H^- reliably. Besides the electron temperature and density only the densities of atomic and molecular hydrogen can therefore be obtained. It should be kept in mind that the intensities measured by OES represent line-of-sight averaged values, which means that also the determined plasma parameters have to be taken as line-of-sight averaged.

Another important input parameter for the CR models is the pressure of the hydrogen gas prior to the RF pulse as this determines the total number of particles available to the discharge. It is determined from the pressure in the plasma chamber via the ideal gas law. Due to the transient nature of the pulsed gas inlet, it is very difficult to give an exact number for the pressure within the plasma pulse and in-line pressure measurements are not possible due to the compact design of the ion source. Dedicated experiments concerning the gas particle propagation inside the vacuum setup of the ion source with respect to the gas valve settings have been carried out by replacing the discharge chamber with a T-shaped flange where a pressure gauge has been installed [105]. From these investigations, the gas pressure has been estimated to be at 3 Pa for the measurement campaigns presented in this paper.

Concerning the molecular Fulcher transition, the first twelve emission lines (rotational quantum numbers $N = 1,\ldots 12$) of the Q branch ($\Delta N = N' - N'' = 0$) arising from the first four diagonal vibrational transitions (vibrational quantum number $v' = v'' = 0,\ldots 3$) have been recorded. Figure 3.17 shows an exemplary emission spectrum of the corresponding wavelength range where the particular lines are labelled. From the measured emissivities the rotational population can be obtained. Typically, a non-Boltzmann rotational population is observed in hydrogen plasmas [106] which can be approximated by a two-temperature distri-

bution [107]. The cold part of this distribution which is described by the temperature $T_{rot,1}$ reflects the population via heavy particle collisions. The hot part of the rotational population described by $T_{rot,2}$ is weighted relatively to the cold part by the factor γ for fitting. This part of the population can in general arise from recombinative desorption of hydrogen atoms at the wall of the discharge vessel, from dissociative recombination of H_3^+ with electrons, or from direct electron impact excitation [106]. For the discharge conditions present in the Linac4 ion source, the most likely process leading to the hot rotational distribution is collisional excitation by electrons. The gas temperature of the discharge can be determined by projecting $T_{rot,1}$ from the excited $d\,^3\Pi_u$ state into the electronic ground state of the hydrogen molecule according to the rotational constants of the two states [108].

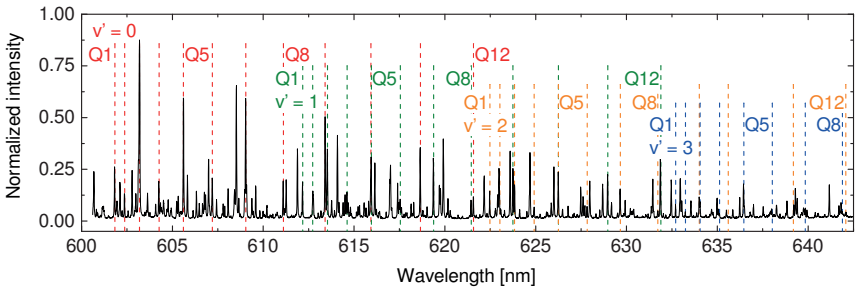

Figure 3.17 – Example spectrum of the molecular Fulcher radiation. The drop lines indicate the position of the Q lines for the first four diagonal vibrational transitions.

3.3.5 RESULTS

Rotational population of H_2 and gas temperature

For evaluating the rotational distribution of the $d\,^3\Pi_u, v' = 0$ state from the Fulcher emission, the measured emissivities of the rovibrational lines are divided by the statistical weight introduced due to the nuclear spin and by the Hönl London factors. When the logarithm of these values is plotted against the energy difference of the particular rotational levels, a Boltzmann distribution would in general lead to a linear slope. The left part of Figure 3.18 shows the rotational distribution obtained at an RF power of 40 kW. The two-temperature fit yields a value of $T_{rot,1} = 152$ K resulting in a gas temperature of $T_{gas} = 304$ K being virtually equivalent to the ambient temperature. Due to the low value of the cold rotational temperature, only the first rotational level and to a lesser extent also the second one follows the cold population. Therefore, one could argue if the high population in the $N = 1$ level is a statistical outlier and the actual gas temperature is much higher (in fact this was done for evaluating the first OES measurements [109]), but this is not the case: in the right part of Figure 3.18 the rotational population of the $d\,^3\Pi_u, v' = 0$ state is shown operating the ion source exceptionally with deuterium. The non-Boltzmann character of the distribution is also clearly present for D_2 and similar to H_2 a value of $T_{rot,1} = 155$ K is obtained. Due to the higher mass of D_2 the energy

difference between the particular rotational levels is smaller. This leads to a higher number of levels following the cold distribution making it much more evident compared to hydrogen. The cold gas temperature can be explained by the short discharge duration of only 500 μs which prevents the heavy particles from heating up considerably. For all investigations, the gas temperature of the discharge has always been virtually equivalent to the ambient temperature and no influence of RF power or the cusp magnets could be determined.

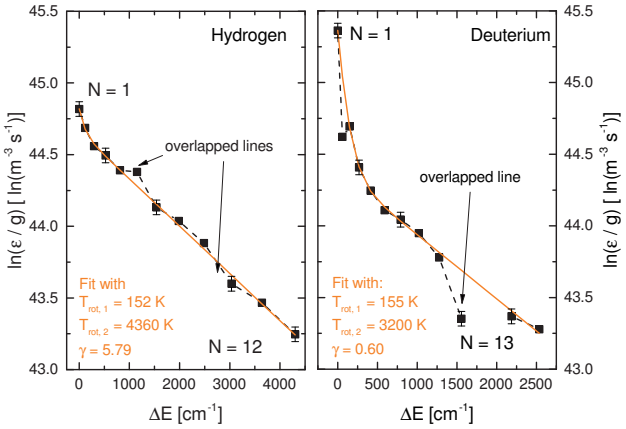

Figure 3.18 – Rotational distribution within the $d\,^3\Pi_u$, $v' = 0$ state evaluated from the Fulcher emission recorded for an RF power of 40 kW in deuterium and hydrogen. The corresponding two-temperature fits are also plotted.

RF power variation without cusp field

When no cusp magnets are installed at the ion source, its operational range with respect to the RF power is limited to 5 – 40 kW, otherwise either the discharge ignition or its stable operation is not possible. Figure 3.19 shows the emissivities measured for varying the RF power in this range (the RF power required for best performance is indicated by the grey hatched area around 20 kW). It can be seen that the atomic Balmer radiation steadily increases with increasing RF power whereas the molecular Fulcher radiation shows a minimum between 10 and 20 kW. The electron temperatures and densities obtained from evaluating the CR models are summarized in Figure 3.20. The value of T_e decreases from 3.75 to 3.25 eV when the power is increased from 5 to 15 kW. Above 15 kW, T_e increases again reaching values of 3.90 eV at 40 kW. The electron density shows a contrary behaviour, increasing from 1.6×10^{19} m^{-3} at 5 kW to a peak value of 4×10^{19} m^{-3} achieved between 15 and 25 kW. The density ratio of atomic to molecular hydrogen obtained from the OES measurements is shown in Figure 3.21. For increasing RF power, the density ratio increases steadily from 0.28 at 5 kW to a value of around 0.6 above 25 kW.

For such plasma parameters, the dominating destruction process for negative hydrogen ions is collisional detachment by electrons: $H^- + e_{fast} \rightarrow H + 2e$. Balancing this destruction process with the formation process $H_2(v) + e_{slow} \rightarrow H^- + H$ shows that the electron density does not

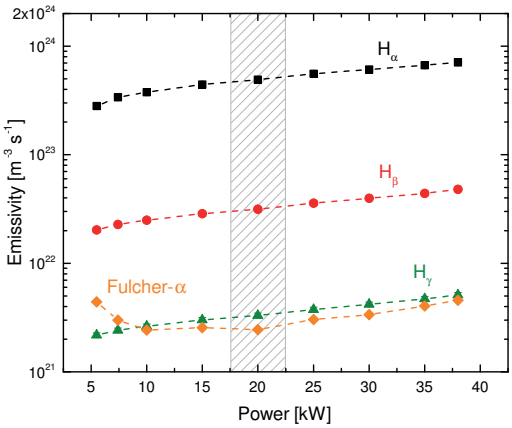

Figure 3.19 – Emissivities of the atomic Balmer and of the molecular Fulcher radiation at varying RF power without applying a magnetic cusp field. The grey hatched area shows the region where the optimum source performance is typically achieved.

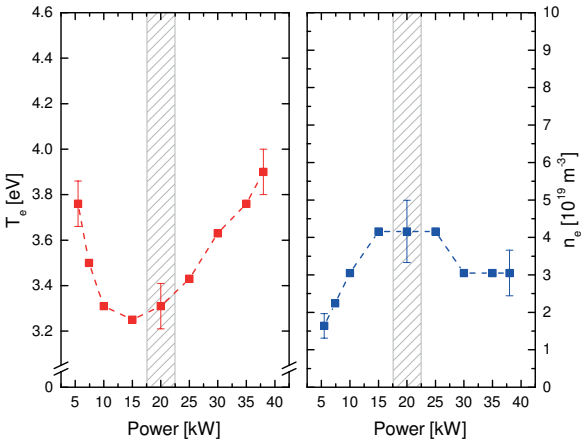

Figure 3.20 – Electron temperature T_e and electron density n_e evaluated from the OES measurements for varying RF power without applying a magnetic cusp field. The grey hatched area shows the region where the optimum source performance is typically achieved.

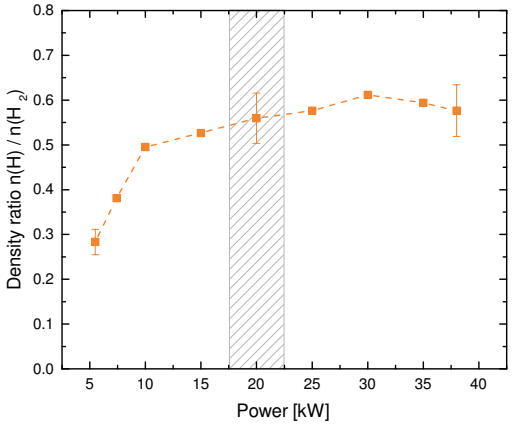

Figure 3.21 – Density ratio of atomic to molecular hydrogen obtained from the OES measurements for varying RF power without applying a magnetic cusp field. The grey hatched area shows the region where the optimum source performance is typically achieved.

influence the H^- yield as both reaction rates depend linearly on n_e. Concerning the electron temperature, a low value of T_e is highly beneficial for the H^- yield as the production rate increases with lower electron energy and also the destruction rate decreases. Furthermore, the vibrational excitation of the electronic ground state of hydrogen influences the production rate considerably as the formation process is more efficient the higher the vibrational excitation. A variety of processes such as cascades from higher lying electronic states or reformation of hydrogen atoms where parts of the binding energy is converted into vibrational excitation contribute to the vibrational population. Many of those processes happen on time scales being larger than the discharge pulse length of 500 μs leading to the fact that the vibrational distribution is far off from equilibrium in the ion source plasma. Nevertheless, the vibrational population of the first four levels ($v' = 0,\ldots 3$) is accessible via summing up over the rotational population measured in each vibrational state. In doing so, a vibrational temperature can be determined and a maximum of this temperature is obtained at an RF power of 20 kW. Concerning the density ratio of atomic to molecular hydrogen, a higher value is in general adhere to a large H^- production rate as there are less molecules available. However, for low RF powers where $n(H)/n(H_2)$ is low, the vibrational temperature is low and the electron temperature is high. In summary these considerations can explain that the best performance of the ion source is achieved at 20 kW as a low electron temperature and a high vibrational excitation is obtained.

RF power variation with cusp field

The operational range of the ion source is shifted to higher values when the cusp magnets are installed: instead of 5 – 40 kW without cusp, the RF power can be varied between 10 and 70 kW. This behaviour arises from the fact that the cusp field is designed in a way that prevents the electrons from getting close to the wall of the discharge vessel where the heating RF field is

most intense. As the over-all heating capability is therefore reduced, the RF power demand is higher when the cusp magnets are installed in the ion source.

Figure 3.22 shows the emissivities measured with cusp field. As already stated, the best ion source performance is achieved around 40 kW which is a factor of two higher than without magnets. The general trends of the emissivities are the same as observed without cusp magnets: the emissivity of the atomic Balmer lines increases steadily with power whereas the molecular Fulcher emission shows a minimum, lying now between 15 and 30 kW. Furthermore, the absolute intensities are higher with cusp magnets.

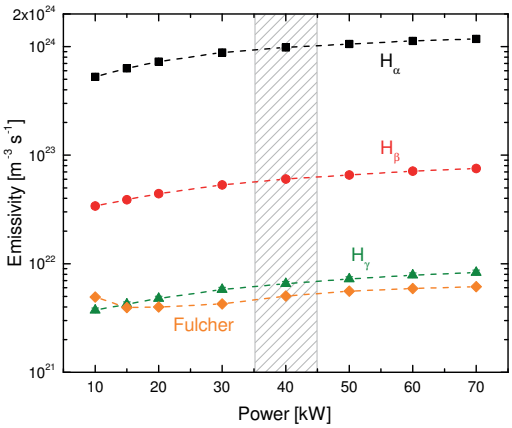

Figure 3.22 – Emissivities of the atomic Balmer series and the molecular Fulcher transition for varying RF power with applying a magnetic cusp field. The grey hatched area shows the region where the optimum source performance is typically achieved.

During the comparison of the general plasma parameter trends, it turned out that the behaviour is very similar for installed cusp magnets or removed ones. However, the higher power demand with cusp magnets is also mirrored in the plasma parameters: for similar discharge conditions the required RF power is around a factor of two higher than without magnets. Figure 3.23 show the electron temperature and density obtained with cusp. For comparison, the values determined without cusp field are also included, an additional x-axis in blue colour has been introduced at the top of the graph (this axis is scaled by a factor of two compared to the x-axis at the bottom of the graph). It can clearly be seen that the same general trends are observed for T_e and n_e with and without cusp magnets: a minimum in the electron temperature and a maximum in the electron density for varying RF power. With cusp field, higher absolute values of T_e and n_e are obtained and the position of the extremes is slightly shifted from the point of optimum source performance to lower RF powers. The same is true for the vibrational temperature reaching a maximum at 30 kW. Concerning the density ratio of atomic to molecular hydrogen (see Figure 3.24), not only the same general trend is observed but also comparable absolute values over the whole RF power range are obtained for both cases.

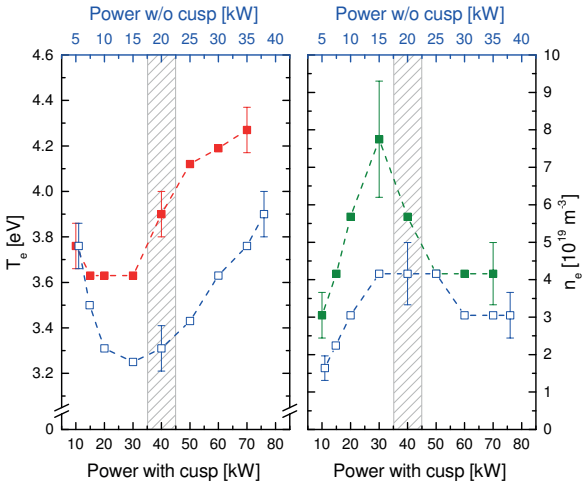

Figure 3.23 – T_e and n_e obtained from the OES evaluation for varying RF power and with applying a magnetic cusp field (full symbols). The open symbols reflect the results obtained without cusp field and belong to the upper x-axis. The grey hatched area shows the region where the optimum source performance is typically achieved with and without cusp magnets.

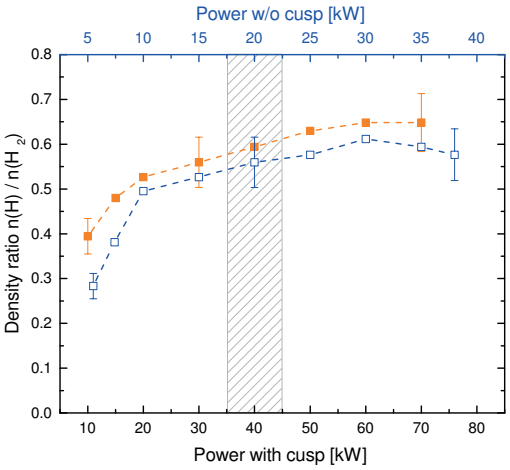

Figure 3.24 – Density ratio of atomic to molecular hydrogen obtained from the OES evaluation for varying RF power and with applying a magnetic cusp field (full symbols). The open symbols reflect the results obtained without cusp field and belong to the upper x-axis. The grey hatched area shows the region where the optimum source performance is typically achieved with and without cusp magnets.

Therefore, the optimum source performance would be expected at an RF power of 30 kW as the electron temperature has its lowest value there and the vibrational excitation is highest. However, the highest H^- current is achieved at 40 kW of RF power. Furthermore, the absolute value of T_e is lower without cusp magnets what should result in a higher H^- yield, but the ion source performance is better with magnets. In order to assess the reasons for these differences in expected and observed performance, it should be kept in mind that a rather large plasma volume is probed by OES due to the inherent line-of-sight integration whereas the H^- ions are actually extracted from only a small region close to the extraction aperture. In addition, different plasma parameter profiles (which will especially be present when comparing the plasma with and without cusp field) cannot be assessed and considered in the OES evaluations. Such spatial variations of the plasma need to be considered in order to explain the performance differences with and without cusp field.

3.3.6 SUMMARY AND CONCLUSION

In order to assess the different performance of the Linac4 H^- ion source with respect to the application of cusp field magnets, optical emission spectroscopy measurements have been carried out while operating the ion source in volume mode. Typically, the extracted H^- current shows a maximum at varying RF power of 15 – 20 mA at 20 kW without cusp magnets and of 25 – 30 mA at 40 kW with cusp field. In both cases, the electron temperature shows an initial decrease with RF power before it rises again whereas the electron density shows a contrary peaking behaviour. An assessment of the relevant production and destruction processes of H^- predicted a maximum H^- yield at 20 kW which is exactly the value where the best ion source performance is achieved.

When the cusp magnets are applied, their field topology prevent the electrons from getting close to the wall of the discharge vessel where the intense RF fields are located. Therefore, a higher RF power is required to reach similar discharge parameters as without cusp field. This can be seen in all determined parameters, as the observed general trends for varying RF powers are shifted by a factor of two to higher powers when the cusp magnets are installed. Considering the H^- yield, the predicted RF power for best performance is at 30 kW whereas the highest current is actually achieved at 40 kW. Furthermore, a higher H^- yield is expected when the cusp magnets are not installed, but the contrary behaviour is observed. These differences can most likely be attributed to changes in the plasma parameter profiles which cannot be accessed by optical emission spectroscopy. Nevertheless, the obtained plasma parameters can be used as benchmark values for RF coupling codes simulating the Linac4 ion source [110, 111, 16].

3.3.7 ACKNOWLEDGMENTS

The authors would like to thank the Deutsche Forschungsgemeinschaft (DFG) for their support within the project BR 4904/1-1.

This work has been carried out within the framework of the EUROfusion Consortium and has received funding from the Euratom research and training programme 2014-2018 under grant agreement No 633053. The views and opinions expressed herein do not necessarily reflect those of the European Commission.

4 Investigation of the hydrogen plasma in the Linac4 H^- ion source

The implicit PIC simulations of the hydrogen plasma inductive heating provide insights into the influence of operational and design parameters on the plasma discharge. We performed a parameter scan of the RF current I_{RF}, gas pressure p_{H_2} and magnetic configuration (cusp, filter) to assess their impact on the plasma densities and energy distributions. Maximizing the H^- density in the beam formation region is of utmost importance. The simulated plasma parameters represent key boundary conditions to beam formation and extraction software packages [63, 40], simulating effective beam intensities and emittances.

4.1 Plasma heating dynamics

We present the time structure of the plasma evolution for the conditions p_{H_2} = 3 Pa and I_{RF} = 100 A in the absence of external magnets. The numerical parameters and initial conditions are listed in table 4.1, chosen from previous convergence tests and simulation results. The plasma is initially loaded uniformly in the plasma chamber. The neutral population is initially composed of only H_2 with a vibrational temperature of 3000 K obtained from measurements in similar conditions.

Numerical parameter		**Initial conditions**	
Cell size ($\Delta r \times \Delta z$)	1×2 mm	Particle number	455'000
Time step	$2.5{\cdot}10^{-11}$ s	H_2 temperature	300 K
Particle weight	10^9	Dissociation degree	0
RF coil current	100 A	Vibrational temperature	3000 K
RF coil turns	5	e^- density	10^{18} m^{-3}
Gas pressure	3 Pa (@300K)	e^- temperature	1 eV
		Ion temperature	0.1 eV
		Ion distrib. H^+:H_2^+:H_3^+	80%:10%:10%

Table 4.1 – Numerical parameters and initial conditions used for the investigation of the design and operational parameters on the hydrogen plasma discharge.

Figure 4.1 shows the evolution of the average plasma densities from the initial condition to steady-state. The plasma heating process is strongly influenced by the 2 MHz driving frequency. The electron density stabilizes around $n_e = 8 \cdot 10^{18}$ m^{-3} during the first 10 μs of simulation. The ion populations require $\approx 20\ \mu s$ to redistribute and stabilize at 88% H^+, 9% H_2^+ and 3% H_3^+, with H^- on average 0.5% of the plasma density. After 25 μs the neutrals reach steady state with $n_H = 2.3 \cdot 10^{20}$ and $n_{H_2} = 6.1 \cdot 10^{20}$ (summed over v) giving a dissociation degree $n_H/(n_H + n_{H_2}) = 0.27$.

The evolution of the vibrational population is shown in figure 4.2. Within the 25 μs of simulation the density of vibrationally excited molecules also reaches steady state and it is characterized by a two-temperature distribution with $T(v \leq 4) = 4500\ K$ and $T(v \geq 5) = 15000$ K as illustrated in figure 4.3. The population of high vibrational states is key to increase the volume production of H^- via dissociative attachment of low energy electrons in the beam formation region (see section 1.5.1).

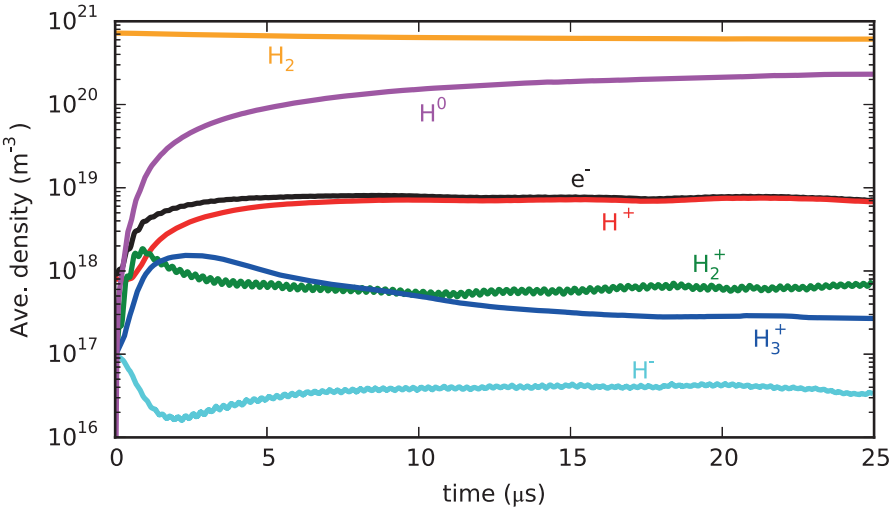

Figure 4.1 – Plasma evolution for the simulation without external magnets at $p_{H_2} = 3$ Pa and $I_{RF} = 100$ A. The positive ion populations (H^+, H_2^+, H_3^+), the electron, H^- and the neutrals are indicated. All densities are averaged over the volume of the plasma chamber.

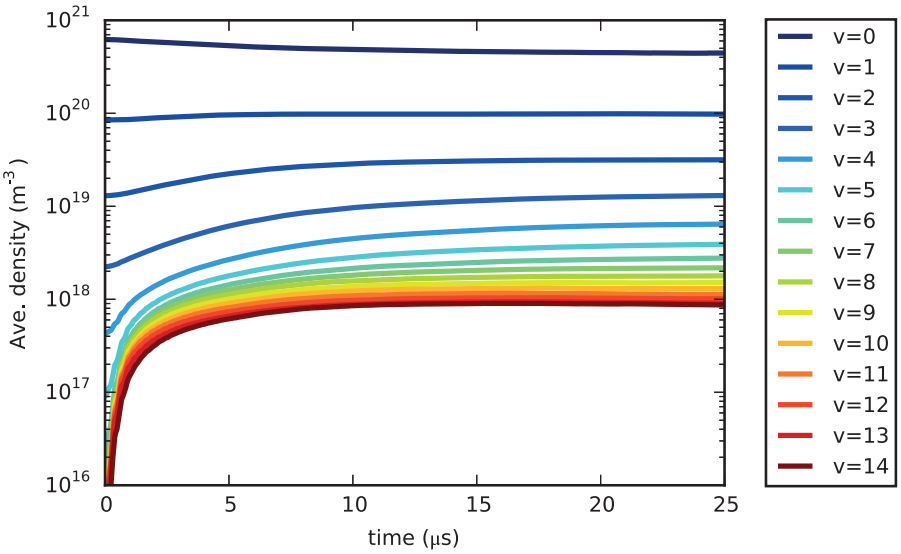

Figure 4.2 – Time evolution of the $H_2(v)$ vibrational population for the simulation without external magnets at p_{H_2} = 3 Pa and I_{RF} = 100 A.

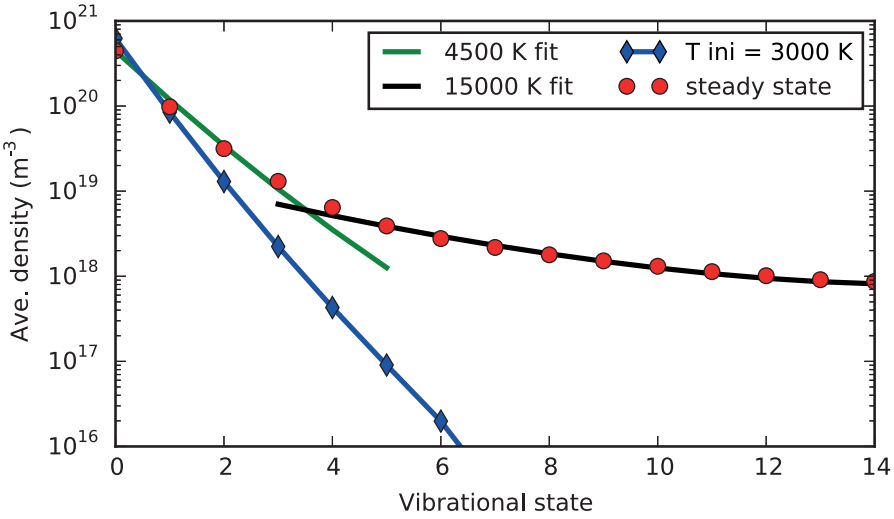

Figure 4.3 – Initial and steady state vibrational temperatures for the simulation without external magnets at p_{H_2} = 3 pa and I_{RF} = 100 A. A two-temperature distribution is observed at steady state.

4.2 Coil current and effect of the magnetic cusp field

The analysis of the E-H transition indicated that the magnetic cusp field prevented electrons close to the plasma chamber wall to be accelerated by the induced electric field. This resulted in a reduction of the inductive power deposited to the plasma in comparison to the configuration without cusp field. We have extended the study for the high density regime, performing a scan of the coil current I_{RF} with and without cusp field to investigate its effect on the plasma. Figure 4.4 shows the average electron density as a function of I_{RF} with and without cusp field. In the range analysed the electron density scales almost linearly with I_{RF} in both configurations. In the presence of the cusp field a factor 2 larger current is required to achieve the same density.

The reason for this behaviour is better revealed by looking at the density and energy profiles. We have compared the simulation without cusp field at I_{RF} = 100 A and the simulation with cusp at I_{RF} = 200 A, which produce the same average density. Figure 4.5 shows the radial profile of the electron density and energy in the coil region (averaged in z direction for the length of the coil). In the presence of the cusp field, the electron density is higher in the center of the plasma chamber and drops more rapidly in the radial direction. This is in agreement with the confinement effect expected when employing the magnetic cusp. The electron energy profiles show significant differences in the two configurations. When no cusp field is employed, the electron energy peaks in the region close to the wall, where the inductive field is largest. In the presence of the cusp field, electrons close to the wall cannot be accelerated, and the energy profile peaks at r=8 mm.

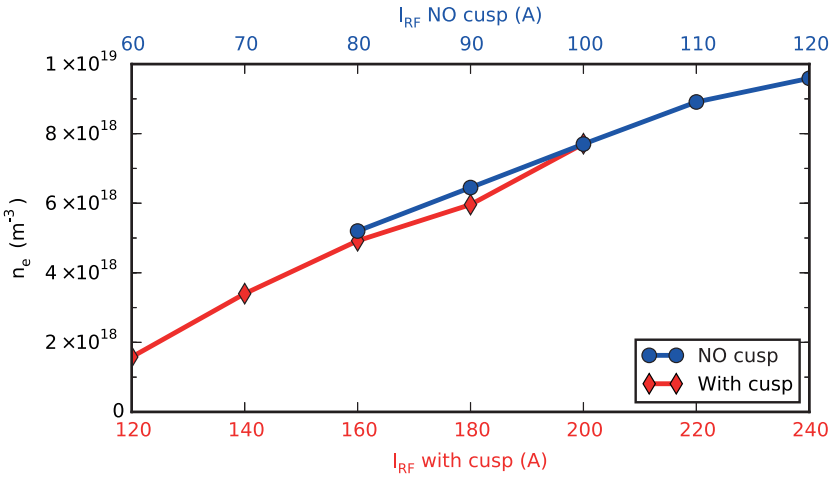

Figure 4.4 – Average electron density n_e as a function of the RF current I_{RF} in the configuration with and without magnetic cusp field.

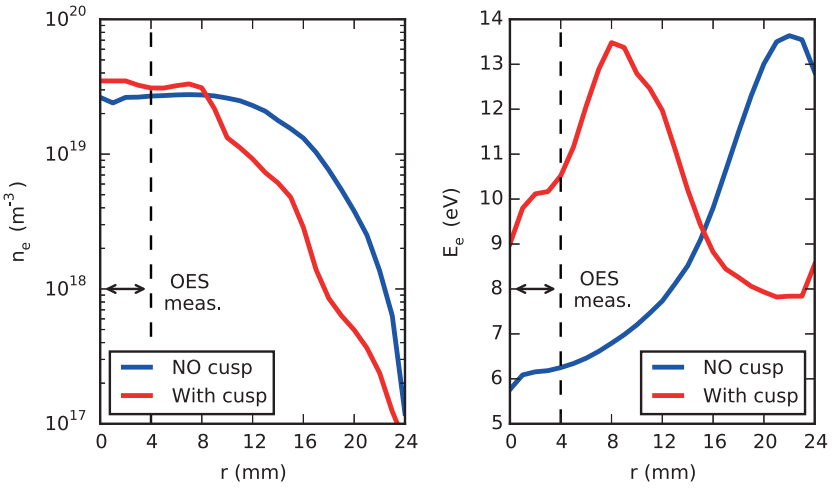

Figure 4.5 – Electron density n_e and electron energy E_e radial profile in the coil region (averaged in the axial direction). The simulation without cusp field is for I_{RF} = 100 A whereas the simulation with cusp field is for I_{RF} = 200 A, producing the same volume averaged density. The view port used for Optical Emission Spectroscopy (OES) has a capture angle of 3°, corresponding to approximately 4 mm radius in the center of the plasma chamber.

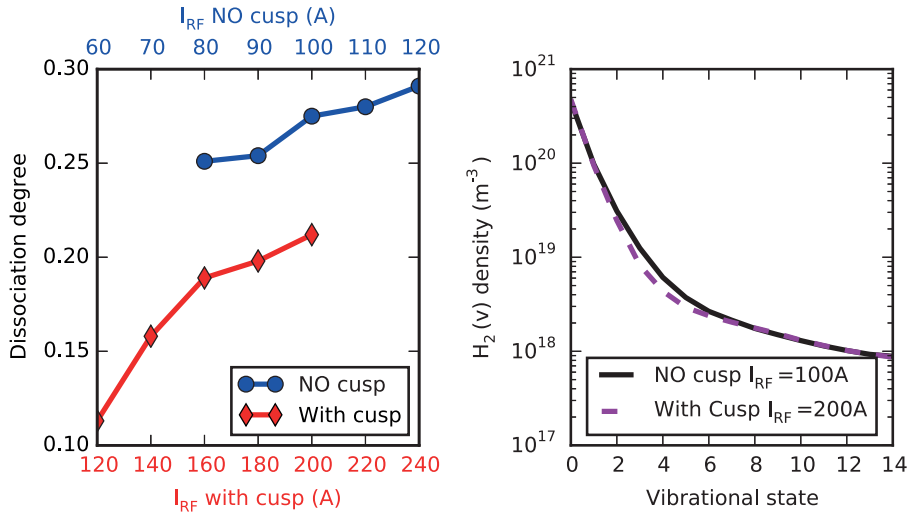

Figure 4.6 – Left) Dissociation degree $n_H/(n_H + n_{H_2})$ as a function of the coil current I_{RF} in the configuration with and without cusp field. Right) Density of vibrationally excited molecules for the simulation without cusp field at I_{RF} = 100 A and with cusp at I_{RF} = 200 A producing the same volume averaged electron density.

The simulation results show good agreement with OES measurements, where a factor 2 in the RF power was required to achieve the same density in the configuration with cusp field (section 3.3). This gives us confidence that the external magnetic field is handled properly in the code.

Concerning the neutrals, a slightly larger dissociation degree is observed in the configuration without cusp field in the whole range analysed (figure 4.6 left). On the other hand, the vibrational temperature of highly excited states $T_{vib}(v \geq 5)$ shows no substantial difference between the two configurations (figure 4.6 right). The impact of I_{RF} on the density of vibrationally excited molecules is unnoticeable and it is not shown in the plot. This result indicates that also concerning the neutrals a factor 2 larger current is required to achieve the same dissociation degree and density of vibrationally excited molecular states. The comparison to OES measurements shows that the simulations slightly underestimate the dissociation degree in both configurations, with a larger deviation in the presence of the cusp field. This could be ascribed to uncertainties in the estimated pressure measured as well as in the recombination coefficients used in the simulations (note that figure 3.24 reports the density ratio and not the dissociation degree). The detailed analysis of the H^- production in the beam formation region will be described in section 4.3 in the presence of the magnetic filter field.

4.3 Effect of the filter field

The aim of the filter field is to separate the heating region, where highly energetic electrons lead to vibrational excitation and dissociation, from the beam formation region where cold electrons are required to form H^- via DA and minimize the destruction processes. The electron energy E_e drop is due to an increased residence time of electrons trapped in the magnetic filter field, which by collisional losses, diffuse to a lower E_e in the beam formation region [39].

We have applied a filter field with a strength of 18 mT, measured on the axis of the plasma chamber, in order to assess its effectiveness. Figure 4.7 and 4.8 compare the electron density n_e, electron energy E_e and volume produced H^- density n_{H^-} 2D profiles with and without filter field respectively for the simulation without cusp field at I_{RF} = 100 A, p_{H_2} = 3 Pa. The plots correspond to the time averaged data during the last μs of simulation (interval 24 to 25 μs). In the presence of the filter field, a drop in n_e and particularly of E_e is clearly visible in the beam formation region (z > 118 mm). A lower E_e is beneficial for the production of H^- by DA, and results in a significant increase of volume produced H^-. It is interesting to notice that the effect of the filter field is not limited to the beam formation region. Due to the penetration of the filter field into the heating region, a lower E_e is observed in the proximity to the coil. Electrons are no longer free to accelerate in the azimuthal direction and this results in a reduced heating efficiency. For the case considered we observe a factor 2 lower electron density averaged over the plasma chamber volume when the filter field is applied. This indicates that, although the filter field is required to enhance the H^- volume production, its penetration to the heating region should be limited not to compromise the plasma heating process.

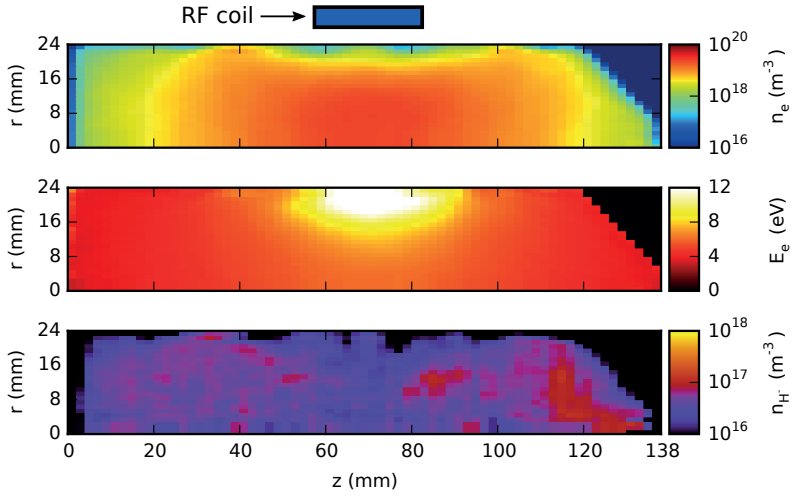

Figure 4.7 – From top to bottom: electron density n_e, electron energy E_e and volume produced H^- density n_{H^-} for the simulation without external magnets at I_{RF} = 100 A and p_{H_2} = 3 Pa. The position of the RF coil is indicated. The largest electron density and energy is observed in the region where the coil is located. n_{H^-} is two orders of magnitude lower than n_e.

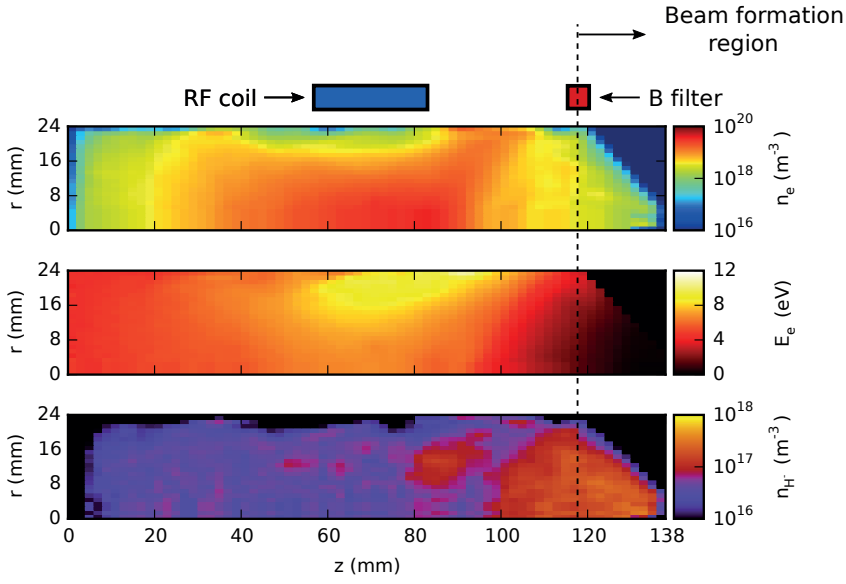

Figure 4.8 – From top to bottom: electron density n_e, electron energy E_e and volume produced H^- density n_{H^-} for the simulation with a magnetic filter field of 18 mT on the center of the plasma chamber, at I_{RF} = 100 A and p_{H_2} = 3 Pa without cusp field. The position of the RF coil and magnetic filter field is indicated. The beam formation region is defined as the region for z > 118 mm. A lower n_e and E_e is observed in the beam formation region, accompanied by an increase of n_{H^-}.

4.3.1 H⁻ and electron densities as a function of the coil current

The H⁻ and electron densities in the beam formation region (z > 118 mm, see figure 4.8) represent critical parameters to characterize the performance of the ion source plasma generator. Figure 4.9 shows the density of volume produced H⁻ (n_{H^-}) and the electron density n_e in the beam formation region for varying RF coil current I_{RF} and constant filter field strength of 18 mT. Both n_e and n_{H^-} increase with increasing I_{RF}. The electron to H⁻ density ratio (n_e/n_{H^-}) also increases for increasing I_{RF}, indicating that at higher I_{RF} the efficiency of the H⁻ volume production decreases. This result is ascribed to the higher electron energy resulting from increased I_{RF}, which is less beneficial for the H⁻ volume production. For comparison, the simulation with cusp field at I_{RF} = 200 A shows similar densities, electron energy and n_e/n_{H^-} as the simulation without cusp at I_{RF} = 100 A. This confirms that also concerning the volume produced H⁻ density a factor 2 larger coil current is required in the configuration with cusp field.

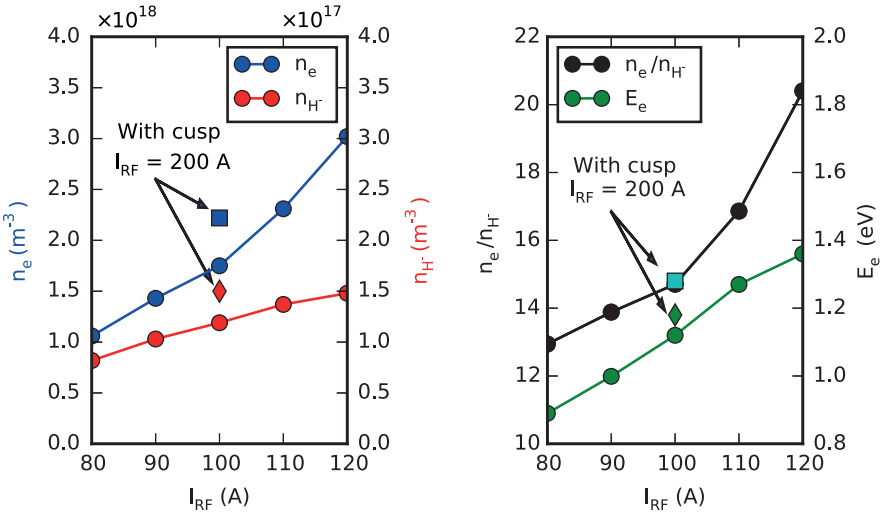

Figure 4.9 – Left) electron density n_e and volume produced H⁻ density n_{H^-} in the beam formation region as a function of the coil current I_{RF}. Right) electron to H⁻ density ratio n_e/n_{H^-} and electron energy E_e as a function of I_{RF}.

4.3.2 Hydrogen atomic flux onto the plasma electrode

The most efficient channel of surface production is backscattering of hydrogen atoms H^0 from low work function surfaces [36]. We have characterized the flux of H^0 impinging on the plasma electrode over the last μs of simulation. The H^0 energy distribution is shown in figure 4.10. It is characterized by a low-energy (≤ 5 eV) non-thermal component and a thermal high-energy component with temperature T = 2.5 eV for the configuration without cusp field at I_{RF} = 100 A. In the presence of cusp field the high-energy thermal component increases to T = 4.0 eV for the

simulation at I_{RF} = 200 A. In both cases the thermal component corresponds to the simulated positive ion temperature.

The H^0 production channel with the highest cross-section is the dissociation of H_2 via the repulsive $b^3\Sigma_u^+$ state [34]. The two "newborn" H^0 receive initially a share of the dissociation energy of 4.5 eV. Part of the H^0 will reach the plasma electrode before thermalizing to the positive ions and contribute therefore to the non-thermal low-energy component. By number, the low-energy component is more than one order of magnitude larger than the thermal one in both configurations. The higher temperature in the configuration with cusp field is the result of a higher inductive electric field, due to a factor 2 larger coil current.

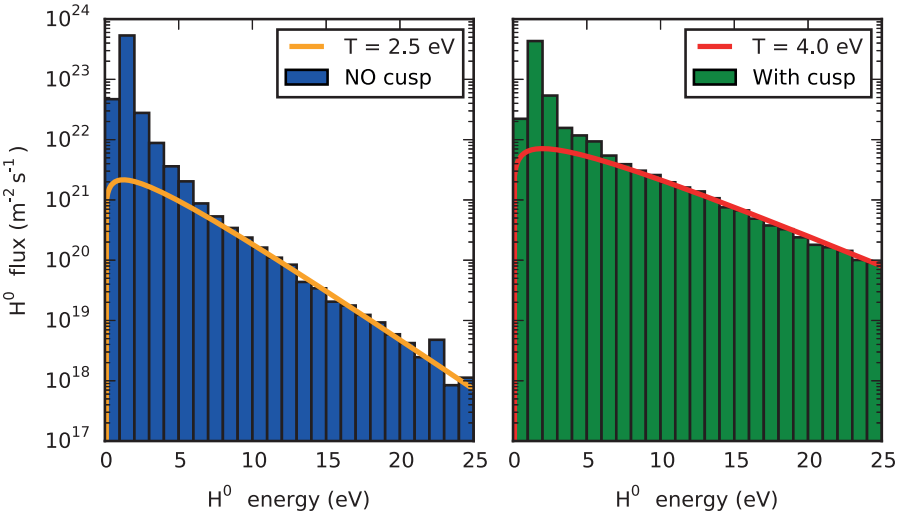

Figure 4.10 – Energy distribution of the H^0 flux impinging onto the plasma electrode. The simulation without cusp field (left) corresponds to a coil current I_{RF} = 100 A, whereas the simulation with cusp field (right) corresponds to a coil current I_{RF} = 200 A. In both configurations the energy distribution is characterized by a low-energy (< 5 eV) non-thermal component and a high-energy thermal component corresponding to the temperature of the positive ions.

The conversion of the impinging H^0 to H^- happens by electron transfer from the surface to the atom leaving the surface. The H^- yield depends on the impinging energy and the surface work function [37] as described in section 1.5.2. Figure 4.11 shows the H^- emission rate for a work function from 1.5 to 3.0 eV, covering the range representative of a molybdenum electrode partially to fully covered with cesium. For a work function of 1.5 the emission rate is of the order of 12-15 kA/m^2 for all cases analysed. The emission rate decreases with increasing work function and a larger dependency on the coil current I_{RF} is observed. This result reflects the impact of the high energy component of the H^0 flux distribution as a function of I_{RF}. The conversion from H^0 to H^- requires a minimum threshold energy $E_{th} = \phi - A$ to allow the electron transfer from the surface, where ϕ is the surface work function and A the

electron affinity (0.754 eV for hydrogen). With increasing work function a larger E_{th} is required, implying that the high-energy component of the H^0 flux is more effectively contributing on the H^- emission rate. The percentage of the emission rate as a function of the H^0 energy distribution and the work function is shown in figure 4.12.

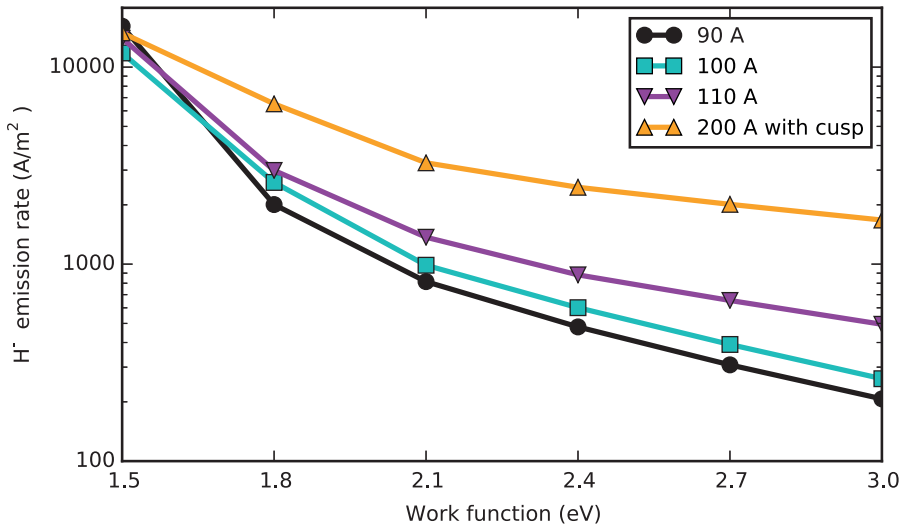

Figure 4.11 – H^- emission rate from the plasma electrode due to backscattering of impinging H^0. A work function of 1.5 eV corresponds to the dynamically cesiated molybdenum surface [37] whereas 2.1 eV is the work function of bulk cesium. Unless indicated the coil current corresponds to the simulation without magnetic cusp field.

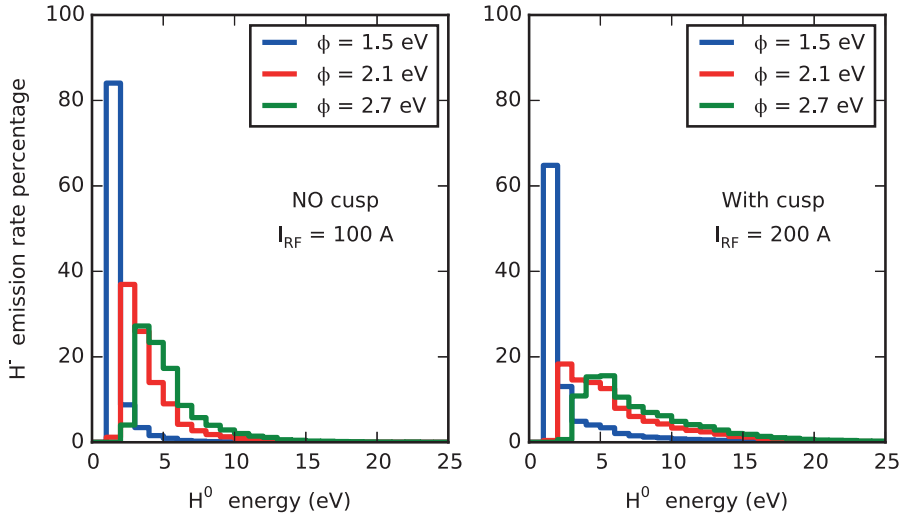

Figure 4.12 – Percentage of H^- emission rate as a function of the impinging H^0 energy for different work function ϕ (histogram binning of 1 eV).

4.3.3 Variation of filter field strength

We have varied the strength of the filter field for the simulation I_{RF} = 200 A with cusp field and investigated the resulting plasma parameters. The characteristic value of the filter field strength is the one obtained at z = 118 mm (position of the magnets) on the plasma chamber axis.

Figure 4.13 shows the axial profiles of the electron density and energy in the region from the RF coil to the plasma electrode. By increasing the strength of the filter field, a reduction of the electron density and energy is obtained in the beam formation region for all cases analysed. The energy profile shows a different behaviour in the region ahead of the filter field. For 6 mT, the energy increases compared to the case without filter field due to additional confinement induced by the filter field. With increasing filter field strength this trend is displaced towards the heating region.

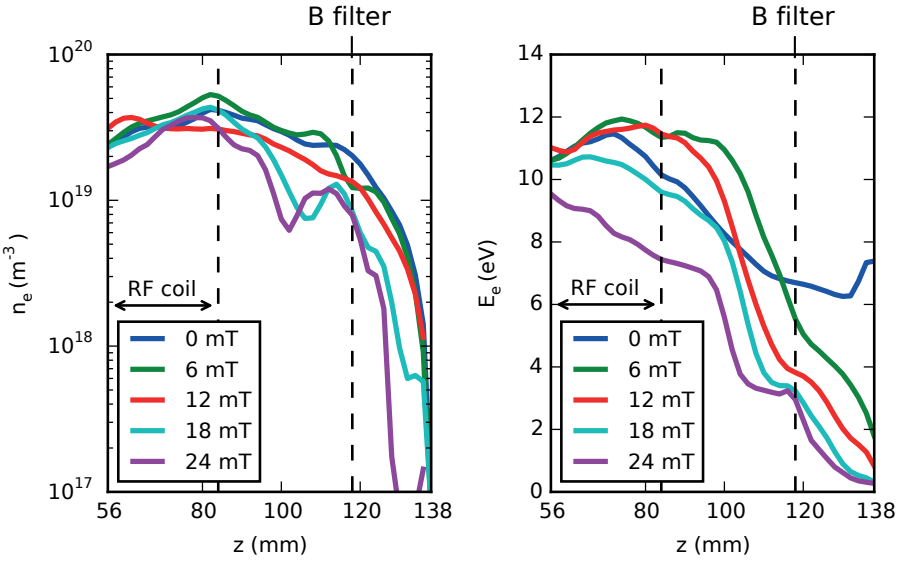

Figure 4.13 – Electron density n_e and electron energy E_e axial profile from the RF coil to the plasma electrode as a function of the filter field strength. The values are averaged over 5 mm radially in the plasma chamber center and are representative of the simulation with I_{RF} = 200 A. The location of the RF coil and the filter magnets are indicated.

The ion source optimal condition maximizes the H^- density in the beam formation region, accompanied by a minimization of the electron density. Figure 4.14 shows the average electron and H^- density in the region z > 118 mm as a function of the filter field strength, together with the electron to H^- density ratio. The electron density drops monotonically whereas the H^- density shows a maximum density for 12 mT. On the other hand, the electron to H^- ratio (e/H) monotonically decreases with increasing filter field strength.

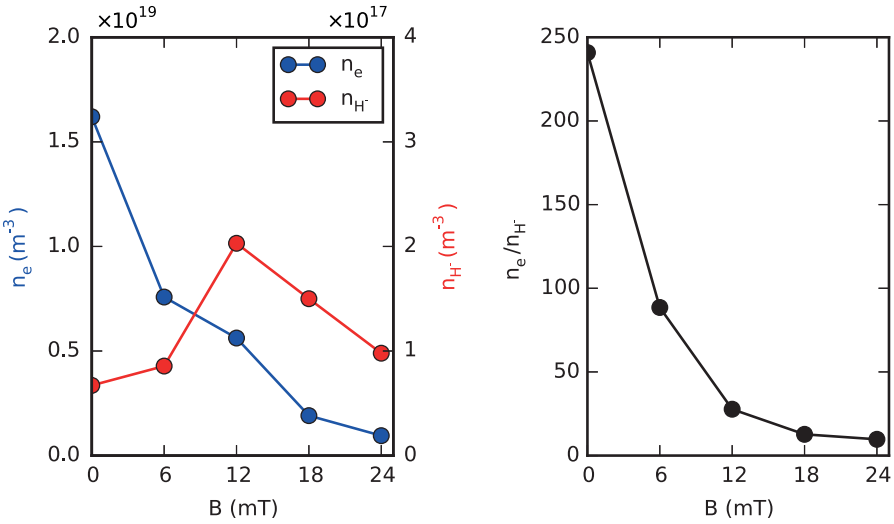

Figure 4.14 – Left) average electron density n_e and H^- density n_{H^-} in the beam formation region ($z > 118$ mm). Right) electron to H^- density ratio (n_e/n_{H^-}).

4.4 Influence of the H_2 pressure

The plasma heating in the pressure range 1-5 Pa has been simulated with a constant coil current I_{RF} = 100 A without magnetic cusp and with a filter field of 18 mT. The volume averaged electron density increases with increasing pressure, accompanied by a decrease of the electron energy as shown in figure 4.15. The atomic density also increases with increasing pressure, although the dissociation degree drops from 0.33 to 0.20 from 1 Pa to 5 Pa respectively. Above 3 Pa the increase is less pronounced and there is tendency towards saturation (figure 4.16). The density of vibrationally excited molecules shows a monotonic increase as a function of the pressure. The two temperature distribution of $H_2(v)$ is visible at all pressures analysed, although a sharper transition is observed for lower pressures at $v = 3-5$.

In the beam formation region (z > 118 mm) the electron and H^- density increase with increasing pressure as shown in figure 4.17. Due to a decrease of the electron energy E_e the H^- volume production becomes more efficient for higher pressures, resulting in a reduction of the electron to H^- density ratio. This indicates that a higher p_{H_2} is beneficial for the operation of the ion source in volume mode.

The energy distribution of the H^0 flux impinging on the plasma electrode is shown in figure 4.18 for the simulations at 2 and 4 Pa. The higher atomic density observed for increasing pressures results in a larger integrated flux, which mainly contributes to the low-energy component. On the other hand, a lower temperature of the high energy component is observed for increasing pressures. This has a direct impact on the H^- emission rate (figure 4.19): for a work function < 1.8 eV the low-energy component has a significant contribution to the emission rate which

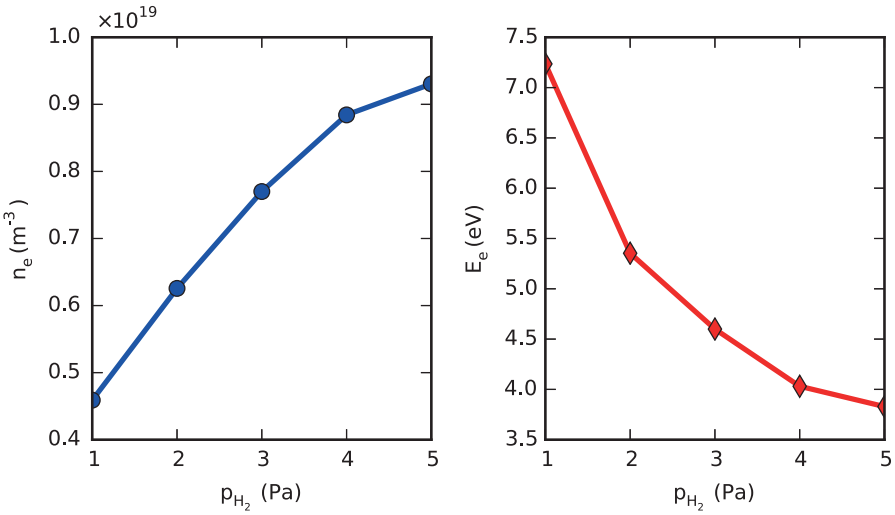

Figure 4.15 – Volume averaged electron density n_e (left) and energy E_e (right) as a function of the hydrogen pressure p_{H_2}.

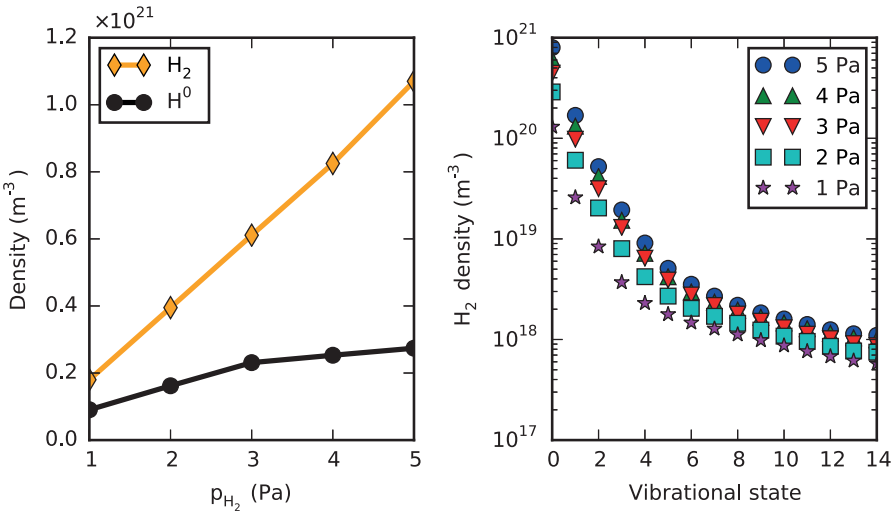

Figure 4.16 – Left) Volume averaged density of H^0 and H_2 (summed over v) as a function of the hydrogen pressure p_{H_2}. Right) Density of vibrationally excited $H_2(v)$ as a function of the hydrogen pressure p_{H_2}.

increases for increasing pressures. For work functions > 2 eV the opposite trend is observed, with a reduction of the emission rate for increasing pressures.]

This result has a critical consequence for the operation of the ion source. Taking as reference the work function of bulk cesium of 2.1 eV, the impact of the hydrogen pressure has opposite trends in terms of volume and surface produced H⁻. Whereas the volume produced H⁻ density increases for increasing pressure, the surface H⁻ emission rate drops. This implies that the optimal operating point will correspond to the best compromise between the two production modes.

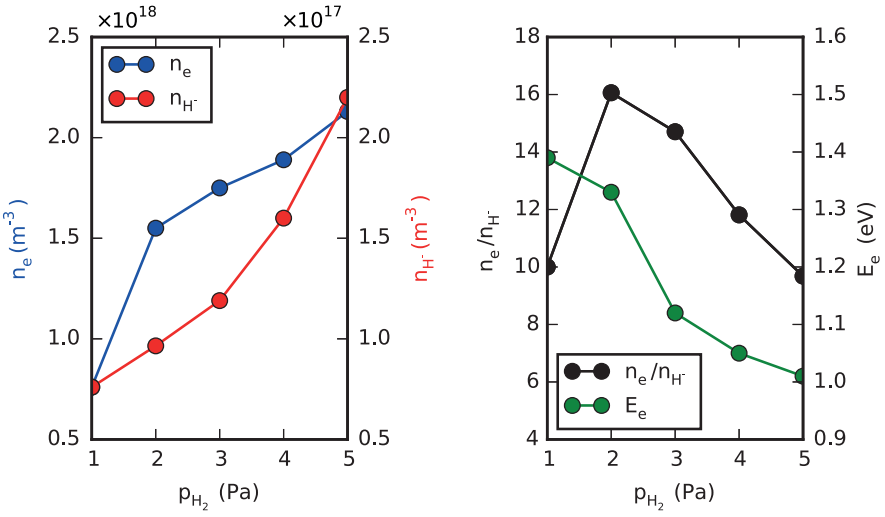

Figure 4.17 – Left) electron density n_e and volume produced H⁻ density n_{H^-} in the beam formation region as a function of the hydrogen pressure p_{H_2}. Right) electron to H⁻ density ratio n_e/n_{H^-} and electron energy E_e as a function of p_{H_2}.

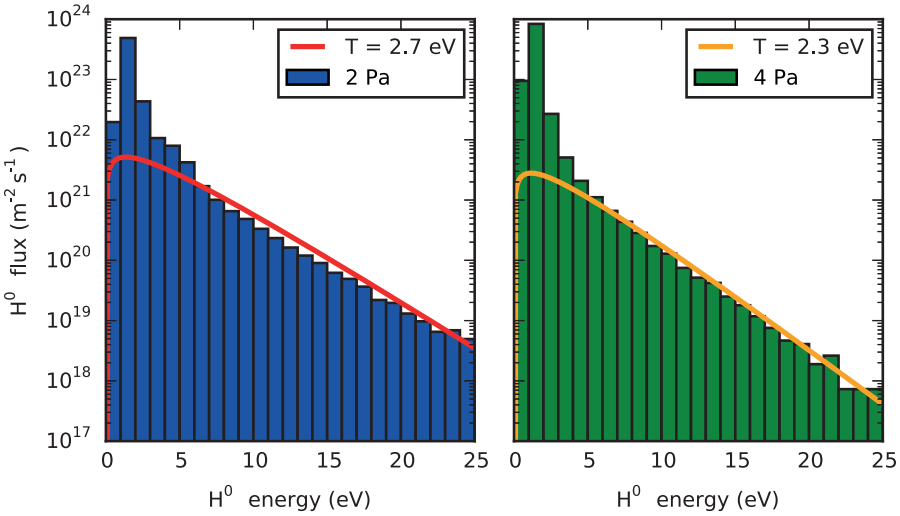

Figure 4.18 – Energy distribution of the H^0 flux impinging onto the plasma electrode for the simulation without cusp field at p_{H_2} = 2 Pa (left) and p_{H_2} = 4 Pa (right) for I_{RF} = 100 A. The energy distribution is characterized by a low-energy (< 5 eV) non-thermal component and a high-energy thermal component corresponding to the temperature of the positive ions, inversely proportional to the hydrogen pressure.

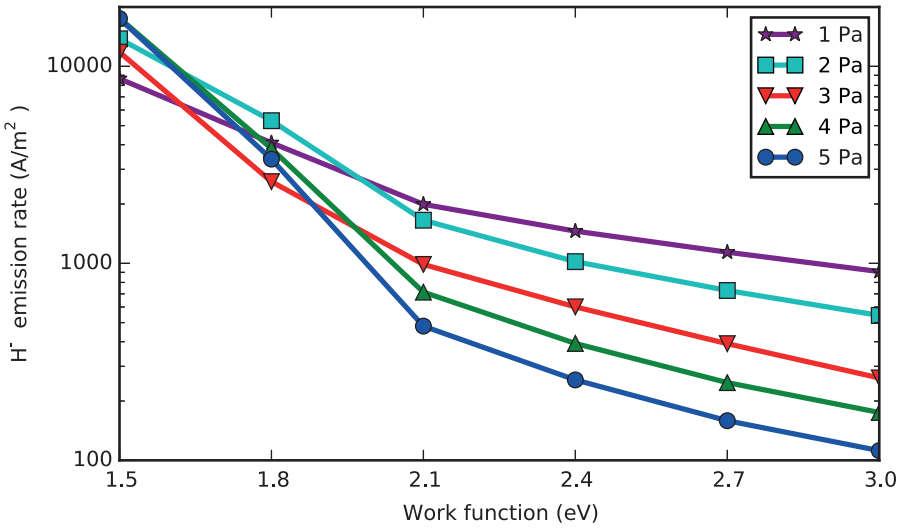

Figure 4.19 – H^- emission rate from the plasma electrode due to backscattering of impinging H^0. A work function of 1.5 eV corresponds to the dynamically cesiated molybdenum surface [37] whereas 2.1 eV is the work function of bulk cesium.

4.5 Coupling to beam formation and extraction codes

The analysis performed with the NINJA code allowed quantifying the impact of the hydrogen pressure, RF coil current and external magnet configuration on the plasma parameters. Optimization of the operational conditions is equivalent to maximising the volume produced H^- density and H^- surface emission, together with a minimization of the electron density in the beam formation region.

The NINJA code is designed to accurately simulate the RF plasma heating mechanism. The underlying physics requires a cell size capable of resolving the structure of the plasma skin depth, which in the Linac4 ion source regime is in the order of few mm. In the beam formation region however, the plasma sheath in the proximity of the wall plays a crucial role in defining the local densities close to the extraction hole and thus to the extracted beam. The size of the plasma sheath is few Debye lengths and corresponds in this density regime to 20-30 μm. Furthermore a full 3D simulation is mandatory in the beam formation region to address asymmetries induced by the filter field on the beam. This implies that, in order to simulate and optimize the beam extracted from the ion source, the NINJA code needs to be coupled with dedicated beam formation and extraction codes [63, 40] capable of resolving the detailed structure of the beam formation region and the resulting beam shape and emittance.

Beam formation and extraction codes are designed to simulate self-consistently the plasma dynamics and the particle transport in the vicinity of the extraction electrodes. The simulation domain typically includes the beam formation region and the first few mm outside the plasma chamber up to the puller-electrode (figure 4.20). A plasma is initially loaded in the left side of the simulation domain and, as the plasma expands, particle re-injection is used as boundary condition on the walls. The electric potential in the whole 3D volume (including the plasma contribution) is calculated by solving Poisson's equation. The boundary condition on the right hand side is in first order the potential resulting from the voltages and geometries of the plasma- and puller-electrodes calculated under vacuum. The boundary condition is then rather strongly influenced by the space charge of the beam itself and its contribution should be taken into account. External magnetic fields are imported by a 3D field map obtained by a separate software. Collisional processes are handled by a Monte Carlo module, including H^- volume production and destruction processes. H^- surface emission from the cesiated plasma electrode is also included. Further details on the codes can be found in [63, 40].

Beam formation is the interface between the plasma and the extraction field issued by the potential difference between the source and the puller-electrode. The field attracts negative charges (electrons and H^-) and repels positive ones. As a result, a boundary is formed between the plasma and the beam which is called meniscus (also defined as the isopotential line with V = 0). The meniscus shape plays a crucial role on the beam optics during the first stage acceleration and it is influenced by many factors including the local density of charged species, the plasma composition, the extraction potential, the geometry of the puller- and the plasma-electrode.

The composition of the initial bulk plasma as well as the surface emission rate are critical input parameters for beam formation simulations. Previous work [40] relied on estimated values and parameter scans due to the absence of local plasma measurement and of simulated results from the heating region. NINJA can provide precisely these input parameters at the entrance of the beam formation region which shall lead to more realistic simulation results.

The coupling from NINJA to beam formation codes is performed by exporting the 2.5 D plasma parameters from a "coupling region" placed between the plasma heating and beam formation region (figure 4.20). The coupling region is represented by a slab of plasma of thickness Δz in the axial direction, located at a distance z_0 from the extraction plane. The seeds are representative of one RF cycle, once the plasma has reached steady state. The plasma parameters of interest are the densities and energies of the plasma species: e^-, H^+, H_2^+, H_3^+, H^-, H^0, $H_2(v)$. In order to have the most complete output, we export the 6D lists (3 position and 3 velocity components) of all particles present in the coupling region at a given time, together with the weight of each particle (ratio of real particles per simulated one). The output is generated N times during one RF cycle. Furthermore the list of all H^0 impinging onto the plasma electrode during the interval considered are stored in a file including time, position, velocity and weight. The set of data allows reconstructing the essential distributions and provide a complete set of boundary conditions to the beam formation software.

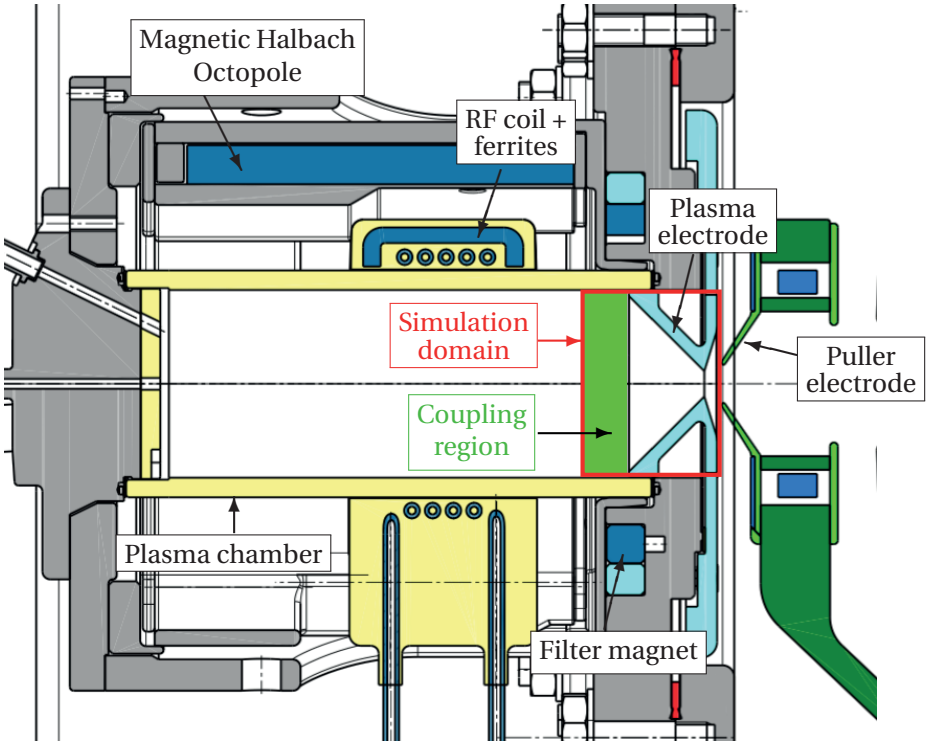

Figure 4.20 – Typical simulation domain of beam formation and extraction codes. The coupling region with NINJA is a slab of plasma at the entrance of the beam formation region, indicated by the green area.

5 Conclusions and outlook

We have characterized the RF-ICP plasma discharge in the Linac4 H^- ion source by numerical simulations and experiments. The code developed for this purpose, called NINJA, represents the first of its kind and has been successfully applied to simulate the high-density low temperature regime of the Linac4 ion source. The usage of a fully-implicit algorithm allowed cell sizes in excess of the Debye length and time steps larger than the plasma period, preserving the conservation of energy while maintaining the computational cost tractable. The simulation results of the electron density, electron energy and H_2 dissociation degree are in excellent agreement with optical emission spectroscopy and photometry measurements.

A survey of operational and design parameters allowed to draw important conclusions that provide insights into the physics of RF-ICP ion sources:

- The use of an external magnetic cusp field surrounding the RF coil prevents electrons in the vicinity of the plasma chamber wall to be accelerated by the RF electric field. This resulted in a factor 2 higher RF coil current to achieve the same average plasma density than in the configuration without cusp field.

- A filter field separating the heating region from the beam formation region is required to enhance the volume production of H^- and reduce the electron density and energy in the beam formation region. We showed that there is an optimal filter field strength to achieve the largest density of volume produced H^-. If the filter field is too weak, the presence of highly energetic electrons in the beam formation region is detrimental to achieve a large H^- population. If the filter field strength is too high, the production rate drops due to an excessive reduction of the electron density and a field penetration in the heating region that reduces the plasma heating efficiency.

- The density of vibrationally excited molecules is characterized by a two temperature distribution with $T(\nu \leq 4)$ in the order of 5000 K, and $T(\nu \geq 5)$ in the order of 15000 K. This result is of paramount importance to determine the density of volume produced H^- via dissociative attachment.

- The H^0 atomic flux onto the Cs-Mo plasma electrode is characterized by a non-thermal low energy component and a high-energy thermal component, whose temperature corresponds to the temperature of the positive ions. H^- emission rates for work functions in the range 1.5 to 3.0 eV were presented.

Optimization of an H^- source performance is a complex mix of: 1) maximization of volume produced H^- in front of the extraction aperture; 2) maximization of the H^- flux generated by the cesiated surface of the plasma electrode; 3) minimization of the co-extracted electron beam; 4) minimization of the beam emittance to optimize the fraction of the beam that will be accepted and accelerated by the Linac.

The results of these simulations provide previously inaccessible input to beam formation and extraction software packages, which rely on the knowledge of the plasma parameters as boundary conditions. This step is key to link the chain of models describing the formation of H^- ion beams, from plasma formation to transport in the accelerating structures. Building on these results, future work will be dedicated to a systematic investigation of the influence of plasma parameters and extraction geometry on the extracted beam optics. This will contribute to a deeper understanding of the beam formation mechanism and pave the way for optimizing the ion source extraction system. In short this work opens the way to proper engineering of the beam formation region for plasma cesiated surface H^- sources.

Bibliography

[1] D. Faircloth, "Ion sources for high-power hadron accelerators," tech. rep., CERN, 2013.

[2] J. Lettry, M. Paoluzzi, Y. Coutron, C. Pasquino, D. Aguglia, P. Moyret, C. Schmitzer, S. Mathot, S. Mattei, E. Chaudeta, *et al.*, "H^- ion sources for CERN's Linac4," in *AIP Conf. Proc.*, vol. 1515 of *CERN-ATS-2013-011*, pp. 302–311, 2013.

[3] J. Lettry, D. Aguglia, P. Andersson, S. Bertolo, A. Butterworth, Y. Coutron, A. Dallocchio, E. Chaudet, J. Gil-Flores, R. Guida, *et al.*, "Status and operation of the Linac4 ion source prototypes," *Review of Scientific Instruments*, vol. 85, no. 2, p. 02B122, 2014.

[4] J. Lettry, D. Aguglia, J. Alessi, P. Andersson, S. Bertolo, A. Butterworth, Y. Coutron, A. Dallocchio, N. David, E. Chaudet, *et al.*, "CERN's Linac4 H^- sources: status and operational results," in *FOURTH INTERNATIONAL SYMPOSIUM ON NEGATIVE IONS, BEAMS AND SOURCES (NIBS 2014)*, vol. 1655, p. 030005, AIP Publishing, 2015.

[5] J. Lettry, D. Aguglia, J. Alessi, P. Andersson, S. Bertolo, S. Briefi, A. Butterworth, Y. Coutron, A. Dallocchio, N. David, E. Chaudet, D. Faircloth, U. Fantz, D. A. Fink, M. Garlasche, A. Grudiev, R. Guida, J. Hansen, M. Haase, A. Hatayama, A. Jones, I. Koszar, J.-B. Lallement, A. M. Lombardi, C. Machado, C. Mastrostefano, S. Mathot, S. Mattei, P. Moyret, D. Nisbet, K. Nishida, M. O'Neil, M. Paoluzzi, R. Scrivens, T. Shibata, D. Steyaert, N. Thaus, and G. Voulgarakis, "Linac4 H^- ion sources," *Review of Scientific Instruments*, vol. 87, no. 02B139, 2016.

[6] S. Briefi, S. Mattei, D. Rauner, J. Lettry, M. Q. Tran, and U. Fantz, "Experimental benchmark of the NINJA code for application to the Linac4 H^- ion source plasma," *submitted to New Journal of Physics*, 2017.

[7] S. Mattei, K. Nishida, M. Onai, J. Lettry, M. Q. Tran, and A. Hatayama, "A fully implicit Particle-In-Cell Monte Carlo code for the simulation of inductively coupled plasmas," *accepted for publication in Journal of Computational Physics*, 2017.

[8] S. Mattei, K. Nishida, M. Onai, J. Lettry, M. Q. Tran, and A. Hatayama, "Numerical simulation of the RF plasma discharge in the Linac4 H^- ion source," in *Proceedings of 5^{th} NIBS conference, Oxford, UK*, 2016.

[9] S. Mattei, K. Nishida, S. Mochizuki, A. Grudiev, J. Lettry, M. Q. Tran, and A. Hatayama, "Kinetic simulations and photometry measurements of the E-H transition in cylindrical inductively coupled plasmas," *Plasma Sources Science and Technology*, vol. 25, no. 6, p. 065001, 2016.

[10] S. Mattei, S. Mochizuki, K. Nishida, T. Shibata, J. Lettry, A. Hatayama, and M. Q. Tran, "RF plasma conductivity in the CERN Linac4 H^- ion source, comparison of simulations and measurements," in *APS Meeting Abstracts*, 2014.

[11] S. Mattei, M. Ohta, M. Yasumoto, A. Hatayama, J. Lettry, and A. Grudiev, "Plasma ignition and steady state simulations of the Linac4 H^- ion source," *Review of Scientific Instruments*, vol. 85, no. 2, p. 02B115, 2014.

[12] S. Mattei, Y. Kawamura, C. Schmitzer, J. Lettry, A. Hatayama, M. Ohta, and M. Yasumoto, "RF plasma modeling of the Linac4 H^- ion source," in *AIP Conf. Proc.*, vol. 1515 of *CERN-ATS-2013-014*, pp. 386–393, 2013.

[13] K. Nishida, S. Mochizuki, M. Ohta, M. Yasumoto, J. Lettry, S. Mattei, and A. Hatayama, "Equivalent circuit of radio frequency-plasma with the transformer model," *Review of Scientific Instruments*, vol. 85, no. 2, p. 02B117, 2014.

[14] K. Nishida, S. Mattei, S. Mochizuki, J. Lettry, and A. Hatayama, "Kinetic modeling of e-to-h mode transition in inductively coupled hydrogen plasmas," *Journal of Applied Physics*, vol. 119, no. 23, 2016.

[15] M. Onai, H. Etoh, Y. Aoki, T. Shibata, S. Mattei, S. Fujita, A. Hatayama, and J. Lettry, "Effect of high energy electrons on H^- production and destruction in a high current dc negative ion source for cyclotron," *Review of Scientific Instruments*, vol. 87, no. 2, 2016.

[16] S. Mochizuki, S. Mattei, T. Shibata, K. Nishida, A. Hatayama, and J. Lettry, "Initial results of a full kinetic simulation of RF H^- source including Coulomb collision process," in *FOURTH INTERNATIONAL SYMPOSIUM ON NEGATIVE IONS, BEAMS AND SOURCES (NIBS 2014)*, vol. 1655, p. 020016, AIP Publishing, 2015.

[17] S. Mochizuki, S. Mattei, K. Nishida, A. Hatayama, and J. Lettry, "Analysis of electron energy distribution function in the Linac4 H^- source," *Review of Scientific Instruments*, vol. 87, no. 2, 2016.

[18] T. Shibata, S. Mattei, K. Nishida, J. Lettry, and A. Hatayama, "Numerical and experimental study of atomic transport and Balmer line intensity in Linac4 negative ion source," in *FOURTH INTERNATIONAL SYMPOSIUM ON NEGATIVE IONS, BEAMS AND SOURCES (NIBS 2014)*, vol. 1655, p. 020008, AIP Publishing, 2015.

[19] T. Shibata, K. Nishida, S. Mochizuki, S. Mattei, J. Lettry, A. Hatayama, A. Ueno, H. Oguri, K. Ohkoshi, K. Ikegami, A. Takagi, H. Asano, and F. Naito, "Numerical study of plasma generation process and internal antenna heat loadings in J-PARC RF negative ion source," *Review of Scientific Instruments*, vol. 87, no. 2, 2016.

[20] I. Goto, K. Miyamoto, S. Nishioka, S. Mattei, J. Lettry, S. Abe, and A. Hatayama, "Effect of coulomb collision on the negative ion extraction mechanism in negative ion sources," *Review of Scientific Instruments*, vol. 87, no. 2, 2016.

[21] A. Grudiev, J. Lettry, S. Mattei, M. Paoluzzi, and R. Scrivens, "Numerical simulation of electromagnetic fields and impedance of CERN Linac4 H^- source taking into account the effect of the plasma," *Review of Scientific Instruments*, vol. 85, no. 2, p. 02B134, 2014.

[22] T. Yamamoto, T. Shibata, M. Ohta, M. Yasumoto, K. Nishida, A. Hatayama, S. Mattei, J. Lettry, K. Sawada, and U. Fantz, "Modeling of neutrals in the Linac4 H^- ion source plasma: Hydrogen atom production density profile and Hα intensity by collisional radiative model," *Review of Scientific Instruments*, vol. 85, no. 2, p. 02B118, 2014.

[23] M. Ohta, S. Mattei, M. Yasumoto, A. Hatayama, and J. Lettry, "Numerical study of the inductive plasma coupling to ramp up the plasma density for the Linac4 H^- ion source," *Review of Scientific Instruments*, vol. 85, no. 2, p. 02B113, 2014.

[24] S. Briefi, D. Fink, S. Mattei, J. Lettry, and U. Fantz, "Determination of discharge parameters via OES at the Linac4 H^- ion source," *Review of Scientific Instruments*, vol. 87, no. 2, 2016.

[25] S. Briefi, S. Mattei, J. Lettry, and U. Fantz, "Influence of the cusp field on the plasma parameters of the Linac4 H^- ion source," in *Proceedings of 5^{th} NIBS conference, Oxford, UK*, 2016.

[26] E. Mahner, C. Pasquino, C. Schmitzer, M. O'Neil, P. Chiggiato, J. Lettry, S. Mattei, and H. Neupert, "Gas injection and fast pressure-rise measurements for the Linac4 H^- source," in *AIP Conf. Proc.*, vol. 1515, pp. 425–432, 2013.

[27] C. De Melis, "The CERN accelerator complex. Complexe des accélérateurs du CERN," Jul 2016. General Photo.

[28] "The European Strategy for Particle Physics," *CERN-Council-S-0106*, May 2013.

[29] J. B. Lallement, A. Akroh, G. Bellodi, J. F. Comblin, V. A. Dimov, E. Granemann Souza, J. Lettry, A. M. Lombardi, O. Midttun, E. Ovalle, U. Raich, F. Roncarolo, C. Rossi, R. Sanchez Alvarez, C. A. Scrivens, C. A. Valerio-Lizarraga, M. Vretenar, and M. Yarmohammadi Satri, "First commissioning experience with the LINAC4 3 MeV front-end at CERN," *CERN CDS*, 2013.

[30] L. Arnaudon, P. Baudrenghien, M. Baylac, G. Bellodi, Y. Body, J. Borburgh, P. Bourquin, J. Broere, O. Brunner, L. Bruno, C. Carli, F. Caspers, S. M. Cousineau, Y. Cuvet, C. De Almeida Martins, T. Dobers, T. Fowler, R. Garoby, F. Gerigk, B. Goddard, K. Hanke, M. Hori, M. Jones, K. Kahle, W. Kalbreier, T. Kroyer, D. Küchler, A. M. Lombardi, L. A. López-Hernandez, M. Magistris, M. Martini, S. Maury, E. Page, M. Paoluzzi, M. Pasini, U. Raich, C. Rossi, J. P. Royer, E. Sargsyan, J. Serrano, R. Scrivens, M. Silari, M. Timmins,

W. Venturini-Delsolaro, M. Vretenar, R. Wegner, W. Weterings, and T. Zickler, "Linac4 Technical Design Report," Tech. Rep. CERN-AB-2006-084. CARE-Note-2006-022-HIPPI, CERN, Geneva, Dec 2006. revised version submitted on 2006-12-14 09:00:40.

[31] M. Bacal and G. W. Hamilton, "H^- and D^- production in plasmas," *Phys. Rev. Lett.*, vol. 42, pp. 1538–1540, Jun 1979.

[32] Y. Belchenko, G. Dimov, and V. Dudnikov, "A powerful injector of neutrals with a surface-plasma source of negative ions," *Nuclear Fusion*, vol. 14, no. 1, p. 113, 1974.

[33] M. Bacal, "Physics aspects of negative ion sources," *Nuclear Fusion*, vol. 46, no. 6, p. S250, 2006.

[34] R. K. Janev, D. Reiter, and U. Samm, "Collision processes in low-temperature hydrogen plasmas," Juel-Report 4105, 2003.

[35] J. Hiskes, "Cross sections for the vibrational excitation of the H_2 $X^1\Sigma_g^+(v)$ levels generated by electron collisional excitation of the higher singlet states," *Journal of applied physics*, vol. 70, no. 7, pp. 3409–3417, 1991.

[36] M. Seidl, H. L. Cui, J. D. Isenberg, H. J. Kwon, and B. S. Lee, "Surface production of negative hydrogen ions," *AIP Conference Proceedings*, vol. 287, no. 1, pp. 25–37, 1992.

[37] M. Seidl, H. L. Cui, J. D. Isenberg, H. J. Kwon, B. S. Lee, and S. T. Melnychuk, "Negative surface ionization of hydrogen atoms and molecules," *Journal of Applied Physics*, vol. 79, no. 6, pp. 2896–2901, 1996.

[38] M. Bacal and M. Wada, "Negative ion production by plasma-surface interaction in caesiated negative ion sources," *AIP Conference Proceedings*, vol. 1515, no. 1, pp. 41–48, 2013.

[39] J. P. Boeuf, B. Chaudhury, and L. Garrigues, "Physics of a magnetic filter for negative ion sources. i. collisional transport across the filter in an ideal, 1d filter," *Physics of Plasmas*, vol. 19, no. 11, p. 113509, 2012.

[40] S. Mochalskyy, J. Lettry, and T. Minea, "Beam formation in CERNs cesiated surfaces and volume H^- ion sources," *New Journal of Physics*, vol. 18, no. 8, p. 085011, 2016.

[41] D. A. Fink, J. Lettry, Ø. Midttun, R. Scrivens, D. Steyaert, and C. A. Valerio-Lizarraga, "Optimization of the beam extraction systems for the Linac4 H^- ion source," *AIP Conference Proceedings*, vol. 1655, no. 1, p. 030006, 2015.

[42] D. Aguglia, "Design of a system of high voltage pulsed power converters for CERN's Linac4 H^- ion source," in *2013 19th IEEE Pulsed Power Conference (PPC)*, pp. 1–6, June 2013.

[43] M. M. Paoluzzi, M. Haase, J. M. Balula, and D. Nisbet, "CERN Linac4 H^- source and SPL plasma generator RF systems, RF power coupling and impedance measurements," *AIP Conference Proceedings*, vol. 1390, no. 1, pp. 265–271, 2011.

[44] Ø. Midttun, T. Kalvas, M. Kronberger, J. Lettry, H. Pereira, and R. Scrivens, "A magnetized Einzel lens electron dump for the Linac4 H^- ion source," *AIP Conference Proceedings*, vol. 1515, no. 1, pp. 481–490, 2013.

[45] P. Chabert and N. Braithwaite, *Physics of radio-frequency plasmas*. Cambridge University Press, 2011.

[46] J. Hopwood, "Review of inductively coupled plasmas for plasma processing," *Plasma Sources Science and Technology*, vol. 1, no. 2, p. 109, 1992.

[47] M. Laroussi, "Low temperature plasma-based sterilization: Overview and state-of-the-art," *Plasma Processes and Polymers*, vol. 2, no. 5, pp. 391–400, 2005.

[48] K. Chandrakar, "The transition from the first to the second stage of the ring discharge," *Journal of Physics D: Applied Physics*, vol. 11, no. 13, p. 1809, 1978.

[49] A. Daltrini, S. Moshkalev, T. Morgan, R. Piejak, and W. Graham, "Plasma power measurement and hysteresis in the EH transition of a RF inductively coupled plasma system," *Applied Physics Letters*, vol. 92, no. 6, pp. 61504–61900, 2008.

[50] U. Kortshagen, N. Gibson, and J. Lawler, "On the E-H mode transition in RF inductive discharges," *Journal of Physics D: Applied Physics*, vol. 29, no. 5, p. 1224, 1996.

[51] H.-C. Lee and C.-W. Chung, "Effect of electron energy distribution on the hysteresis of plasma discharge: Theory, experiment, and modeling," *Scientific reports*, vol. 5, 2015.

[52] T. Wegner, C. Küllig, and J. Meichsner, "Electron heating during EH transition in inductively coupled rf plasmas," *Plasma Sources Science and Technology*, vol. 24, no. 4, p. 044001, 2015.

[53] T. Wegner, C. Küllig, and J. Meichsner, "Mode transition and hysteresis in inductively coupled radio frequency argon discharge," *Physics of Plasmas (1994-present)*, vol. 23, no. 2, p. 023503, 2016.

[54] E. Kawamura, M. A. Lieberman, A. J. Lichtenberg, and D. B. Graves, "Two-dimensional simulation of inductive–capacitive transition instability in an electronegative plasma," *Plasma Sources Science and Technology*, vol. 21, no. 4, p. 045014, 2012.

[55] M. Kronberger, E. Chaudet, G. Favre, J. Lettry, D. Küchler, P. Moyret, M. Paoluzzi, L. PreverâLoiri, C. Schmitzer, R. Scrivens, and D. Steyaert, "Magnetic Cusp Configuration of the SPL Plasma Generator," *AIP Conference Proceedings*, vol. 1390, no. 1, pp. 255–264, 2011.

[56] K. Yee, "Numerical solution of initial boundary value problems involving Maxwell's equations in isotropic media," *Antennas and Propagation, IEEE Transactions on*, vol. 14, no. 3, pp. 302–307, 1966.

[57] G. Mur, "Absorbing boundary conditions for the finite-difference approximation of the time-domain electromagnetic-field equations," *Electromagnetic Compatibility, IEEE Transactions on*, vol. EMC-23, no. 4, pp. 377–382, 1981.

[58] A. Bayliss and E. Turkel, "Radiation boundary conditions for wave-like equations," *Communications on Pure and applied Mathematics*, vol. 33, no. 6, pp. 707–725, 1980.

[59] C. K. Birdsall and A. B. Langdon, *Plasma physics via computer simulation*. CRC Press, 2004.

[60] J. Verboncoeur, "Symmetric spline weighting for charge and current density in particle simulation," *Journal of Computational Physics*, vol. 174, no. 1, pp. 421 – 427, 2001.

[61] K. Nanbu, "Probability theory of electron-molecule, ion-molecule, molecule-molecule, and coulomb collisions for particle modeling of materials processing plasmas and gases," *IEEE Transactions on plasma science*, vol. 28, no. 3, pp. 971–990, 2000.

[62] K. Chandrakar and A. V. Engel, "The starting mechanism of the first stage of the ring discharge," *Proceedings of the Royal Society of London A: Mathematical, Physical and Engineering Sciences*, vol. 284, no. 1398, pp. 442–454, 1965.

[63] S. Nishioka, I. Goto, K. Miyamoto, A. Hatayama, and A. Fukano, "Study of ion-ion plasma formation in negative ion sources by a three-dimensional in real space and three-dimensional in velocity space particle in cell model," *Journal of Applied Physics*, vol. 119, no. 2, p. 023302, 2016.

[64] U. Fantz, B. Heinemann, D. Wünderlich, R. Riedl, W. Kraus, R. Nocentini, and F. Bonomo, "Towards 20 A negative hydrogen ion beams for up to 1 h: Achievements of the ELISE test facility (invited)," *Review of Scientific Instruments*, vol. 87, no. 2, 2016.

[65] H. Singh and D. B. Graves, "Measurements of the electron energy distribution function in molecular gases in an inductively coupled plasma," *Journal of Applied Physics*, vol. 87, no. 9, pp. 4098–4106, 2000.

[66] V. I. Kolobov, D. P. Lymberopoulos, and D. J. Economou, "Electron kinetics and non-joule heating in near-collisionless inductively coupled plasmas," *Phys. Rev. E*, vol. 55, pp. 3408–3422, 1997.

[67] U. Kortshagen, I. Pukropski, and L. D. Tsendin, "Experimental investigation and fast two-dimensional self-consistent kinetic modeling of a low-pressure inductively coupled rf discharge," *Phys. Rev. E*, vol. 51, pp. 6063–6078, 1995.

[68] H.-C. Lee, M.-H. Lee, and C.-W. Chung, "Experimental observation of the transition from nonlocal to local electron kinetics in inductively coupled plasmas," *Applied Physics Letters*, vol. 96, no. 4, 2010.

[69] R. A. Stewart, P. Vitello, and D. B. Graves, "Two-dimensional fluid model of high density inductively coupled plasma sources," *Journal of Vacuum Science and Technology B*, vol. 12, no. 1, pp. 478–485, 1994.

[70] J. D. Bukowski, D. B. Graves, and P. Vitello, "Two-dimensional fluid model of an inductively coupled plasma with comparison to experimental spatial profiles," *Journal of Applied Physics*, vol. 80, no. 5, pp. 2614–2623, 1996.

[71] H. C. Kim, F. Iza, S. S. Yang, M. Radmilović-Radjenović, and J. K. Lee, "Particle and fluid simulations of low-temperature plasma discharges: benchmarks and kinetic effects," *Journal of Physics D: Applied Physics*, vol. 38, no. 19, p. R283, 2005.

[72] P. L. G. Ventzek, T. J. Sommerer, R. J. Hoekstra, and M. J. Kushner, "Two-dimensional hybrid model of inductively coupled plasma sources for etching," *Applied Physics Letters*, vol. 63, no. 5, pp. 605–607, 1993.

[73] A. Langdon, "Effects of the spatial grid in simulation plasmas," *Journal of Computational Physics*, vol. 6, no. 2, pp. 247 – 267, 1970.

[74] R. J. Mason, "Implicit moment particle simulation of plasmas," *Journal of Computational Physics*, vol. 41, no. 2, pp. 233 – 244, 1981.

[75] J. Denavit, "Time-filtering particle simulations with $\omega_{\mathrm{pe}}\Delta t \gg 1$," *Journal of Computational Physics*, vol. 42, no. 2, pp. 337 – 366, 1981.

[76] A. Friedman, A. Langdon, and B. Cohen, "A direct method for implicit particle-in-cell simulation," *Comments on plasma physics and controlled fusion*, vol. 6, no. 6, pp. 225–236, 1981.

[77] G. Chen, L. Chacón, and D. Barnes, "An energy- and charge-conserving, implicit, electrostatic particle-in-cell algorithm," *Journal of Computational Physics*, vol. 230, no. 18, pp. 7018 – 7036, 2011.

[78] S. Markidis and G. Lapenta, "The energy conserving particle-in-cell method," *Journal of Computational Physics*, vol. 230, no. 18, pp. 7037 – 7052, 2011.

[79] J. Brackbill and D. Forslund, "An implicit method for electromagnetic plasma simulation in two dimensions," *Journal of Computational Physics*, vol. 46, no. 2, pp. 271 – 308, 1982.

[80] W. T. Taitano, "Development of a jacobian-free-newton-krylov method with kinetic enslavement to implicitly solve vlasov-poisson system in plasma physics," Master's thesis, University of Idaho, 2010.

[81] M. Pernice and H. F. Walker, "Nitsol: A newton iterative solver for nonlinear systems," *SIAM Journal on Scientific Computing*, vol. 19, no. 1, pp. 302–318, 1998.

[82] J. Brackbill and B. Cohen, "Simulation of low-frequency, electromagnetic phenomena in plasma," in *Multiple time scales*, pp. 271–310, Academic Press, Inc., 1985.

[83] J. P. Boris, "Relativistic plasma simulation-optimization of a hybrid code," *Proceeding of Fourth Conference on Numerical Simulations of Plasmas*, November 1970.

[84] J. M. Wallace, J. U. Brackbill, and D. W. Forslund, "An implicit moment electromagnetic plasma simulation in cylindrical coordinates," *Journal of Computational Physics*, vol. 63, no. 2, pp. 434–457, 1986.

[85] T. Takizuka and H. Abe, "A binary collision model for plasma simulation with a particle code," *Journal of Computational Physics*, vol. 25, no. 3, pp. 205 – 219, 1977.

[86] R. K. Janev, W. D. Langer, K. Evans Jr, and E. Douglass Jr, *Elementary processes in hydrogen-helium plasmas: cross sections and reaction rate coefficients*, vol. 4. Springer-Verlag Berlin Heidelberg, 1987.

[87] S. Buckman and Y. Itikawa, *Interactions of Photons and Electrons with Atoms*. Springer, 2000.

[88] S. Buckman *et al.*, *Interactions of Photons and Electrons with Molecules*. Springer-Verlag, 2003.

[89] P. T. Greenland, D. Reiter, and F. Jülich, *The role of molecular hydrogen in plasma recombination*. Forschungszentrum Jülich, 1996.

[90] P. Krstic and D. Schultz, "Elastic and related transport cross sections for collisions among isotopomers of $H^+ + H$, $H^+ + H_2$, $H^+ + He$, $H + H$ and $H + H_2$," *Plasma-Mater. Data Fusion*, vol. 8, no. 1, 1998.

[91] A. V. Phelps, "Cross sections and swarm coefficients for H^+, H_2^+, H_3^+, H, H_2, and H^- in H_2 for energies from 0.1 eV to 10 keV," *Journal of Physical and Chemical Reference Data*, vol. 19, no. 3, pp. 653–675, 1990.

[92] A. Aanesland, L. Liard, G. Leray, J. Jolly, and P. Chabert, "Direct measurements of neutral density depletion by two-photon absorption laser-induced fluorescence spectroscopy," *Applied Physics Letters*, vol. 91, no. 12, 2007.

[93] G. Lapenta, "Particle rezoning for multidimensional kinetic particle-in-cell simulations," *J. Comput. Phys.*, vol. 181, pp. 317–337, Sept. 2002.

[94] Y. Saad, "Sparsekit: a basic tool kit for sparse matrix computations," tech. rep., University of Minnesota, Computer Science Department, June 1994.

[95] M. A. Lieberman and A. J. Lichtenberg, *Principles of plasma discharges and materials processing*. John Wiley & Sons, 2005.

[96] Y. P. Raizer and J. E. Allen, *Gas discharge physics*, vol. 2. Springer Berlin, 1997.

[97] T. Shibata, M. Kashiwagi, A. Hatayama, K. Sawada, T. Inoue, and M. Hanada, "Numerical study of the h0 atomic density and the balmer line intensity profiles in a hydrogen negative ion source with the effect of non-equilibrium electron energy distribution function," *Plasma and Fusion Research*, vol. 9, 2014.

[98] S. Abe, S. Nishioka, S. Mattei, A. Hatayama, and J. Lettry, "Effect of the puller-electrode voltage on the extraction in Linac4 negative ion source," in *Proceedings of 5^{th} NIBS conference, Oxford, UK*, 2016.

[99] L. Arnaudon *et al.*, "Linac4 technical design report." CERN-AB-2006-084 ABP/RF, 2006.

[100] M. Bacal and M. Wada, "Negative hydrogen ion production mechanisms," *Appl. Phys. Rev.*, vol. 2, p. 021305, 2015.

[101] D. Wünderlich, S. Dietrich, and U. Fantz, "Application of a collisional radiative model to atomic hydrogen for diagnostic purposes," *J. Quant. Spectr. Rad. Transfer*, vol. 110, no. 1–2, pp. 62 – 71, 2009.

[102] D. Wünderlich, "Berechnung von Teilchendichten für die Diagnostik an Niedertemperaturplasmen," *Ph.D. thesis, University of Augsburg*, 2004.

[103] D. Wünderlich and the NNBI Team, "Influence of photoelectron emission on the plasma sheath in cesiated sources for negative hydrogen ions," *Proceedings of the 30th ICPIG, Belfast, Northern-Ireland*, 2011.

[104] J. Lettry *et al.*, "H^- Ion Sources for CERN's Linac4," *AIP Conf. Proc.*, vol. 1515, pp. 302–311, 2013.

[105] E. Mahner *et al.*, "Gas injection and fast pressure-rise measurements for the Linac4 H^- sources," *AIP Conf. Proc.*, vol. 1515, pp. 425–432, 2013.

[106] P. Vankan, D. Schram, and R. Engeln, "High rotational excitation of molecular hydrogen in plasmas," *Chem. Phys. Lett.*, vol. 400, pp. 196 – 200, 2004.

[107] S. Briefi, D. Rauner, and U. Fantz, "Determination of the rotational population of H_2 and D_2 including high-N states in low temperature plasmas via the Fulcher-α transition," *Journal of Quantitative Spectroscopy and Radiative Transfer*, vol. 187, pp. 135 – 144, 2017.

[108] S. A. Astashkevich *et al.*, "Radiative characteristics of 3p σ, π, 3d π^-, δ^- states of H_2 and determination of gas temperature of low pressure hydrogen containing plasmas," *J. Quant. Spectrosc. Radiat. Transfer*, vol. 56, pp. 725 – 751, 1996.

[109] S. Briefi *et al.*, "Determination of discharge parameters via OES at the Linac4 H^- ion source," *Rev. Sci. Instrum.*, vol. 87, p. 02B104, 2016.

[110] S. Mattei *et al.*, "RF plasma modeling of the Linac4 H^- ion source," *AIP Conf. Proc.*, vol. 1515, pp. 386–393, 2013.

[111] T. Shibata, S. Mattei, K. Nishida, J. Lettry, and A. Hatayama, "Numerical and experimental study of atomic transport and Balmer line intensity in Linac4 negative ion source," *AIP Conf. Proc.*, vol. 1655, no. 1, p. 020008, 2015.

Stefano Mattei

Tel. +41 22 76 71 911
Email: stefano.mattei@cern.ch

EDUCATION

Ph.D.

Ph.D. in Physics, Swiss Plasma Center
École Polytechnique Fédérale de Lausanne (September 2014 - present)
In collaboration with CERN, Geneva, Switzerland

Thesis title: H^- ion source for the CERN Linac4 accelerator: simulation, experimental validation and optimization of the hydrogen plasma

My work consists in the development of a parallel fully-implicit Particle-In-Cell Monte Carlo Collision (PIC-MCC) code for the simulation of inductively coupled plasmas, its validation and application to proper engineering of the Linac4 H^- ion source (in collaboration with KEIO University in Japan). Furthermore, I perform optical emission spectroscopy/photometry measurements to characterize the hydrogen plasma.

Master of Science:

Master of Science in Aerospace Engineering with distinction (cum laude)
TU Delft, The Netherlands (Sept. 2007 - Aug. 2010)

During my master's studies I focused on the theoretical and computational aspects of aerodynamics, acquiring a solid base in mathematical methods and programming.

Thesis title: A semi-continuous approach to reduced-order modeling

Bachelor of Science:

B.Sc. in Aerospace Engineering
Milan Polytechnic, Italy (Sept. 2003 - March 2007)

WORK EXPERIENCE

CERN fellowship
CERN, Geneva, Switzerland (Sept. 2011 - August 2014)

Linac4 H^- ion source development and operation:

- Plasma and electromagnetic simulations
- Experimental work: measurement of plasma parameters via optical emission spectroscopy, photometry and Langmuir probe. Fast pressure rise measurements.
- Participation in design meetings and source operation.

Assistant Patent Examiner
European Patent Office (EPO), Munich, Germany (2011)
EPO, Rijswijk, The Netherlands (2007 - 2010)

My work involved examining patent applications for three contract projects in the field:

- Hydraulic circuits for servomotors (Feb. 2011 - June 2011 and Nov. 2009 - June 2010)
- Arrangements of data in optical and magneto-optical discs (Sept. 2008 - Dec. 2008)
- Recording-reproducing devices (July 2007 - March 2008)

Research Assistant, Plasma Physics Department
Université de Montréal, Canada (Jan. 2009 - July 2009, during my M.Sc. program)

My work involved the characterization of expanding chlorine and argon plasmas sustained by electromagnetic surface waves via optical emission spectroscopy.

Graduate Student Assistant
TU Delft, The Netherlands (2008 - 2010)

Graduate assistant for two bachelor's level courses and a master's level course

- Programming I (B.Sc.) - lab sessions and grading assignments (Nov. 2009 - Jan. 2010)
- Computational fluid and solid mechanics (B.Sc.) - Assisting lab sessions, grading lab and take-home assignments (Sept. 2009 - Nov. 2009)
- Computational fluid dynamics (M.Sc) - Helping course supervisor prepare lectures, assisting students with questions about course content and with their final project (Sept. 2008 - Dec. 2008)

TRAINING

CERN Accelerator School - Basics of Accelerator Science and Technology at CERN
Chavannes de Bogis, Switzerland, 4-8 November 2013

CERN Accelerator School - Ion Sources
Senec, Slovakia, 29 May - 8 June 2012

Technical courses on radiological protection and electrical habilitation

ADDITIONAL SKILLS

Languages:

Italian:	Mother tongue
English:	Fluent - Main working language. TOEFL: 110/120
French:	Fluent - Second working language
Spanish:	Fluent
German:	Intermediate
Japanese:	Basic conversational knowledge

Technical skills: High performance computing: advanced user in Matlab and Fortran, parallel computing via Message Passing Interface (MPI) and OpenMP, familiar with C++ and Python.
Software: Opera VectorField, LaTex, Office and Origin

Outreach: Visit service at CERN - I guided tours in English, French, Italian and Spanish.
For the past 3 years I lectured "Introduction to particle accelerator" for the Spanish teacher's program at CERN and I gave 3 seminars in Italian schools about CERN.

Awards:

- Graduated (M.Sc.) in Aerospace Engineering with distinction, cum laude (top 5% students)
- Awarded an IB-Groep Scholarship for international students working and studying at the same time in the country of the sponsoring group, the Netherlands
- Awarded an ISU scholarship for merit and financial need, Italy (undergraduate studies)
- Awarded housing during undergraduate studies in Milan, Fondazione Mattei apartments in Milan, based on merit and financial need

Appendix – Publications and Conference Presentations

1. S. Briefi, S. Mattei, D. Rauner, J. Lettry, M. Q. Tran, and U. Fantz, "Experimental benchmark of the NINJA code for application to the Linac4 H^- ion source plasma", submitted to *New Journal of Physics, 2017*

2. S. Mattei, K. Nishida, M. Onai, J. Lettry, M. Q. Tran, and A. Hatayama, "A fully-implicit Particle-In-Cell Monte Carlo Collision code for the simulation of inductively coupled plasmas", submitted to *Journal of Computational Physics, 2017*

3. S. Mattei, K. Nishida, S. Mochizuki, A. Grudiev, J. Lettry, M. Q. Tran, and A. Hatayama, "Kinetic simulations and photometry measurements of the E-H transition in cylindrical inductively coupled plasmas", *Plasma Sources Science and Technology 25(6), 065001, 2016.* http://stacks.iop.org/0963-0252/25/i=6/a=065001

4. S. Mattei, K. Nishida, M. Onai, J. Lettry, M. Q. Tran, and A. Hatayama, "Numerical simulation of the RF plasma discharge in the Linac4 H^- ion source," *AIP Conference Proceedings, 5th NIBS conference, Oxford, UK, 2016, in press.*

5. S. Briefi, S. Mattei, J. Lettry, and U. Fantz, "Influence of the cusp field on the plasma parameters of the Linac4 H^- ion source," *AIP Conference Proceedings, 5th NIBS conference, Oxford, UK, 2016, in press.*

6. K. Nishida, S. Mattei, S. Mochizuki, J. Lettry, A. Hatayama, "Kinetic modeling of E-to-H mode transition in inductively coupled hydrogen plasmas", *J. Appl. Phys. 119, 233302, 2016.* http://dx.doi.org/10.1063/1.4953647

7. J. Lettry, et al., "Linac4 H^- ion sources," *Review of Scientific Instruments, vol. 87, no. 02B139, 2016.* http://dx.doi.org/10.1063/1.4936120

8. M. Onai, H. Etoh, Y. Aoki, T. Shibata, S. Mattei, S. Fujita, A. Hatayama, and J. Lettry, "Effect of high energy electrons on H^- production and destruction in a high current dc negative ion source for cyclotron," *Review of Scientific Instruments, vol. 87, no. 2, 2016.* http://dx.doi.org/10.1063/1.4934846

9. S. Mochizuki, S. Mattei, K. Nishida, A. Hatayama, and J. Lettry, "Analysis of electron energy distribution function in the Linac4 H^- source," *Review of Scientific Instruments, vol. 87, no. 2, 2016.* http://dx.doi.org/10.1063/1.4932322

10. L. Cheng, S. Mattei, P. W. Fick, S. Hulshoff, "A Semi-Continuous Formulation for Goal-oriented Reduced-Order Models: 1D problems", *International Journal for Numerical Methods in Engineering 105(6), 2015.* http://dx.doi.org/10.1002/nme.4990

11. T. Shibata, K. Nishida, S. Mochizuki, S. Mattei, J. Lettry, A. Hatayama, A. Ueno, H. Oguri, K. Ohkoshi, K. Ikegami, A. Takagi, H. Asano, and F. Naito, "Numerical study of plasma generation process and internal antenna heat loadings in J-PARC RF negative ion source," *Review of Scientific Instruments, vol. 87, no. 2, 2016.* http://dx.doi.org/10.1063/1.4931787

12. I. Goto, K. Miyamoto, S. Nishioka, S. Mattei, J. Lettry, S. Abe, and A. Hatayama, "Effect of coulomb collision on the negative ion extraction mechanism in negative ion sources," *Review of Scientific Instruments, vol. 87, no. 2, 2016.* http://dx.doi.org/10.1063/1.4934206

13. S. Briefi, D. Fink, S. Mattei, J. Lettry, and U. Fantz, "Determination of discharge parameters via OES at the Linac4 H^- ion source," *Review of Scientific Instruments, vol. 87, no. 2, 2016.* http://dx.doi.org/10.1063/1.4932009

14. J. Lettry et al., "CERN's Linac4 H^- sources: status and operational results," in *AIP Publishing, NIBS 2014, vol. 1655, p. 030005, 2015.* http://dx.doi.org/10.1063/1.4916432

15. T.Shibata, S. Mattei, K. Nishida, J. Lettry, and A. Hatayama, "Numerical and experimental study of atomic transport and Balmer line intensity in Linac4 negative ion source*," in AIP Publishing, NIBS 2014, vol. 1655, p. 020008, 2015.* http://dx.doi.org/10.1063/1.4916417

16. S. Mochizuki, S. Mattei, T. Shibata, K. Nishida, A. Hatayama, and J. Lettry, "Initial results of a full kinetic simulation of RF H^- source including Coulomb collision process," *in AIP Publishing, NIBS 2014, vol. 1655, p. 020016, 2015.* http://dx.doi.org/10.1063/1.4916425

17. K. Nishida, S. Mochizuki, M. Ohta, M. Yasumoto, J. Lettry, S. Mattei, and A. Hatayama, "Equivalent circuit of radio frequency-plasma with the transformer model," *Review of Scientific Instruments, vol. 85, no. 2, p. 02B117, 2014.* http://dx.doi.org/10.1063/1.4832060

18. S. Mattei, M. Ohta, M. Yasumoto, A. Hatayama, J. Lettry, and A. Grudiev, "Plasma ignition and steady state simulations of the Linac4 H^- ion source," *Review of Scientific Instruments, vol. 85, no. 2, p. 02B115, 2014.* http://dx.doi.org/10.1063/1.4833919

19. S. Mattei, S. Mochizuki, K. Nishida, T. Shibata, J. Lettry, A. Hatayama, and M. Q. Tran, "RF plasma conductivity in the CERN Linac4 H^- ion source, comparison of simulations and measurements," in APS Meeting Abstracts, 2014.

20. J. Lettry et al., "Status and operation of the Linac4 ion source prototypes", *Review of Scientific Instruments, vol. 85, no. 2, p. 02B122, 2014*. http://dx.doi.org/10.1063/1.4848975

21. A. Grudiev, J. Lettry, S. Mattei, M. Paoluzzi, and R. Scrivens, "Numerical simulation of electromagnetic fields and impedance of CERN Linac4 H^- source taking into account the effect of the plasma," *Review of Scientific Instruments, vol. 85, no. 2, p. 02B134, 2014.* http://dx.doi.org/10.1063/1.4842317

22. T. Yamamoto, T. Shibata, M. Ohta, M. Yasumoto, K. Nishida, A. Hatayama, S. Mattei, J. Lettry, K. Sawada, and U. Fantz, "Modeling of neutrals in the Linac4 H− ion source plasma: Hydrogen atom production density profile and Hα intensity by collisional radiative model," *Review of Scientific Instruments, vol. 85, no. 2, p. 02B118, 2014.*

23. M. Ohta, S. Mattei, M. Yasumoto, A. Hatayama, and J. Lettry, "Numerical study of the inductive plasma coupling to ramp up the plasma density for the Linac4 H^- ion source," *Review of Scientific Instruments, vol. 85, no. 2, p. 02B113, 2014.* http://dx.doi.org/10.1063/1.4833920

24. S. Mattei, Y. Kawamura, C. Schmitzer, J. Lettry, A. Hatayama, M. Ohta, and M. Yasumoto, "RF plasma modeling of the Linac4 H^- ion source," *in AIP Conf. Proc., vol. 1515 of CERN-ATS-2013-014, pp. 386–393, 2013.*

25. J. Lettry et al., "H^- ion sources for CERN's Linac4," *AIP Conference Proceedings*, 1515, 302-311 (2013), DOI: http://dx.doi.org/10.1063/1.4792798

26. E. Mahner, C. Pasquino, C. Schmitzer, M. O'Neil, P. Chiggiato, J. Lettry, S. Mattei, and H. Neupert, "Gas injection and fast pressure-rise measurements for the Linac4 H^- source," *in AIP Conf. Proc., vol. 1515, pp. 425–432, 2013.*

27. O. Boudreault, S. Mattei, L. Stafford, J. Margot, M. Moisan, R. Khare, and V. M. Donnelly, "Nonlocal effect of plasma resonances on the electron energy-distribution function in microwave plasma columns," *Physical Review E* 86(1), 015402, 2012. http://link.aps.org/doi/10.1103/PhysRevE.86.015402

28. S. Mattei, O. Boudreault, R. Khare, L. Stafford, and V.M. Donnelly, "Characterization of a low-pressure chlorine plasma column sustained by propagating surface waves using phase-sensitive microwave interferometry and trace-rare-gas optical emission spectroscopy," *Journal of Applied Physics* 109, 113304, 2011. http://jap.aip.org/resource/1/japiau/v109/i11/p113304_s1

29. L. Stafford, J. Guha, R. Khare, S. Mattei, O. Boudreault, B. Clain, and V.M. Donnelly, "Experimental and modeling study of O- and Cl-atoms surface recombination reactions in oxygen and chlorine plasmas," *Pure and Applied Chemistry* 82(6), 1301-1315, 2010. http://www.iupac.org/publications/pac/82/6/1301/